DISS. ETH NO. 28633

Shear rate imaging using a polarization camera and birefringent aqueous cellulose nanocrystal suspensions

A thesis submitted to attain the degree of
DOCTOR OF SCIENCES of ETH ZURICH
(Dr. sc. ETH Zurich)

presented by
CONNOR PIERS LANE

MSc ETH Masch.-Ing, ETH Zurich
born on January 20, 1992
citizen of Germany and the United Kingdom

accepted on the recommendation of
Prof. Dr. Thomas Rösgen, examiner
Prof. Dr. Jürg Dual, co-examiner

2022

Copyright © 2022 Connor Piers Lane

Institute of Fluid Dynamics, ETH Zürich

All rights reserved

Shear rate imaging using a polarization camera and birefringent aqueous cellulose nanocrystal suspensions

Published and distributed by:

Institute of Fluid Dynamics
ETH Zürich
8092 Zürich
Switzerland

https://ifd.ethz.ch/

Abstract

A fluid that is composed of anisotropic particles may show birefringence when under the effect of shear. This phenomenon is known as shear induced birefringence and it is of interest to researchers for two reasons. First, to study the rheological behaviour as birefringence is linked to particle alignment. Second, to study and visualize fluid flows. The most common way to measure birefringence is to send polarized light through the birefringent material and to measure the change in polarization.

This thesis considers five aspects of flow birefringence measurements which were also the subject of five corresponding publications.

First, we give guidance for researchers calibrating a polarization-sensitive camera. For this, we define an error that quantifies the quality of the polarization measurements and discuss multiple factors influencing the measurement quality. We show that sufficiently large f-numbers no longer influence measurement quality and argue that lens design and focal length have little influence.

Second, we describe a two-dimensional birefringence measurement technique that is based on a rotatable linear polarizer and a polarization camera. By measuring the first three Stokes parameters, the technique determines the relative position of the refractive index axes and the relative phase difference. The measurement range of the optical retardation is half the wavelength of the illumination.

Third, we present an experimental procedure to measure the optical response of a birefringent fluid to shear. The experimental set-up is based on a Taylor-Couette flow where transparent end plates at the top and bottom enable optical access. Using a polarization camera, the absolute difference between the two main

refractive indices and the relative position of the refractive index axes with respect to the flow direction (commonly referred to as extinction angle) are determined.

Fourth, we report birefringence measurements in aqueous cellulose nanocrystal suspensions. Suspensions with concentrations between 0.7 and 1.3% per weight are sheared with shear rates up to 31 1/s and show extinction angles of 23-40° and birefringence in the order of 1e-5.

Fifth, the birefringence response of aqueous cellulose nanocrystal suspensions is used to measure shear and strain rates in a two-dimensional fluid flow. The results show that the study of shear rates in a two-dimensional shearing flow by means of flow birefringence is feasible and therefore encourage the use of aqueous CNC suspensions for birefringent flow studies. However, the results indicate that the angle between principal strain rate and direction of flow affects particle alignment and thus birefringence.

Kurzfassung

Ein Fluid, das aus anisotropen Partikeln zusammengesetzt ist, kann unter dem Einfluss von Scherung doppelbrechend werden. Dieses Phänomen ist auch bekannt unter dem Namen Strömungsdoppelbrechung und für Forscher aus zwei Gründen von Interesse. Zum einen für die Untersuchung von rheologischen Eigenschaften, da Strömungsdoppelbrechung im Zusammenhang mit der Ausrichtung der Partikel steht. Zum anderen für Visualisierungen und Studien von Strömungen. Die gängigste Art Doppelbrechung zu messen ist polarisiertes Licht durch das doppelbrechende Material zu schicken und die Änderung der Polarisation zu bestimmen.

Diese Arbeit beschäftigt sich mit fünf Aspekten der Messung von Strömungsdoppelbrechung, die auch den Inhalt von fünf entsprechenden wissenschaftlichen Veröffentlichungen darstellen.

Zunächst berichten wir von unseren Erfahrungen mit der Kalibration einer polarisationsempfindlichen Kamera. Wir definieren eine Fehlergrösse, die die Messqualität der Polarisationsmessungen quantifiziert und untersuchen mithilfe der Fehlergrösse verschiedene Einflussfaktoren auf die Messqualität. Wir zeigen, dass bei hinreichend grosser F-Zahl diese keinen Einfluss auf die Messqualität hat und argumentieren, dass der Einfluss des Objektivs sowie der Brennweite zu vernachlässigen ist.

Als Zweites beschreiben wir eine Messmethodik, um zweidimensional verteilte Doppelbrechung zu messen. Die Technik basiert auf einen rotierbaren linearen Polarisationsfilter und einer Polarisationskamera. Mit der Kamera werden die ersten drei Stokes Parameter gemessen, mit denen die relative Position der beiden Hauptbrechungsindex Achsen sowie die relative Phasenverschiebung bestimmt

werden. Das Verfahren kann optische Verzögerungen von einer halben Wellenlänge der Beleuchtung messen.

Im dritten Teil beschreiben wir ein experimentelles Verfahren, mit dem die Strömungsdoppelbrechung einer Flüssigkeit in einer Scherströmung bestimmt werden kann. Das Experiment basiert auf einer Taylor-Couette Strömung. Transparente Endflächen im Boden und an der Decke ermöglichen einen optischen Zugang. Mittels einer Polarisationskamera kann die absolute Differenz der beiden Hauptbrechungsindexe sowie die relative Position derer Achsen (auch bekannt als Auslöschwinkel) bestimmt werden.

Im vierten Teil charakterisieren wir die Strömungsdoppelbrechung in wässrigen Suspensionen bestehend aus Cellulose Nanokristallen mit Gewichtsprozentsätzen von 0.7 bis 1.3%. Scherraten von bis zu 31 1/s ergaben Auslöschwinkel im Bereich von 23-40° und Doppelbrechungen in der Grössenordnung von 1e-5.

Im fünften Teil werden anhand der gemessenen Strömungsdoppelbrechung die Scher- und Dehnraten einer zweidimensionalen Strömung ermittelt. Die Ergebnisse zeigen, dass das Messen von Scherraten in einer zweidimensionalen Scherströmung mittels Strömungsdoppelbrechung zu plausiblen Ergebnissen führt. Jedoch deuten die Ergebnisse auch darauf hin, dass der Winkel zwischen Dehnungshauptachse und Strömungsrichtung die Partikelausrichtung und somit die Strömungsdoppelbrechung beeinflusst.

Acknowledgements

I would like to express my upmost gratitude to Professor Thomas Rösgen from the Institute of Fluid Dynamics for supervising my research and his superb guidance. His continued support and assistance have, in the first place, made this thesis possible. I thoroughly enjoyed the time spent working with him and all the numerous constructive discussions.

I sincerely wish to express my full gratitude to Professor Jürg Dual from the Institute of Mechanical Systems for his co-supervision.

I would also like to thank the faculty of the Department of Mechanical and Process Engineering for the solid and sound theoretical fundamentals I have gained in my Bachelor's and Master's degree programmes.

Special thanks go to Rene Holliger for his technical assistance, ideas and suggestions, as well as to Bianca Maspero and Maria Halbleib for their administrative help. I also wish to thank Maximilian Müller, Pascal Aeschi, Lena Egli, Sebastian Lerch, Adrian Köpfli, Nathalie Nick, Frédéric Baumann, and David Rode who contributed to this work by completing various student projects with me. Further thanks to David Rode for his great support in the lab as well as for his contribution towards the publications.

I would also like to mention my appreciate to my colleagues Hanna Berning, Philipp Bühlmann, Julian Humml, Markus Schmidt, Jiggar Shah, Alexander Rusch, Christina Tsalicoglou, Bernhard Vennemann, and He Wang who made this experience enormously enjoyable.

Finally, I would like to thank my friends, family, and partner Anna-Carolin Bender for their great support, advice, and encouragement.

Contents

1. Introduction 7

1.1. Motivation 7

1.2. Thesis structure 8

2. Theory 11

2.1. Birefringence explained on a linear retarder 11

2.2. Stokes parameters and Mueller matrices 13

2.3. Strain and shear rates in a two-dimensional fluid flow 20

2.4. Birefringent fluids 26

2.4.1. Characteristic properties 26

2.4.2. Applications 27

2.5. Streaming birefringence in fluids vs. photoelasticity in solids 28

2.6. Three-dimensional flow birefringence 30

2.6.1. Refractive index tensor 30

2.6.2. Measurement techniques 31

2.6.3. Challenges 32

3. Calibration of a polarization image sensor and investigation of influencing factors 33

Abstract 34

3.1. Introduction 34
3.2. Material and methods 38
3.2.1. Optical setup 38
3.2.2. Calibration Procedure 40
3.2.3. Image Analysis 45
3.3. Results and Discussion 47
3.3.1. Effect of Dark Noise 47
3.3.2. Consistency of the 1224 x 1024 super-pixels 48
3.3.3. Influence of Focal Ratio and Choice of Lens 50
3.3.4. LCD Monitor Test Case 55
3.4. Conclusion 56
3.5. Appendix 57

4. Two-dimensional birefringence measurement technique using a polarization camera 61
Abstract 62
4.1. Introduction 62
4.2. Theory 64
4.3. Material and methods 73
4.3.1. Applied materials 73
4.3.2. Measurement procedure 73

4.3.3. Camera calibration 76

4.3.4. Performance tests 77

4.4. Results and discussion 78

4.4.1. Two-dimensional measurements 79

4.4.2. Number of required polarizer positions 81

4.4.3. Error analysis 83

4.4.4. Exemplary test case 84

4.5. Conclusion 87

5. Optical characterization method for birefringent fluids using a polarization camera 89

Abstract 90

5.1. Introduction 90

5.2. Materials and Methods 101

5.2.1. Theory 102

5.2.2. Material 109

5.2.3. Experimental Procedure 109

5.2.4. Data Fitting 114

5.3. Results and Discussion 120

5.3.1. Measurement of extinction angle 121

5.3.2. Measurement of birefringence 122

5.4. Conclusions 124

6. Birefringent properties of aqueous Cellulose Nanocrystal suspensions ... 125

Abstract 126

6.1. Introduction 126

6.2. Materials and methods 131

6.2.1. Material 131

6.2.2. Experimental setup 132

6.2.3. Optical characterization 134

6.2.4. Experimental procedure 139

6.3. Results and discussion 140

6.4. Appendix 145

7. Shear rate imaging using a polarization camera and a birefringent aqueous cellulose nanocrystal suspension 149

Abstract 150

7.1. Introduction 151

7.2. Material and methods 152

7.2.1. Experimental set-up 152

7.2.2. Two-dimensional birefringence measurements 154

7.2.3. Aqueous cellulose nanocrystal suspensions 155

7.2.4. Fluid flow simulation with Ansys Fluent 156
7.2.5. Measurement assumption 156
7.3. Results and discussion 157
7.3.1. Straight channel section 157
7.3.2. Cosine shaped constriction 158
7.4. Conclusion 160

8. Overall conclusion and outlook 163
8.1. Discussion 163
8.1.1. Summary 163
8.1.2. Personal conclusion 165
8.2. Potential future studies 166
8.2.1. The effect of the two-dimensional flow state on birefringence 166
8.2.2. Flow birefringence in axisymmetric flows 167
8.2.3. Three-dimensional flow birefringence studies 168
8.2.4. Polarization sensitive optical coherence tomography 169
8.3. Concluding remarks 169

Bibliography 171
Curriculum vitae 198

1. Introduction

1.1. Motivation

When the propagation of light through a material depends on the oscillation direction of the light, the material is optically anisotropic; or stated otherwise, the material is birefringent. For solid materials, birefringence can be classified into two types, intrinsic birefringence and stress induced birefringence (AZoOptics, 2014). Intrinsic birefringence is caused by an anisotropic structure within the material. Crystals such as calcite are well known examples. Stress-induced birefringence is caused by mechanical deformation, and this phenomenon is known as photoelasticity. Glass and plastics are typical materials which show this effect. When assessing these effects, the linear relation between phase difference and difference of the two corresponding principal stresses is described by the stress-optic law (Ramesh, 2000, p. 9). Prior to the introduction of numerical methods, photoelasticity had been routinely used for stress analysis.

Although the distinction between intrinsic and stress-induced birefringence is mainly associated with solids, it similarly applies to fluids. Liquid crystals have ordered structures that are (intrinsically) birefringent (Cowling, 2014; Te Nijenhuis et al., 2007). Because of their ordered structure liquid crystals are sometimes seen as a fourth state of matter, positioned between liquid and solid, and possessing fluid-like and solid-like properties (Kent State University, 2022). Fluids that show shear (stress) induced birefringence are composed of anisotropic particles or macromolecules (Merzkirch, 2001). At rest, these particles or macromolecules are randomly oriented due to Brownian motion. When under the effect of shear, the particles or macromolecules align in a preferential direction. Due to this anisotropic alignment the fluid becomes birefringent.

The experimental determination of shear rates and shear stresses in fluid flows is a challenge and currently there seems to be no generally preferred approach. If velocity measurements (McKeon et al., 2007) are available, the shear rates, being velocity derivatives, can be approximated. However, the differentiation of experimental data is not always straightforward (Ahnert & Abel, 2007), especially when the data is rather noisy. As photoelasticity has proven to be a successful method to visualize and study stresses in solids, it is only consequent that researchers have tried and are still trying to utilize this measurement technique for the study of fluid flows. To date, however, it seems that this application to fluid flows cannot match the success of photoelasticity in solids. This is thought to be due to several reasons, which we will discuss in section 2.5. The task within this thesis is therefore to investigate the potential of shear rate imaging using birefringent fluids and to improve the current state of the art. In addition, new measurement techniques that are based on a polarization camera are presented, and a new type of birefringent fluid based on cellulose nanocrystals is studied.

1.2. Thesis structure

The main part of the thesis is composed of five papers. Four of them are journal papers that have been published in peer-reviewed journals. The fifth paper is a conference paper (with peer-reviewed acceptance) outlining the corresponding oral presentation delivered at that conference.

Prior to the main part of the thesis, we begin with a theory section, in which we present most of the physical concepts that the publications consider. The intention of this is to give the reader some additional background information. Part of section 2.2, “Stokes parameters and Mueller matrices”, is also presented and discussed in the papers. However, as Stokes parameters and Mueller matrices are

central elements in this thesis, we have introduced these concepts separately and comprehensively.

The titles of the five papers are:

1. Calibration of a polarization image sensor and investigation of influencing factors
2. Two-dimensional birefringence measurement technique using a polarization camera
3. Optical characterization method for birefringent fluids using a polarization camera
4. Birefringent properties of aqueous cellulose nanocrystal suspensions
5. Shear rate imaging using a polarization camera and a birefringent aqueous cellulose nanocrystal suspension

They have been arranged thematically and in a logical order (It is worth noting that the chronological order of publication is 3,2,1,4,5). The first paper discusses the calibration of a polarization camera and investigates the relevant parameters. We utilized a polarization camera throughout the entire project, and it is therefore reasonable to start by introducing this measurement device. The second paper presents a two-dimensional birefringence measurement technique that is based on the use of a polarization camera. The technique can be applied to any form of birefringence, including both photoelasticity and flow birefringence. The third paper uses a slightly modified version of the technique presented in the second paper to measure the optical response of a birefringent fluid in a Taylor-Couette flow. The fourth paper applies the measurement technique presented in the third paper to characterize the optical response to shear of aqueous cellulose nanocrystal (CNC) suspensions. These kind of CNC suspensions are a rather new type of birefringent fluid. In the fifth paper, the conference paper, we describe the

design of a two-dimensional flow channel and how we measure the flow induced birefringence with the help of our previously described measurement techniques. We use aqueous CNC suspensions similar to the ones we have characterized before and compare the optically determined shear rates to numerical simulations.

We end the thesis by reviewing our work and putting it into an overall context. Additionally, new research opportunities that we consider to be potentially interesting are described and we propose further work in this field of research.

2. Theory

2.1. Birefringence explained on a linear retarder

If a material is a linear retarder, then linear polarized light is able to travel through it without a change in the state of polarization, provided that the polarization direction is parallel to one of the two main refractive index axes. We note that also elliptic retarders exist, where two states of orthogonal elliptic polarization can travel through the retarder and have the same state of polarization afterwards (Sarma, 1977; Yu, 2016). More information on this can be found in the literature (Jones, 1942; P. L. Lin et al., 2008). Fig. 2.1 illustrates birefringence for the example of a linear retarder. Linear polarized light at position 1 is represented as an electromagnetic wave with angular frequency ω and wavenumber $k = 2\pi/\lambda$. Parameter λ is the wavelength, t the time and x the spatial position. We define c_0 as the speed of light in vacuum (and accordingly λ_0 and k_0) and c_1, c_2 as the speed along the corresponding refractive indices $n_{1,2} = c_0/c_{1,2}$. The angular wavenumbers along the refractive indices can then be calculated as

$$k_{1,2} = \frac{\omega}{c_{1,2}} = n_{1,2} \cdot \frac{\omega}{c_0} = n_{1,2} \cdot k_0 . \tag{2.1}$$

A linear retarder has two main refractive indices. We define n_1 to be the fast axis, meaning $n_1 < n_2$, and describe its position with the angular coordinate α. When the linear polarized light from position 1 enters the birefringent medium (indicated by the grey background at position 2), the electromagnetic wave can be decomposed into two linear polarized components, each travelling along one of the main refractive index axes. Each component travels at a different speed and

with a different wavenumber. After leaving the birefringent medium of length *L*, the retardation along the refractive index axes can be modelled by additional phase offsets $\delta_{1,2} = -k_{1,2} \cdot L$. The phase difference between the two components is then given as

$$\delta = \delta_1 - \delta_2 = (k_2 - k_1) \cdot L = (n_2 - n_1) \cdot \frac{2\pi}{\lambda_0} L = \Delta n \cdot \frac{2\pi}{\lambda_0} L\,, \tag{2.2}$$

where

$$\Delta n = n_2 - n_1 \tag{2.3}$$

is the difference between the refractive indices. Generally, the two components will be out of phase when leaving the birefringent medium and thus the light at position 3 will have a different state of polarization. It may be linear, circular or elliptical polarized. By knowing the state of polarization at position 1 and measuring the state of polarization at position 3, the amount of retardation $\Delta n \cdot L$ can be derived.

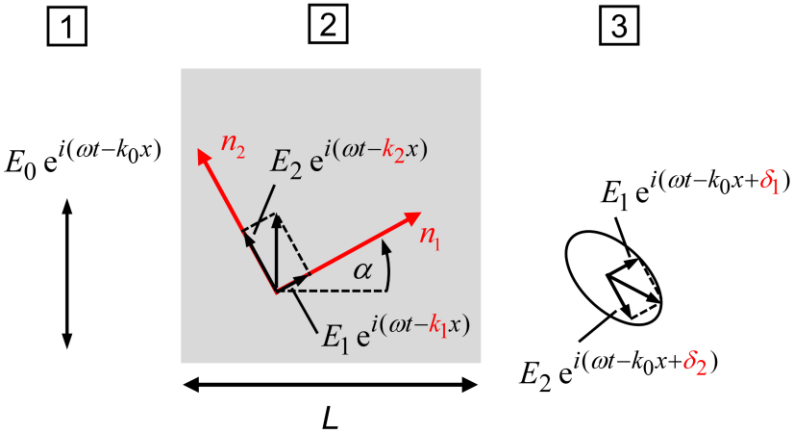

Fig. 2.1. Linear polarized light travelling through a birefringent material and exiting with a changed state of polarization.

2.2. Stokes parameters and Mueller matrices

Stokes parameters and Mueller matrices are useful tools when describing polarized light and modelling optical elements. Here, we briefly introduce the expressions and formulations used in this thesis. For more information, we recommend consulting one of these books (Chipman, 1994; Chipman et al., 2018b; Collett, 2005; Fuller, 1995a).

Stokes parameters

The Stokes vector with its four Stokes parameters S_0, S_1, S_2, S_3 is defined as (Chipman, 1994, p. 22.8-22.9)

$$\vec{S} = \begin{bmatrix} S_0 \\ S_1 \\ S_2 \\ S_3 \end{bmatrix} = \begin{bmatrix} I_0 + I_{90} \\ I_0 - I_{90} \\ I_{45} - I_{135} \\ I_R - I_L \end{bmatrix}, \tag{2.4}$$

where $I_0, I_{45}, I_{90}, I_{135}$ are, as marked by the subscripts, the intensities of light in directions 0°, 45°, 90°, 135° defined with respect to an arbitrary direction. They can be measured by placing a linear polarizer accordingly. The intensity passing the polarizer placed in this manner is the desired quantity. Ideally, the equation $S_0 = I_0 + I_{90} = I_{45} + I_{135}$ holds. Intensities I_R, I_L correspond to the right and left circular polarization. Additional components such as circular polarizers are necessary for their measurement. Generally, the Stokes vector is defined in terms of six flux measurements. Choosing intensities such as in Eq. (2.4) is beneficial when working with intensity measurements obtained by orientating linear polarizers. The Stokes parameters for elliptically polarized light (fully polarized) can also be expressed in a fixed (x,y) basis by means of two perpendicular electromagnetic waves (increasing phase convention)

$$\begin{aligned} E_x &= E_{0x}\, e^{i(\omega t - kz + \delta_x)}, \\ E_y &= E_{0y}\, e^{i(\omega t - kz + \delta_y)}, \end{aligned} \tag{2.5}$$

giving (Collett, 2005, p. 13):

$$\begin{bmatrix} S_0 \\ S_1 \\ S_2 \\ S_3 \end{bmatrix} = \begin{bmatrix} E_x E_x^* + E_y E_y^* \\ E_x E_x^* - E_y E_y^* \\ E_x E_y^* + E_y E_x^* \\ i(E_x E_y^* - E_y E_x^*) \end{bmatrix} = \begin{bmatrix} E_{0x}^2 + E_{0y}^2 \\ E_{0x}^2 - E_{0y}^2 \\ 2E_{0x}E_{0y}\cos\delta \\ 2E_{0x}E_{0y}\sin\delta \end{bmatrix}, \tag{2.6}$$

where *i* is the imaginary number, * the complex conjugate and $\delta = \delta_y - \delta_x$ the phase difference. With the notation in Eq. (2.6) the relation between S_2 and S_3 becomes clearer. However, this expression requires the light to be fully polarized.

The degree of polarization (DOP), the degree of linear polarization (DOLP) and the degree of circular polarization (DOCP) are defined as

$$\begin{aligned} \mathrm{DOP} &= \frac{\sqrt{S_1^2 + S_2^2 + S_3^2}}{S_0}, \\ \mathrm{DOLP} &= \frac{\sqrt{S_1^2 + S_2^2}}{S_0}, \\ \mathrm{DOCP} &= \frac{S_3}{S_0}. \end{aligned} \tag{2.7}$$

It is worth noting that

$$S_0^2 \geq S_1^2 + S_2^2 + S_3^2 \tag{2.8}$$

and hence $0 \leq \mathrm{DOP} \leq 1$. Similarly, $0 \leq \mathrm{DOLP} \leq 1$ but $-1 \leq \mathrm{DOCP} \leq 1$. If light is only partially polarized (DOP<1), the Stokes vector can be considered as a superposition of a fully polarized Stokes vector $\vec{S}_P$ and an unpolarized Stokes vector $\vec{S}_U$ (Chipman, 1994, p. 22.9),

$$\vec{S} = \vec{S}_P + \vec{S}_U = \mathrm{DOP} \begin{bmatrix} S_0 \\ S_1/\mathrm{DOP} \\ S_2/\mathrm{DOP} \\ S_3/\mathrm{DOP} \end{bmatrix} + (1 - \mathrm{DOP}) \begin{bmatrix} S_0 \\ 0 \\ 0 \\ 0 \end{bmatrix}. \tag{2.9}$$

The first Stokes parameter S_0 relates to the total intensity. A normalized form is therefore given as

$$\vec{S}_N = \frac{1}{S_0} \vec{S}. \tag{2.10}$$

In this thesis, the linear components of the normalized and fully polarized part of the Stokes vector will be used frequently. The expressions

$$S_{1_{P,N}} = \frac{S_1}{S_0 \cdot \mathrm{DOP}}$$
$$S_{2_{P,N}} = \frac{S_2}{S_0 \cdot \mathrm{DOP}} \tag{2.11}$$

follow directly from Eq. (2.9) and Eq. (2.10). The polarization ellipse describes the oscillation of the electric (and magnetic) field vectors rotating clockwise or counter-clockwise. If *a* is the length of the major axis and *b* the length of the minor, the ellipse can be described by two parameters, the orientation angle of the major axis, also known as azimuth, $\psi(0 \le \psi \le \pi)$; and the ellipticity $\varepsilon(0 \le \varepsilon \le 1)$ (Chipman et al., 2018b, p. 73)

$$\psi = \frac{1}{2}\arctan\left(\frac{S_2}{S_1}\right), \tag{2.12}$$

$$\varepsilon = \frac{b}{a} = \frac{|S_3|}{\sqrt{S_1^2 + S_2^2 + S_3^2} + \sqrt{S_1^2 + S_2^2}}. \tag{2.13}$$

Mueller matrices

Mueller matrices are 4x4 matrices and are used together with Stokes vectors to describe optical elements. They transform the Stokes parameters of the incident light to the Stokes parameters of the outgoing light

$$\vec{S}_{out} = \underline{M} \cdot \vec{S}_{in}. \tag{2.14}$$

Mueller matrices are associative but not commutative. The Mueller matrix of a linear polarizer oriented at ϕ is

$$P(\phi) = \frac{1}{2}\begin{bmatrix} 1 & \cos 2\phi & \sin 2\phi & 0 \\ \cos 2\phi & \cos^2 2\phi & \sin 2\phi \cos 2\phi & 0 \\ \sin 2\phi & \sin 2\phi \cos 2\phi & \sin^2 2\phi & 0 \\ 0 & 0 & 0 & 0 \end{bmatrix}, \tag{2.15}$$

and that of a linear retarder $X(\delta,\alpha)$ inducing a phase difference δ with a fast axis orientation α,

$$X(\delta,\alpha) = \begin{bmatrix} 1 & 0 & 0 & 0 \\ 0 & \cos^2 2\alpha + \sin^2 2\alpha \cos\delta & \cos 2\alpha \sin 2\alpha(1-\cos\delta) & -\sin 2\alpha \sin\delta \\ 0 & \cos 2\alpha \sin 2\alpha(1-\cos\delta) & \sin^2 2\alpha + \cos^2 2\alpha \cos\delta & \cos 2\alpha \sin\delta \\ 0 & \sin 2\alpha \sin\delta & -\cos 2\alpha \sin\delta & \cos\delta \end{bmatrix}. \tag{2.16}$$

Fig. 2.2 shows a series of the two optical elements represented by the Mueller matrices in Eq. (2.15) and Eq. (2.16). Light from a light source is linear polarized and then travels through a linear retarder. The situation is similar to the one depicted in Fig. 2.1 (only that now the linear polarizer can be actively rotated). If we assume that our light source emits unpolarized light of intensity I_s, corresponding to a Stokes vector

$$\vec{S}_{in} = \begin{bmatrix} I_s \\ 0 \\ 0 \\ 0 \end{bmatrix}, \tag{2.17}$$

the outgoing light can be modelled as

$$\vec{S}_{out} = X(\delta,\alpha)\cdot P(\phi)\cdot \vec{S}_{in}, \tag{2.18}$$

resulting in

$$\begin{aligned} S_0 &= \frac{I_S}{2}, \\ S_1 &= \frac{I_S}{4}\left(\cos 2\phi + \cos 2\phi\,\cos\delta + \cos[2\phi - 4\alpha](1-\cos\delta)\right), \\ S_2 &= \frac{I_S}{4}\left(\sin 2\phi + \sin 2\phi\,\cos\delta - \sin[2\phi - 4\alpha](1-\cos\delta)\right), \\ S_3 &= \frac{I_S}{2}\sin[2\alpha - 2\phi]\sin\delta. \end{aligned} \tag{2.19}$$

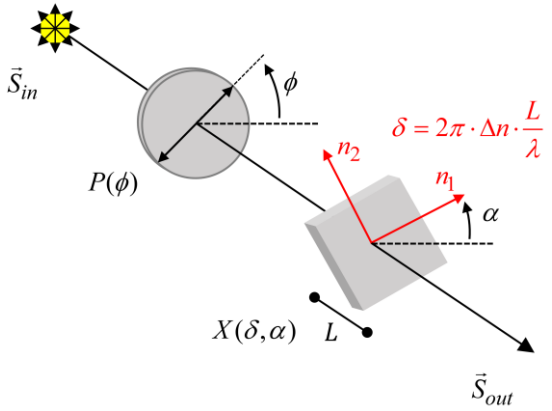

Fig. 2.2. Light passing through a linear polarizer $P(\phi)$ and a linear retarder $X(\delta,\alpha)$.

The polarizer $P(\phi)$ blocks half of the light and hence halves the total intensity. No reduction comes from the linear retarder, as it merely changes the state of polarization. We would like to discuss two special cases. First, if the phase

difference of the linear retarder is a multiple of $\pi/2$ (a so-called quarter wave plate),

$$\delta = N \cdot \frac{\pi}{2}, \qquad \text{with } N = 1, 2, 3, \ldots \tag{2.20}$$

and, furthermore, if the relative position between polarizer and fast axis is a multiple of $\pi/4$,

$$\alpha - \phi = N \cdot \frac{\pi}{4}, \qquad \text{with } N = 1, 2, 3, \ldots \tag{2.21}$$

the combination of polarizer and quarter wave plate will form a circular polarizer, meaning that the resulting light will be fully circular polarized, $|S_3| = S_0$.

The second special case concerns only the relative position between polarizer and refractive index axes. If

$$\alpha - \phi = N \cdot \frac{\pi}{2}, \qquad \text{with } N = 0, 1, 2, \ldots \tag{2.22}$$

then the outgoing light will have the state of polarization

$$\vec{S}_{out} = \frac{1}{2}\begin{bmatrix} 1 \\ \cos 2\phi \\ \sin 2\phi \\ 0 \end{bmatrix} \tag{2.23}$$

that equals $P(\phi) \cdot \vec{S}_{in}$, meaning that the linear retarder has no effect. Eq. (2.22) applies when the linear polarization is in line with one of the refractive index axes and in this case the light does not split into two components that travel at different

velocities but all of the light travels along one axis and hence no birefringence occurs.

2.3. Strain and shear rates in a two-dimensional fluid flow

The symmetric strain rate tensor for a two-dimensional fluid flow is given as (Kundu et al., 2012, p. 76)

$$\dot{\varepsilon} = \begin{bmatrix} \dot{\varepsilon}_{xx} & \dot{\varepsilon}_{xy} \\ \dot{\varepsilon}_{xy} & \dot{\varepsilon}_{yy} \end{bmatrix} = \begin{bmatrix} \dfrac{\partial u}{\partial x} & \dfrac{1}{2}\left(\dfrac{\partial u}{\partial y} + \dfrac{\partial v}{\partial x}\right) \\ \dfrac{1}{2}\left(\dfrac{\partial u}{\partial y} + \dfrac{\partial v}{\partial x}\right) & \dfrac{\partial v}{\partial y} \end{bmatrix}, \tag{2.24}$$

with *u* and *v* being the velocity components in x and y direction in a cartesian coordinate system. If we assume the flow to be incompressible, the divergence of the velocity field is zero,

$$\frac{\partial u}{\partial x} + \frac{\partial v}{\partial y} = 0\,. \tag{2.25}$$

Note that stress and strain rates are related. For a Newtonian, incompressible, and isotropic fluid the stress tensor is given as (Kundu et al., 2012, p. 113)

$$\sigma_{ij} = -p \cdot \delta_{ij} + \mu\left(\frac{\partial u_i}{\partial x_j} + \frac{\partial u_j}{\partial x_i}\right). \tag{2.26}$$

The maximum strain rate $\dot{\varepsilon}_{\max}$ can then be expressed as (derived for example with the help of Mohr's circle)

$$\dot{\varepsilon}_{\max} = \sqrt{\left(\frac{\partial u}{\partial x}\right)^2 + \frac{1}{4}\left(\frac{\partial u}{\partial y} + \frac{\partial v}{\partial x}\right)^2} \,. \tag{2.27}$$

The maximum strain rate $\dot{\varepsilon}_{\max}$ is the positive eigenvalue and the maximum strain rate axis the corresponding eigenvector of the matrix in Eq. (2.24). Let us now define a local set of cartesian coordinates (ξ, η), with ξ pointing in the direction of the flow. The strain rate tensor for an incremental fluid element in the coordinate system (ξ, η) will therefore have the form

$$\dot{\varepsilon} = \begin{bmatrix} \dot{\varepsilon}_{\xi\xi} & \frac{1}{2}\dot{\gamma}_{\xi\eta} \\ \frac{1}{2}\dot{\gamma}_{\xi\eta} & -\dot{\varepsilon}_{\xi\xi} \end{bmatrix}, \tag{2.28}$$

with

$$\dot{\varepsilon}_{\xi\xi} = \frac{\partial u}{\partial \xi} \tag{2.29}$$

being the strain rate in flow direction, and

$$\frac{1}{2}\dot{\gamma}_{\xi\eta} = \dot{\varepsilon}_{\xi\eta} = \frac{1}{2}\left(\frac{\partial u}{\partial \eta} + \frac{\partial v}{\partial \xi}\right) \tag{2.30}$$

the corresponding shear rate. Note that shear rates are defined as $\dot{\gamma}_{ij} = 2 \cdot \dot{\varepsilon}_{ij}$. Equations (2.27) can now be written as

$$\dot{\varepsilon}_{\max} = \sqrt{\dot{\varepsilon}_{\xi\xi}^2 + \frac{1}{4} \cdot \dot{\gamma}_{\xi\eta}^2} \,. \tag{2.31}$$

Following the idea discussed by Wayland (1960, 1964), we define Λ_0 as the angle between the maximum strain rate axis and the direction of flow,

$$\Lambda_0 = \frac{1}{2}\arctan 2\left(\frac{\dot{\gamma}_{\xi\eta}}{2\cdot\dot{\varepsilon}_{\xi\xi}}\right). \tag{2.32}$$

This gives

$$\dot{\varepsilon}_{\xi\xi} = \dot{\varepsilon}_{\max}\cos 2\Lambda_0\,, \tag{2.33}$$

and

$$\frac{1}{2}\dot{\gamma}_{\xi\eta} = \dot{\varepsilon}_{\max}\sin 2\Lambda_0\,. \tag{2.34}$$

Figure 2.3 shows different strain rate tensors in Mohr's circle. We can see that the maximum strain rate $\dot{\varepsilon}_{\max}$ is the radius of the circle. The eigenvectors are located at $\dot{\varepsilon}_{ii} = \dot{\varepsilon}_{\max}$, $\dot{\gamma}_{ij} = 0$ and $\dot{\varepsilon}_{ii} = -\dot{\varepsilon}_{\max}$, $\dot{\gamma}_{ij} = 0$. The angle between the position of the eigenvectors and the ξ-axis can be calculated using simple geometrical relations. With the help of Mohr's circle, Eq. (2.32) can easily be understood. Therefore, every strain rate tensor in Eq. (2.28) can be transformed into a representation with strain rates only,

$$\dot{\varepsilon} = \begin{bmatrix} \dot{\varepsilon}_{\max} & 0 \\ 0 & -\dot{\varepsilon}_{\max} \end{bmatrix}. \tag{2.35}$$

Merely the axes are rotated by angle Λ_0, which therefore describes the relative position between flow direction and strain rate tensor.

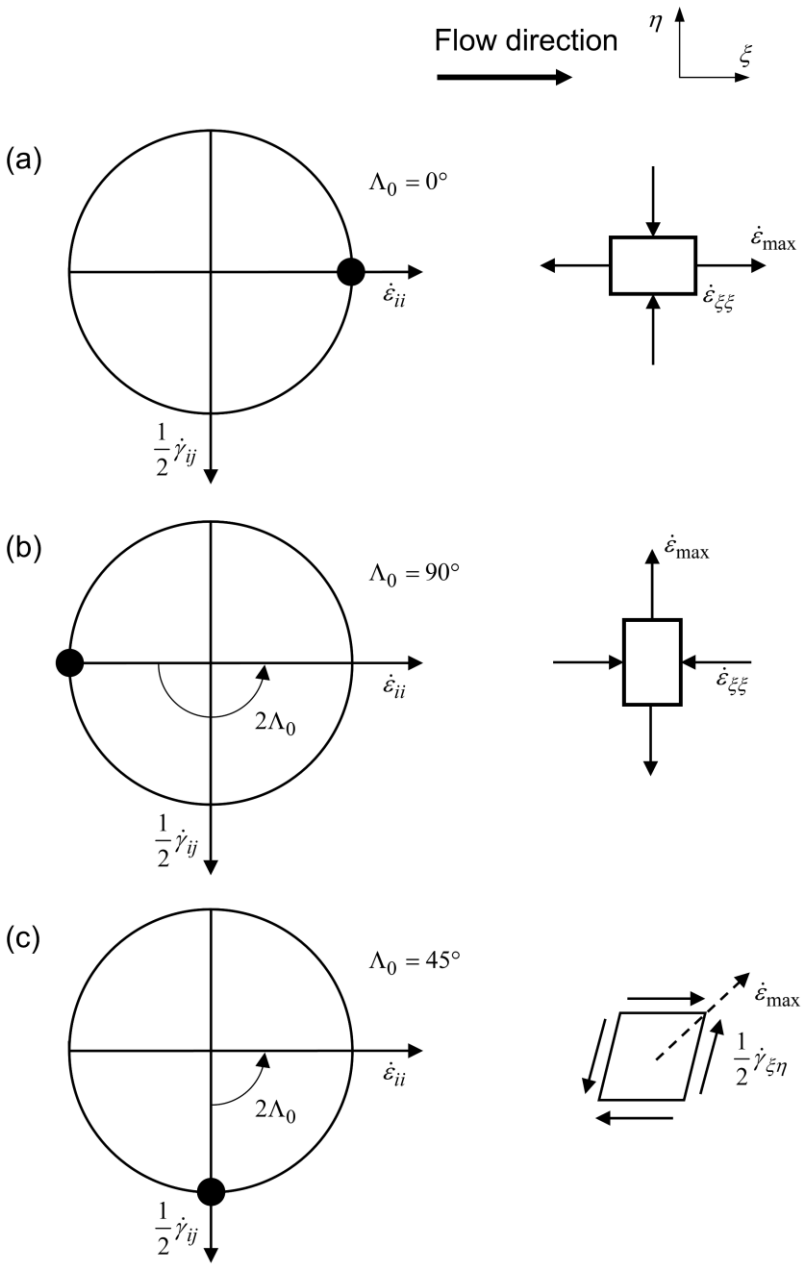
Flow direction
η
ξ
(a)
$\Lambda_0 = 0°$
$\dot{\varepsilon}_{ii}$
$\frac{1}{2}\dot{\gamma}_{ij}$
$\dot{\varepsilon}_{\max}$
$\dot{\varepsilon}_{\xi\xi}$
(b)
$\Lambda_0 = 90°$
$\dot{\varepsilon}_{ii}$
$2\Lambda_0$
$\frac{1}{2}\dot{\gamma}_{ij}$
$\dot{\varepsilon}_{\max}$
$\dot{\varepsilon}_{\xi\xi}$
(c)
$\Lambda_0 = 45°$
$\dot{\varepsilon}_{ii}$
$2\Lambda_0$
$\frac{1}{2}\dot{\gamma}_{ij}$
$\dot{\varepsilon}_{\max}$
$\frac{1}{2}\dot{\gamma}_{\xi\eta}$

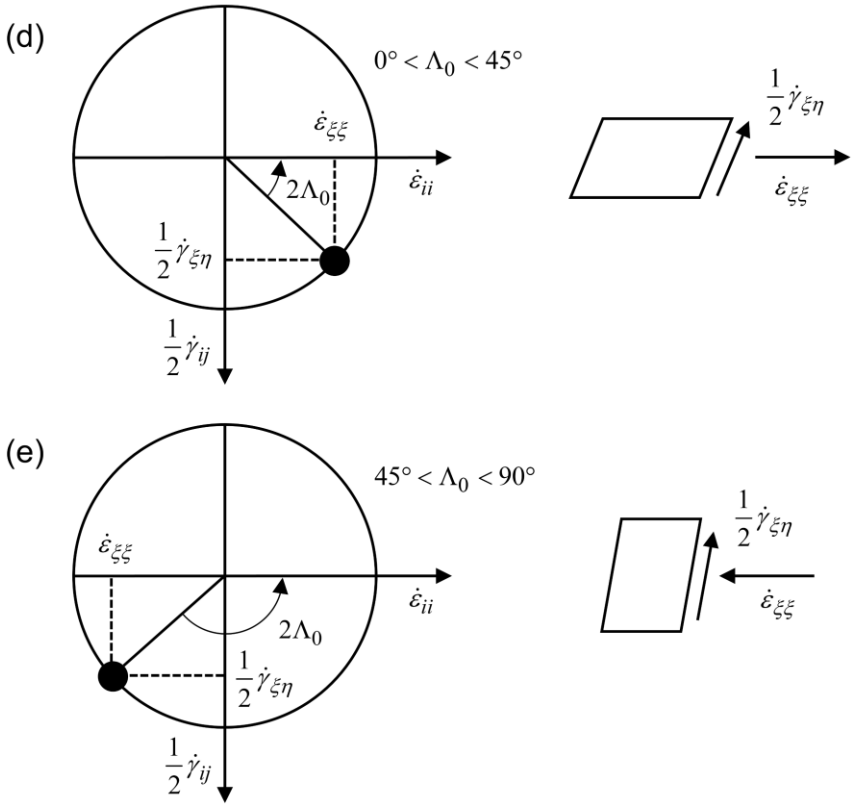

Fig. 2.3. Mohr's circles for various two-dimensional strain rate tensors in (ξ,η) coordinates. The ξ-axis is in the direction of flow. (a)-(e) illustrate different situations.

We would now like to look at different strain rate tensors given in the (ξ,η) coordinate system, and their corresponding representation in Mohr's circle. Different strain rate tensors describe different flow situations. Situation (a) and (b) in Fig. 2.3 describe the flow down the centreline of a symmetrically converging and diverging channel, respectively. In (a), the fluid is accelerated in the direction of flow whereas it is slowed down in (b). Situation (c) describes a

shearing flow where different layers of the fluid move parallel to each other but at different velocities. A Taylor-Couette flow and a flow through a straight channel (plane Poiseuille flow) are two typical examples. Situations (d) and (e) can be seen as a combination of (a) and (c), and (b) and (c), respectively.

In this thesis we often use the term 'shear rate' for any type of flow. Due to the assumed incompressibility, Eq. (2.25), we can find a reference coordinate system that allows us to transform any strain rate tensor to the form

$$\dot{\varepsilon} = \begin{bmatrix} 0 & \frac{1}{2}\dot{\gamma} \\ \frac{1}{2}\dot{\gamma} & 0 \end{bmatrix}, \tag{2.36}$$

with $\dot{\gamma}/2 = \dot{\varepsilon}_{\max}$ being the characteristic shear rate. Every flow situation can therefore be expressed as a state of pure shear rate. This quickly becomes clear if we look at the Mohr's circles in Fig. 2.3. All center points are in the origin of the $(\dot{\varepsilon}_{i,i}, \dot{\gamma}_{i,j}/2)$ coordinate system. Note that generally the center points can move along the $\dot{\varepsilon}_{i,i}$-axis (if it was not for the two-dimensional incompressibility condition). If we rotate the reference coordinate system by -45° for situation (a) and +45° for situation (b) in Fig. 2.3, the strain rate tensors will take the form given in Eq. (2.36). Talking of measuring shear rates therefore comprises all (incompressible, two-dimensional) flow fields.

Alternative definition

In section 6 we define the maximum strain rate as

$$\dot{\varepsilon}_{\max} = \sqrt{2 \cdot \dot{\varepsilon} : \dot{\varepsilon}} = \sqrt{4 \cdot \left(\frac{\partial u}{\partial x}\right)^2 + \left(\frac{\partial u}{\partial y} + \frac{\partial v}{\partial x}\right)^2} = \sqrt{4 \cdot \dot{\varepsilon}_{\xi\xi}^2 + \dot{\gamma}_{\xi\eta}^2}\,. \tag{2.37}$$

This definition corresponds to the strain rate magnitude as defined in the utilized fluid simulation software, Ansys Fluent (Ansys, 2022). Both definitions, Eq. (2.27) as well as Eq. (2.37), can be found in the literature (for example compare (Wayland, 1964) with (Peebles & Liu, 1965)). Equation (2.27) corresponds to the eigenvalue of the strain rate tensor in Eq. (2.24). However, Eq. (2.37) is more practical, as we get $\dot{\varepsilon}_{\max} = \dot{\gamma}$ for a shearing flow.

2.4. Birefringent fluids

Birefringence in a fluid occurs when elongated and deformable macromolecules (polymers) or nonspherical particles align under the effect of shear (Merzkirch, 2001). The terms shear rate or strain rate may equally be used, as they are only a matter of reference coordinate systems (not taking the flow direction into account). Merzkirch points out that "theoretically, any fluid consisting of nonspherical particles or molecules should show this effect" (Merzkirch, 2001, p. 181) and cites Boyer et al. (1978), who measured birefringence in air flows with high velocity gradients. Boyer et al. (1978) mention two other studies that report flow birefringence in gases of linear molecules: polyatomic gases (Hess, 1969), and CO_2 and N_2 (Baas, 1971). In the following however, we focus on fluids in the liquid state.

2.4.1. Characteristic properties

Birefringent fluids are characterised by two properties (Pindera & Krishnamurthy, 1978), the amount of birefringence Δn and the position of the refractive index axes in relation to the direction of flow, commonly described by the extinction angle χ. (The term extinction angle is mostly used in the context of a Taylor-Couette flow. A more general expression is "position" or "orientation of the isoclinic", as for example used by Wayland (1964)). If the Taylor-Couette

flow is viewed through two crossed linear polarizers, an isoclinic cross appears, indicating the position of the refractive index axes. The relation between Δn and the flow is also known as the flow-optic relation (Merzkirch, 2001), and it characterises the sensitivity of a birefringent fluid to shear. According to Wayland (1960, 1964), the birefringence response of suspensions composed of rigid particles to a general two-dimensional laminar flow is a function of the maximum strain rate $\dot{\varepsilon}_{\max}$ (compare section 2.3) and the flow state, expressed with angle Λ_0 (compare section 2.3). We can therefore write

$$\begin{aligned} \Delta n &= \Delta n(\dot{\varepsilon}_{\max}, \Lambda_0), \\ \chi &= \chi(\dot{\varepsilon}_{\max}, \Lambda_0). \end{aligned} \tag{2.38}$$

For example, the flow field given in Fig. 2.3 (a) leads to $\chi = 0°$ regardless of the strain rate, whereas a Taylor-Couette flow with shear rate $\dot{\gamma}$ gives $\chi = 45°$ for $\dot{\gamma} \to 0$, and $\chi = 0°$ for $\dot{\gamma} \to \infty$ (Scheraga et al., 1951).

2.4.2. Applications

Birefringent fluids are of interest for two reasons. First, they can be used to investigate the alignment of particles and macromolecules as well as for optical rheometry (Fuller, 1995a; Janeschitz-Kriegl, 1983). Second, they can be utilized to visualize and study fluid flows (Pih, 1980). There are several literature references available for both areas of application. We cite many of them in the papers accordingly.

Schneider (2013, pp. 34–35) lists certain requirements that a birefringent fluid should meet to be suitable for flow measurement studies. They can be briefly summarized as: Optical aspects (birefringence and transparency); rheology;

availability; and manageability (non-toxic and easy to prepare). Schneider also gives an overview of various birefringent fluids (Schneider, 2013, pp. 36–41).

2.5. Streaming birefringence in fluids vs. photoelasticity in solids

As mentioned earlier, photoelasticity is an established experimental method for analysing stress and strain fields in solids. There are many textbooks available on this topic (for example (Föppl & Mönch, 1950; Ramesh, 2000; Wolf, 1961)). Current work has been focusing on digital photoelasticity (Ramesh & Sasikumar, 2020).

The following assumes the solid to be linear elastic and isotropic. The stress-optic law for two-dimensional photoelasticity is given as (Ramesh, 2000, pp. 9–10)

$$\delta = \frac{2\pi \cdot L}{\lambda_0} \cdot C \cdot (\sigma_1 - \sigma_2)\,, \tag{2.39}$$

where δ is the phase difference, L the path length, λ_0 the speed of light in vacuum, σ_1, σ_2 are the principal stresses, and C the stress-optic coefficient. The directions of the main refractive indices n_1 and n_2 correspond to the directions of σ_1 and σ_2. The stress-optic coefficient C can be interpreted when comparing Eq. (2.39) to Eq. (2.2), resulting in

$$\Delta n = C \cdot (\sigma_1 - \sigma_2)\,. \tag{2.40}$$

The amount of birefringence Δn is thus a linear function of the difference in principal stresses. By making use of the constitutive equations, with E being Young's modulus and ν Poisson's ratio, we can write

$$(\sigma_1 - \sigma_2) = \frac{E}{1+\nu}(\varepsilon_1 - \varepsilon_2)\,. \tag{2.41}$$

With this, we can express the stress-optic law by means of strains, giving

$$\delta = \frac{2\pi \cdot L}{\lambda_0} \cdot C^* \cdot (\varepsilon_1 - \varepsilon_2) \tag{2.42}$$

and

$$\Delta n = C^* \cdot (\varepsilon_1 - \varepsilon_2)\,, \tag{2.43}$$

where C^* is now the strain-optic coefficient with

$$C^* = C \cdot \frac{E}{1+\nu}\,. \tag{2.44}$$

Concluding, photoelasticity in solids is based on two properties:

1. The amount of birefringence is linearly dependent on the difference in principal strains / stresses.
2. The directions of n_1, n_2 correspond to the directions of $\varepsilon_1, \varepsilon_2$ (and to σ_1, σ_2)

In fluid flows, stresses lead to strain rates rather than strains. So ideally, Equation (2.43) should translate into

$$\Delta n = C^* \cdot (\dot{\varepsilon}_1 - \dot{\varepsilon}_2) = C^* \cdot (\dot{\varepsilon}_1 - (-\dot{\varepsilon}_1)) = C^* \cdot 2\dot{\varepsilon}_{\max} = C^* \cdot \dot{\gamma}\,. \tag{2.45}$$

Note the use of the incompressibility $\dot{\varepsilon}_2 = -\dot{\varepsilon}_1$ (two-dimensional), as well as that $2\dot{\varepsilon}_{\max} = \dot{\gamma}$ is the diameter of Mohr's circle shown in Fig. 2.3.

Equation (2.45) does not generally hold for two reasons. The first reason is that the coefficient *C** is usually not constant. This can be seen, for example, in section 4 for Xanthan solutions and in section 6 for aqueous cellulose nanocrystal suspensions. Some studies however make certain assumptions such as assuming small shear rates in order to apply a linear relationship (for example (Schneider, 2013; Y.-D. Sun et al., 1999)). The second reason is that the flow state, expressed by angle Λ_0, is thought to affect birefringence. This aspect is discussed in section 7.

Furthermore, the directions of n_1, n_2 do not necessarily correspond with the directions of $\dot{\varepsilon}_1, \dot{\varepsilon}_2$. In fact, they only correspond with the directions of $\dot{\varepsilon}_1, \dot{\varepsilon}_2$ for situations (a) and (b) depicted in Fig. 2.3 (flow down the centreline of a symmetrically converging and diverging channel), and for situation (c) if $\dot{\gamma} \to 0$ (extinction angle close to $\chi = 45°$ for $\dot{\gamma} \to 0$, compare section 2.4.1).

2.6. Three-dimensional flow birefringence

2.6.1. Refractive index tensor

The dielectric tensor ε (note the new definition for ε here) for a nonmagnetic and transparent material is real and symmetric (Yariv et al., 2007, pp. 30–31), and is therefore orthogonally diagonalizable, giving

$$\varepsilon = \varepsilon_0 \begin{bmatrix} n_1^2 & 0 & 0 \\ 0 & n_2^2 & 0 \\ 0 & 0 & n_3^2 \end{bmatrix}, \tag{2.46}$$

where ε_0 is the vacuum permittivity and n_1, n_2, and n_3 are the principal refractive indices. If $n_1 \neq n_2 \neq n_3$, the material is referred to as a biaxial crystal (Hecht, 1998b). The dielectric tensor of a birefringent fluid in a three-dimensional flow field will have the form of Eq. (2.46). The directions of the main refractive indices do not necessarily coincide with the directions of the principal strain rates.

2.6.2. Measurement techniques

There are two common approaches to study three-dimensional flow birefringence, the integrated photoelasticity method, and the scattered-light photoelasticity method.

Integrated photoelasticity method: Following their work on integrated photoelasticity for axisymmetric flows (H. Aben & Puro, 1993), Aben and Puro (1997) published a work titled "Photoelastic tomography for three-dimensional flow birefringence studies". Similar to their previous study, they make the assumption of weak birefringence (H. K. Aben et al., 1989), and that the principal refractive index axes correspond to the directions of the principal strain rates. This approach allows to simplify the relationships so that they can be solved using the Radon inversion and hence provides a conceptual guideline for a suitable experiment. More information on the topic of integrated photoelasticity can be found in the literature, for example in (H. Aben, 1979; H. Aben et al., 2010; H. Aben & Guillemet, 1993; H. K. Aben et al., 1992; Ainola & Aben, 2005). To our knowledge, integrated photoelasticity so far has only been applied to solids (for example by Aben et al. (2005, 2010)) and no three-dimensional flow fields have been studied by means of this approach. We suppose that the rather complicated experimental design as well the requirements on the birefringent fluid are issues that need to be addressed.

Scattered-light photoelasticity method: A review of the scattered-light method is given by Ascough (1981) and the basic principles of scattered-light measurements are summarized by Pih (1980). The technique has been used in solids, for example (Kihara, 2004; Swinson et al., 1980), as well as in fluids (Ahimaz, 1970; Dupré et al., 2010; Horsmann & Merzkirch, 1981; Krishnamurthy & Pindera, 1982; McAfee & Pih, 1971). To increase the scattering effect, Schneider et al. (2012) propose adding small droplets of mineral oil to the birefringent fluid (milling yellow). Details are given by Schneider (2013).

2.6.3. Challenges

The evaluation and utilization of three-dimensional flow birefringence presents a challenging task due to several reasons. The experimental design can be difficult and has to be in accordance with the measurement technique. Some components such as the flow channel must be transparent or at least allow optical access. Ideally, these components are non-birefringent and not refractive. The integrated photoelasticity method is based on strong assumptions (see previous section), and the scattered-light photoelasticity method relies on an additional physical effect (light scattering), that has to be taken into account. The relation between strain rate tensor and dielectric tensor is most likely not straightforward. We discussed in section 2.3 the two-dimensional case and argued that the flow state affects this relation (see Eq. (2.38)). As a consequence, the strain rate tensor cannot simply be derived from the refractive index tensor and hence measuring the refractive index tensor does not automatically lead to reliable strain rates.

3. Calibration of a polarization image sensor and investigation of influencing factors

The content of this chapter has been published in (Lane, Rode, et al., 2022a):

Lane, C., Rode, D., & Rösgen, T. (2022a). Calibration of a polarization image sensor and investigation of influencing factors. *Applied Optics*, *61*(6), C37. https://doi.org/10.1364/AO.437391

Author contribution statements:

Connor Lane developed the theory, designed the experimental setup, analysed the data, and wrote the manuscript. David Rode helped to carry out the experiments and sort out the references. Thomas Rösgen developed the camera software and directed the project. All authors discussed the results and helped formulate the manuscript.

Note:

The following refers to the author version. Please refer to the original paper for the typeset version. The text is quoted verbatim; however, the citation style and the numbering of the figures and equations have been aligned to this document and are therefore changed. The figures are reprinted with permission (see copyright transfer and licensing information (Optica Publishing Group, 2022)).

Disclosures:

The authors declare no conflicts of interest.

Abstract

Polarization measurements conducted with a polarization camera using the Sony IMX 250 MZR polarization image sensor are assessed with the super-pixel calibration technique and a simple test setup. We define an error that quantifies the quality of the polarization measurements. Multiple factors influencing the measurement quality of the polarization camera are investigated and discussed. We demonstrate that polarization measurements are generally consistent throughout the sensor if not corrupted by large chief ray angles or large angles of incidence. The central 600 x 400 pixels were analyzed and it is shown that sufficiently large f-numbers no longer influence the measurement quality. We also argue that lens design and focal length have little influence on these central pixels. The findings of this study provide useful guidance for researchers using such a polarization image sensor.

3.1. Introduction

Polarization refers to the geometric orientation of a transverse electromagnetic wave, and the Stokes parameters can be used to describe the state of polarization. The corresponding Stokes vector $\vec{S}$ is defined as (Chipman, 1994)

$$\vec{S} = \begin{bmatrix} S_0 \\ S_1 \\ S_2 \\ S_3 \end{bmatrix} = \begin{bmatrix} \frac{I_0 + I_{45} + I_{90} + I_{135}}{2} \\ I_0 - I_{90} \\ I_{45} - I_{135} \\ I_R - I_L \end{bmatrix}, \tag{3.1}$$

wherein $I_0, I_{45}, I_{90}, I_{135}$ represent the intensities of the light in the directions 0°, 45°, 90°, 135°, as indicated by their subscripts. They can be measured by

orientating a linear polarizer accordingly. The intensities I_R, I_L correspond to the right and left circular polarization and their measurement requires additional components such as circular polarizers. Stokes parameters are hence defined by means of intensities and their differences and can therefore describe not only fully polarized light but non-polarized and partially polarized light as well. With known Stokes vector, the degree of polarization and its orientation can be calculated. Commercially available polarization image sensors such as the Sony IMX 250 MZR sensor (Sony Semiconductor Solutions Corporation, 2022) apply a Polarizer Filter Array (PFA) as a division-of-focal-plane polarimeter. This constitutes a four-directional polarizer. The four linear polarizers with orientation axes 0°, 45°, 90° and 135° are arranged in a specific spatial pattern, as indicated in Fig. 3.1. Each linear polarizer is covered by an on-chip micro-lens, and the passing light intensity is captured by individual sensor pixels. A set of four neighboring pixels, each with different polarizer orientations, forms what is known as a super-pixel (Powell & Gruev, 2013). With the definition in Eq. (1), each super-pixel can measure the first three Stokes parameters S_0, S_1, S_2. The fourth Stokes parameter S_3 requires knowledge of the rotational direction of the light and therefore cannot be measured with linear polarizers alone. To achieve a full Stokes imaging polarimeter, different approaches have been proposed by researchers (Li et al., 2020, 2021; Otani, 2021; Shibata et al., 2019; Vedel et al., 2011). Polarization image sensors applied in polarization cameras measure Stokes parameters with a resolution defined by the corresponding super-pixels. These types of cameras are being more frequently used in various applications (Iwata et al., 2019; Lane et al., 2021a, 2021b; Liu et al., 2020; Oba & Inoue, 2016; Sattar et al., 2020; Wolff, 1995) because of their ability to measure four different polarization directions with a single snapshot. For example, with the theory of

(Onuma & Otani, 2014), a polarization camera can measure two-dimensional birefringence with a single exposure. As polarization imaging systems are of interest in various applications (Ferraton et al., 2009; S.-S. Lin et al., 2006; Morel et al., 2006; Puttonen et al., 2009; Schechner et al., 2003; Shwartz et al., 2006; Tominaga & Kimachi, 2008; Treibitz & Schechner, 2009; Tyo et al., 2006), the increased availability of polarization cameras is thought to promote the use of such systems.

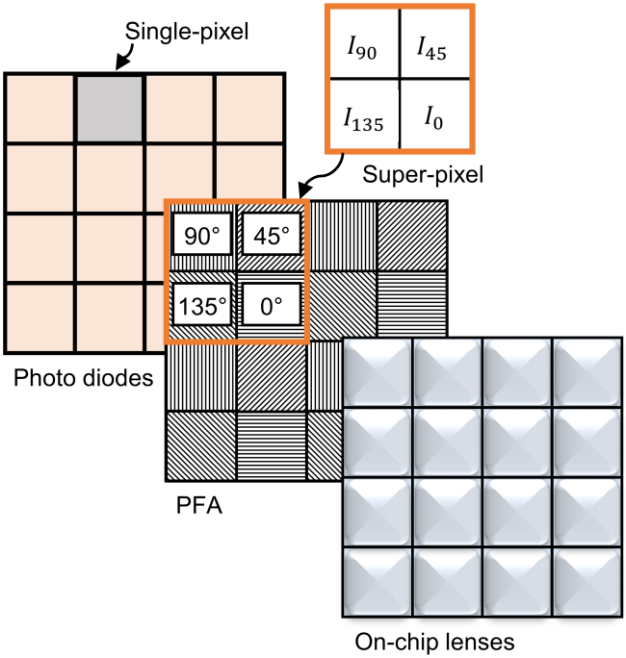

Fig. 3.1. Structure of the Sony polarization image sensor. Figure adapted from (Sony Semiconductor Solutions Corporation, 2022).

Due to the spatial arrangement, polarization measurements conducted with a polarization camera suffer from sparsity, meaning that each single-pixel senses only one polarization direction. The resulting field-of-view errors can be

corrected (Ratliff et al., 2009; Tyo et al., 2009). Besides these and general digital imaging errors such as fixed pattern noise and photon response nonuniformity (Chen et al., 2015) that occur during a sensor readout, the PFA introduces a new type of error due to imperfections in the polarization filters. Each polarization filter will have slightly different optical properties which affect transmission, orientation and the extinction ratio due to micro-polarizer non-uniformities and orientation misalignments. Various calibration techniques have been presented and summarized by Giménez et al. in (Gimenez et al., 2020; Giménez et al., 2019), such as single-pixel calibration (Hagen et al., 2019; Powell & Gruev, 2013), super-pixel calibration (Myhre et al., 2012; Powell & Gruev, 2013), adjacent super-pixel calibration (Chen et al., 2015), average analysis matrix calibration (Zhang et al., 2016) and installation calibration (Han et al., 2017). It was found that the relatively simple super-pixel method performs well and the more advanced approaches reportedly bring no significant advantages. Regarding the training data, Giménez et al. (Gimenez et al., 2020) recommend applying at least four different polarization angles and two different dynamic ranges. It was pointed out that the gap between PFA and sensor causes measurement errors that depend on the focal length and the f-number (Myhre et al., 2012). Therefore, a camera ought to be recalibrated when the focal length or the f-number are changed, as a decrease of the focal length or the f-number is said to decrease performance. York and Gruev (2012) arrived at a similar conclusion regarding the divergence of the light. To counteract this effect, the Sony IMX 250 MZR sensor places the PFA below the on-chip micro-lenses, reducing the gap between the PFA and the photo diodes. This is thought to increase performance of the polarization filtering and decrease calibration sensitivity on the focal ratio. In general, it would be convenient if one calibration were to be valid for all super-pixels, i.e. that super-pixel performance does not differ significantly within the

sensor. The intention of this study is therefore to present a practical optical setup for calibration; study any differences in the super-pixels; propose a definition of a measurement error that quantifies the polarization measurement quality and discuss other relevant aspects such as pixel position within the sensor, f-number and camera lens dependencies. This is done using a specific monochrome polarization camera utilizing the Sony IMX 250 polarization image sensor.

3.2. Material and methods

3.2.1. Optical setup

The optical setup used in this study is depicted in Fig. 3.2. A 150W EKE light bulb in a fiber optic illuminator with an IR blocking glass (Transmission >90% @ 400-690nm; Edmund Optics Inc #64-457) was used as the light source. Two color filters were applied. We generated blue-green light with a bandpass filter (CWL 493nm, FWHM 120nm; Edmund Optics Inc #46-051) and red light with a longpass filter (Cut-Off 620nm; Edmund Optics Inc #66-055). A broadband hybrid diffuser (200x200mm, Edmund Optics Inc #36-619) was used as a target on which the lenses were focused. A rotatable linear polarizer (Techspec Glass polarizer 50.8mm; Edmund Optics Inc #66-183) in a continuous manual rotation mount (Thorlabs Part RSP2/M) with an extinction ratio of 10,000:1 was placed directly in front of the lens. The camera was a monochrome polarization camera (Phoenix PHX050S-P, Lucid Vision Labs (LUCID Vision Labs, 2022)) containing the Sony IMX 250 MZR sensor (Sony Semiconductor Solutions Corporation, 2022). The sensor size is 11.1mm and the resolution of the camera is 2448 x 2048 pixels with a pixel size of 3.45 x 3.45 micrometer. This gives a spatial resolution of 1224 x 1024 (1.25 MP) super-pixels (compare Fig. 3.1).

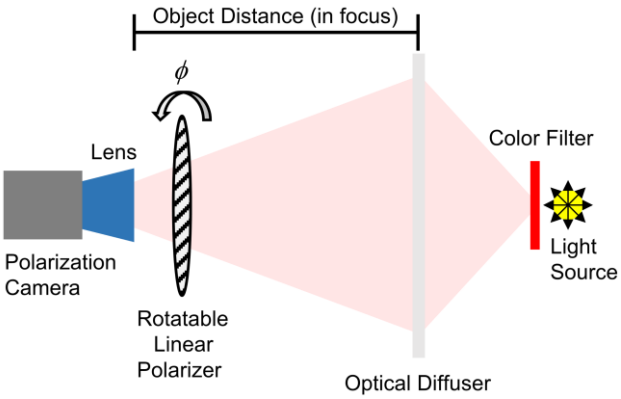

Fig. 3.2. Optical setup consisting of a rotatable linear polarizer and a polarization camera with a mounted lens, focused at an optical diffuser illuminated by color filtered light.

The various lenses that were investigated are summarized in Table 3.1. For each lens, the camera was positioned with the stated object distance to the diffuser and the focus adjusted accordingly. All available focal ratios up to a ratio of 22 were tested. The lenses chosen are commonly used types and were chosen to represent a sample within the wide spectrum of available lenses.

Table 3.1. Applied lenses and tested focal lengths, f-numbers and object distances.

Lens	Focal length (mm)	f-numbers	Object Distance (cm)
Nikon Micro-Nikkor 105mm 1:2.8	105	2.8-22	60
Nikon Micro-Nikkor 60mm 1:2.8	60	2.8-22	50
Nikon Nikkor 35-70mm 1:3.3-4.5	35, 70	3.3-22, 4.5-22	50

Nikon Nikkor 85mm 1:1.4	85	1.4-16	85
Schneider Xenon 25mm f/0.95	25	0.95-11	40
Sill TZM 1260/0.31	-	2.8-16	19
Pentax 8.5mm 1:1.5	8.5	1.5-16	20
Pentax 12.5mm 1:1.8	12.5	1.8-16	30

3.2.2. Calibration Procedure

The polarization camera was assessed by implementing the super-pixel calibration technique. The concept of this method is that the information from all four individual pixels within one super-pixel is considered. Derived quantities from the measured intensities such as degree of linear polarization and angle of linear polarization are more precise than those achieved by use of a single-pixel calibration approach. The calibration function

$$Cal(\vec{I}) = \underline{G} \cdot (\vec{I} - \vec{d}) \tag{3.2}$$

consists of a matrix $\underline{G}$, referred to as gain correction, the measured intensity vector $\vec{I} = [I_0 \quad I_{45} \quad I_{90} \quad I_{135}]^T$ and a vector $\vec{d} = [d_0 \quad d_{45} \quad d_{90} \quad d_{135}]^T$, which corrects for sensor dark noise. Equation (3.2) is well established in the literature (Powell & Gruev, 2013). However, some studies neglect the dark noise parameter $\vec{d}$ (Myhre et al., 2012). If the training data has to be considered as only partially polarized, meaning that the degree of polarization (DOP), defined as

$$\mathrm{DOP} = \frac{\sqrt{S_1^2 + S_2^2 + S_3^2}}{S_0} \tag{3.3}$$

is below 1, i.e. $\mathrm{DOP} < 1$, the Stokes vector should be considered as a superposition of a fully polarized Stokes vector $\vec{S}_P$ and an unpolarized Stokes vector $\vec{S}_U$ (Chipman, 1994)

$$\vec{S} = \vec{S}_P + \vec{S}_U = \mathrm{DOP}\begin{bmatrix} S_0 \\ S_1/\mathrm{DOP} \\ S_2/\mathrm{DOP} \\ S_3/\mathrm{DOP} \end{bmatrix} + (1-\mathrm{DOP})\begin{bmatrix} S_0 \\ 0 \\ 0 \\ 0 \end{bmatrix} \tag{3.4}$$

In the case of purely linear polarization, the fourth Stokes parameter S_3 is equal to zero, enabling the measurement of the DOP with a polarization camera. Following this approach, unpolarized light equally distributed over the 0°, 45°, 90°, 135° pixels can be treated without the necessity to add it to the parameter $\vec{d}$. The intensity values corresponding to the unpolarized Stokes vector $\vec{S}_U$ are to be subtracted prior to the calibration. In this study, it can be assumed that the training data is fully polarized (DOP=1), as the linear polarizer was placed directly in front of the lens.

The imaging model that transforms the incoming Stokes vector into the measured intensities $\vec{I}$ is modeled as

$$\vec{I} = \underline{A}\vec{S} + \vec{d}\,. \tag{3.5}$$

The ideal transfer function $\underline{A}$ is

$$\underline{A}_{ideal} = \frac{1}{2}\begin{bmatrix} 1 & 1 & 0 & 0 \\ 1 & 0 & 1 & 0 \\ 1 & -1 & 0 & 0 \\ 1 & 0 & -1 & 0 \end{bmatrix}. \tag{3.6}$$

The gain correction matrix for the calibration function of a super-pixel is calculated as:

$$\underline{G} = \underline{A}_{ideal} \cdot \underline{A}^{+}, \tag{3.7}$$

where $\underline{A}^{+}$ is the pseudo-inverse of the measured transfer function $\underline{A}$. This approach calibrates the measured intensities to $\vec{I}_{ideal}$, so that they correspond to an ideal transfer function $\underline{A}_{ideal}$

$$Cal(\vec{I}) = \underline{G}(\vec{I} - \vec{d}) = \underline{A}_{ideal}\,\underline{A}^{+}(\underline{A}\vec{S} + \vec{d} - \vec{d}) = \underline{A}_{ideal}\,\vec{S} = \vec{I}_{ideal}\,. \tag{3.8}$$

For each calibration, training data for six different (linear) polarization angles {0°, 30°, 60°, 90°, 120°, 150°} at each of the three levels of dynamic range {50%, 70%, 90%} are acquired. This is considered to provide sufficient training data for the calibration (Gimenez et al., 2020). For each angle and at each dynamic range level, 10 images were taken and averaged. This results in a total of 180 images per calibration. The different dynamic range levels were obtained by varying the set exposure time. The images were taken at 12-bit resolution and without additional electronic gain (0 dB). For each lens, each f-number, wavelength and distance setting, the exposure time was adjusted so that the desired dynamic ranges were obtained. We use the normalized Stokes vector definition:

$$\vec{S}_N = \frac{1}{S_0}\vec{S} = \frac{2}{I_0 + I_{45} + I_{90} + I_{135}}\vec{S}, \tag{3.9}$$

and normalize intensity vector and dark noise vector accordingly

$$\vec{I}_N = \frac{2}{I_0 + I_{45} + I_{90} + I_{135}} \begin{bmatrix} I_0 \\ I_{45} \\ I_{90} \\ I_{135} \end{bmatrix}, \tag{3.10}$$

and

$$\vec{d}_N = \frac{2}{I_0 + I_{45} + I_{90} + I_{135}} \begin{bmatrix} d_0 \\ d_{45} \\ d_{90} \\ d_{135} \end{bmatrix}, \tag{3.11}$$

so that we can rewrite Eq. (3.5) as:

$$\vec{I}_N - \vec{d}_N = \underline{A}\vec{S}_N . \tag{3.12}$$

The rotatable linear polarizer was aligned to the 0° direction of the polarization camera. However, as the manual arrangement with its 2° increment scale could introduce alignment errors, a misalignment correction factor $\Delta\phi$ is introduced. The normalized Stokes vector of linearly polarized light with polarization angle ϕ can be calculated with Mueller matrices. Together with the misalignment correction factor $\Delta\phi$, this leads to

$$\vec{S}_{N,linear}(\phi) = \begin{bmatrix} 1 \\ \cos 2(\phi + \Delta\phi) \\ \sin 2(\phi + \Delta\phi) \\ 0 \end{bmatrix}. \tag{3.13}$$

The misalignment correction factor $\Delta\phi$ is estimated in an optimization routine by fitting the measured Stokes parameters $S_{1_N}(\phi)$ and $S_{2_N}(\phi)$ to the expected distributions in Eq. (3.13). For known $\vec{I}_N, \vec{d}_N$ and $\vec{S}_N$, the matrix $\underline{A}$ in Eq. (3.12) is estimated by a second optimization routine with starting point $\underline{A}_{ideal}$. For the fitting of Eqs. (3.12) and (3.13), all three dynamic range levels were considered. We propose a relative error as the difference between measured normalized intensity vector $\vec{I}_{N,linear}$ and calibrated (ideal) normalized intensity vector $\vec{I}_{N,linear,ideal}$ in relation to the latter. By making use of the compatibility between Euclidean and Frobenius norm, indicated with $\|\ \|_2$ and $\|\ \|_F$, we obtain

$$\begin{aligned}
&\frac{\left\|\vec{I}_{N,linear} - \vec{I}_{N,linear,ideal}\right\|_2}{\left\|\vec{I}_{N,linear,ideal}\right\|_2} \\
&= \frac{\left\|\underline{A}\,\vec{S}_{N,linear} - \underline{A}_{ideal}\,\vec{S}_{N,linear}\right\|_2}{\left\|\underline{A}_{ideal}\,\vec{S}_{N,linear}\right\|_2} = \frac{\left\|(\underline{A} - \underline{A}_{ideal})\cdot\vec{S}_{N,linear}\right\|_2}{\frac{\sqrt{6}}{2}} \\
&\le \frac{2}{\sqrt{6}}\left\|\underline{A} - \underline{A}_{ideal}\right\|_F \left\|\vec{S}_{N,linear}\right\|_2 = \frac{2}{\sqrt{3}}\left\|\underline{A} - \underline{A}_{ideal}\right\|_F .
\end{aligned} \tag{3.14}$$

For the equation above, it is important to note that the Euclidean norm of the normalized linear Stokes vector in Eq. (3.13) is $\sqrt{2}$. We define the result of Eq. (3.14) as our error estimation *Err*

$$Err := \frac{2}{\sqrt{3}}\left\|\underline{A} - \underline{A}_{ideal}\right\|_F . \tag{3.15}$$

It will therefore serve as a parameter that quantifies the amount of required calibration and the measurement error of a polarization camera when used

uncalibrated. The relative error *Err* is based on linear polarized light with DOP=1. The absolute measurement error $\left\|\vec{I}_N - \vec{I}_{N,ideal}\right\|_2$ for partially polarized or unpolarized light is smaller, due to the smaller Euclidean norm of the corresponding Stokes vector (compare Eq. (3.3))

$$\left\|\vec{S}\right\|_2 = \sqrt{S_0^2 + S_1^2 + S_2^2 + S_3^2} = \sqrt{S_0^2 + (DOP \cdot S_0)^2} \leq \sqrt{2 \cdot S_0^2} = \left\|\vec{S}_{DOP=1}\right\|_2 . \tag{3.16}$$

In conclusion, the measurement error of a polarization camera is maximum when measuring completely linear polarized light defined with DOP=1 and $S_0 = \sqrt{S_1^2 + S_2^2}$. As mentioned in section 3.1, a polarization camera is not able to measure circular polarized light and thus $S_3 = 0$ is assumed here.

3.2.3. Image Analysis

For the analysis in section 3.3.3, a region of interest of 600 x 400 pixels in the center of the sensor was selected. The same pixels were investigated in each measurement. This gives 300 x 200 analyzed super-pixels and hence 60,000 solutions of $\underline{A}$ for Eq. (3.12). We limited the amount of analyzed pixels for two reasons: first, due to the large number of required optimization routines and the consequent computational cost which would result if all 1224 x 1024 super-pixels are considered for every lens assessment. Secondly due to potential distortions related to geometrical optics (Hecht, 1998a; Theuwissen, 2011). The chief ray angle, the angle between the principle ray and the optical axis, is a function of the distance between exit pupil (relevant aperture seen from the image plane) and sensor and the pixel position on the sensor. If the distance between exit pupil and sensor is small, the chief ray angle for the pixels in the periphery of the sensor

might cause the rays to be not appropriately focused onto the corresponding photodiodes. This can cause pixel vignetting and cross-talk. Pixels in the center of the sensor are illuminated by principal rays that are largely parallel to the optical axis and hence the microlenses are able to focus the light correctly to the photodiodes. By choosing the region in the center of the sensor we try to avoid corruption from large chief ray angles.

Light from the exit pupil entering a microlens is shaped like a cone, with the principle ray being in the center. The half-angle θ of the cone is the angle at which the marginal ray enters the microlens. This angle can be described by the numerical aperture. Increasing the f-number decreases this angle, as the rays that remain able to enter the microlens become increasingly parallel to each other. Decreasing the f-number by opening the aperture enables more light to reach the microlens by widening the light cone. This implies that the additional rays enter the microlens at an increased angle. Very small f-numbers lead to rays with large angles of incidence that may not be correctly focused on to the photodiode. Moreover, large angles of incidence reduce the polarization efficiency of the PFA due to the dependence of polarizers on the angle of incidence (Chipman et al., 2018a).

In section 3.3.2 the individual super-pixels are studied and we evaluate the uniformity of the polarization measurement across the sensor. Therefore, potential corruption from large chief ray angles and from marginal rays with large angles of incidence θ is avoided as far as practically possible. We conducted measurements with the Nikon Micro-Nikkor 105mm 1:2.8 lens and set the f-number to 22. This gives marginal rays with a small incidence angle of about $\theta \approx \sin^{-1}[1/(2 \cdot 22)] \approx 1.3°$. The distance between exit pupil and sensor is lens

type dependent, but a lens with a large focal length usually comes with a larger exit pupil distance than a lens with a small focal length.

3.3. Results and Discussion

3.3.1. Effect of Dark Noise

Figure 3.3 shows the distribution of the dark noise pixel counts (12-bit) for an exposure time of one second. The image was acquired with a lid covering the camera to block the surrounding light. The pixels are sorted according to their position within the polarization filter array: 0°, 45°, 90°, 135°. We can see that the dark noise pixel count values (12-bit) are small with respect to the available gray levels (4096). There seems to be a slight difference between the 0°-135° pixels and the 45°-90° pixels. The 45°-90° pixels, which are on the same horizontal sensor row, perform slightly better than their counterparts. If the measured intensities can be kept significantly large ($\vec{I} \gg \vec{d}$), the overall influence of the dark noise should be negligible, as the normalized vector in Eq. (3.12) will be close to zero due to Eq. (3.11): $\vec{d}_N \to 0$. We propose that it is feasible not to model the dark noise via vector $\vec{d}$, provided that the measured intensity values are sufficiently large compared to the dark noise. In the following section 3.3.2 and 3.3.3, we will therefore neglect the impact of the dark noise and do not consider its modeling, i.e., by setting $\vec{d} = 0$.

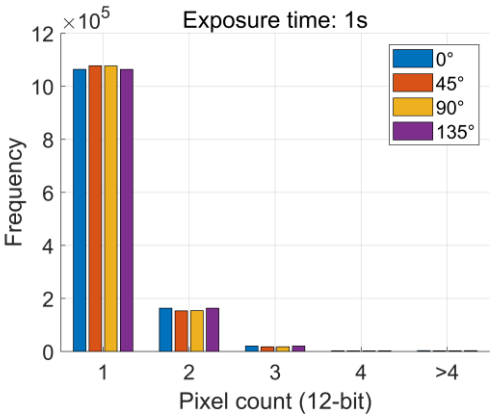

Fig. 3.3. Histogram of the pixel counts (12-bit) for an exposure time of one second.

3.3.2. Consistency of the 1224 x 1024 super-pixels

The analyzed images in this section were taken with a Nikon Micro-Nikkor 105mm 1:2.8. The settings were f/22 and exposure times of 1440ms, 1920ms and 2400ms were used to measure at three dynamic ranges. As discussed in section 3.2.3, the large focal length of 105mm is chosen to minimize distortion from large chief ray angles, and the high f-number leads to rays that are largely parallel to each other. The blue-green bandpass filter was applied, limiting the wavelengths to a range of 413-573 nm. Each super-pixel was assessed by applying Eq. (3.12) and Eq. (3.13), and the relative error *Err* was calculated using Eq. (3.15). Mean and standard deviation of the 1224 x 1024 correction factors $\Delta\phi$ in Eq. (3.13) are 0.26° and 0.09°, respectively. Figure 3.4 (a) shows measured and calibrated data for an exemplary super-pixel. Figure 3.4 (b) depicts all 1224 x 1024 super-pixel errors *Err*. The overall mean is 0.024 with a standard deviation (Std) of 0.006. Most super-pixels produce errors below 4%. The mean of the fitted transfer functions $\underline{A}$ is

$$\text{mean}(\underline{A}) = \frac{1}{2}\begin{bmatrix} 0.989 & 0.980 & -0.001 & 0 \\ 1.015 & -0.001 & 1.003 & 0 \\ 0.986 & -0.980 & -0.002 & 0 \\ 1.011 & 0 & -1.001 & 0 \end{bmatrix}, \tag{3.17}$$

with a standard deviation of:

$$\text{Std}(\underline{A}) = \begin{bmatrix} 0.003 & 0.003 & 0.002 & 0 \\ 0.003 & 0.002 & 0.003 & 0 \\ 0.003 & 0.003 & 0.002 & 0 \\ 0.003 & 0.002 & 0.003 & 0 \end{bmatrix}. \tag{3.18}$$

Figure 3.4 (c) shows the relative error *Err* for all analyzed 1224 x 1024 super-pixels. No influence of the sensor position can be identified. The “stripes” in the image are thought to be caused by the column-parallel readout of the CMOS sensor. We conclude that super-pixel polarization measurements are generally consistent across the sensor. Due to the small standard deviations in Eq. (3.18) (one order of magnitude smaller) we also conclude that all super-pixels perform similarly, and hence the mean of the transfer matrix $\underline{A}$ is a valid estimate for all super-pixels.

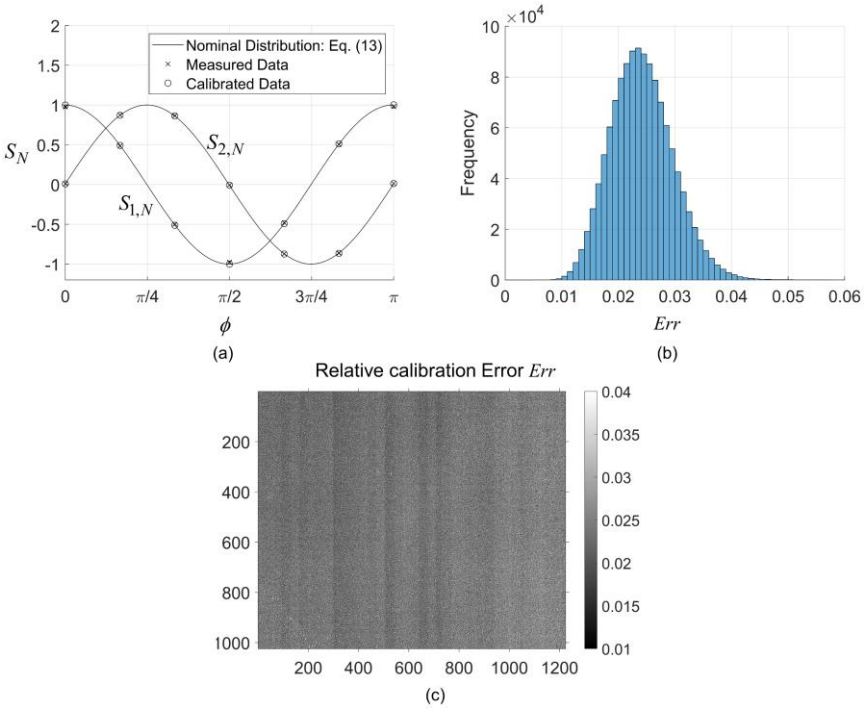

Fig. 3.4. Super-pixel assessment: (a) Measured vs. calibrated data for a single super-pixel. (b) Histogram of the relative error *Err* for all super-pixels. Overall mean: 0.024 and standard deviation: 0.006. (c) Variation of the relative error *Err* for all 1224 x 1024 super-pixels. Lens: Nikon Micro-Nikkor 105mm 1:2.8 with f/22. Wavelength: 413-573 nm.

3.3.3. Influence of Focal Ratio and Choice of Lens

The results described in this section have been obtained by analyzing the images in the way described in section 3.2.3. For the reasons given, a region of 600 x 400 pixels in the center of the sensor was selected. No dark noise effect was taken into account. For the lenses summarized in Table 3.1, all available f-numbers up to f/22 have been tested by changing the aperture. The results obtained for the Schneider Xenon 25mm f/0.95 lens and with red light are shown in Fig. 3.5 (a).

All relative errors *Err* of the 300 x 200 super-pixels are plotted as a function of the f-number. For f/0.95, the relative errors are between 9.6-12.3% and for f/11 between 2-5% (except for two outliers). Differences within the super-pixels are significantly smaller compared to the variations caused by changing the aperture. Mean values of the transfer functions $\underline{A}$ for the f/0.95 configuration are

$$\text{mean}(\underline{A}) = \frac{1}{2}\begin{bmatrix} 1.038 & 0.943 & 0.001 & 0 \\ 0.998 & -0.029 & 0.935 & 0 \\ 0.939 & -0.878 & -0.001 & 0 \\ 1.025 & -0.037 & -0.935 & 0 \end{bmatrix}, \tag{3.19}$$

with standard deviations of

$$std(\underline{A}) = \begin{bmatrix} 0.003 & 0.002 & 0.001 & 0 \\ 0.003 & 0.001 & 0.002 & 0 \\ 0.003 & 0.002 & 0.002 & 0 \\ 0.003 & 0.002 & 0.002 & 0 \end{bmatrix}. \tag{3.20}$$

The standard deviations in Eq. (3.20) are small, indicating similar performance of the superpixels across the sensor area and supporting the conclusion of section 3.3.2. Looking at Fig. 3.5 (b) we can see that the measurements at position 2 ($\phi = \pi/2$, polarization parallel to I_{90}) are less accurate compared to those at position 1 ($\phi = 0$, polarization parallel to I_0). It seems, that the values for S_{1_N} are slightly too high at position 2, indicating that the intensity measurements of the I_0 pixels are either too high or that the I_{90} measurements are too low. The results for S_{2_N} do not show this mismatch, indicating that the I_{45} and I_{135} pixels perform similarly. However, mismatching measurements for position 1 and 2 were observed at low f-numbers and not at higher f-numbers. Besides

comparing Fig. 3.5 (b) with Fig. 3.4 (a), measurement positions 1 and 2 can also be studied by means of entries $A_{11}, A_{12}, A_{31}, A_{32}$ in Eqs. (3.19) and (3.17).

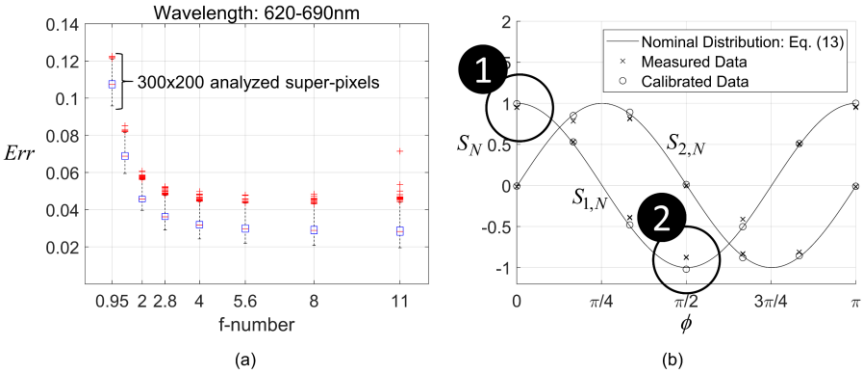

Fig. 3.5. Measurement results for the Schneider Xenon 25mm f/0.95 lens. (a) Box plots of the relative error *Err* for the 300 x 200 analyzed super-pixels plotted as function of the f-number. (b) Measured vs. calibrated data for a single super-pixel with *Err*=10.8% taken with f/0.95. Measurements at position 1 ($\phi = 0$) are more accurate than at position 2 ($\phi = \pi/2$).

The results for all lenses are shown in Fig. 3.6. The depicted values are the mean values for the calculated relative errors *Err* of the 300 x 200 analyzed super-pixels for each test case. We distinguish between blue-green light in Fig. 3.6 (a), and red light in Fig. 3.6 (b). Selected full transfer functions $\underline{A}$ for some of the results can be found in the appendix in Table 3.3-3.5. The overall performance of the blue-green light measurements is better. This is assumed to be due to a higher omnidirectional extinction ratio of the IMX250MZR sensor for wavelengths in the blue-green range compared to the longer wavelengths of the red light. Sony states an extinction ratio of 330 for a wavelength of 500nm compared to a ratio of 130 for a wavelength of 650nm (Sony Semiconductor Solutions Corporation, 2022). The results for *Err* are very close for nearly all investigated lenses,

indicating good measurement repeatability as well as a lack of focal length dependency. The focal length could however have an influence on the pixels in the periphery of the sensor due to cross-talk resulting from large chief ray angles. Besides, the distance to the objective and hence the focus does not seem to influence the results, as both are varied from lens to lens. Although these parameters have not been examined individually, the results obtained do not indicate any potential dependency. The only results that do not match the others are those of the measurements conducted with red light and the Sill TZM 1260/0.31. It being the only telecentric lens investigated, we assume the particular telecentric design to be responsible. However, to clearly identify the cause of the deviation and to exclude any potential measurement errors, further investigation would be required.

The influence of the focal ratio on the performance is apparent in Fig. 3.6 (a) and (b). In case of the blue-green light, focal ratios below 2.8 perform significantly worse. For ratios 2.8 and above, no differences between the lenses can be observed, and the results do not improve with increasing focal ratio. The same trend can be seen for the red wavelengths, but an increase of the focal ratio up to values of 8 seems to constantly improve performance. Focal ratios above 2.8 for blue-green light and above 8 for red light seem to have converged to lower limits for *Err* of approximately 2.4% and 2.7%, respectively. We suppose these limits are more likely to be linked to the performance of the sensor than to the choice of lens. Similar to the consideration referred to in section 3.2.3, we explain the inferior accuracy at low f-numbers with ray optics. Estimating the incident angles θ of the marginal rays with $\sin\theta = 1/(2\text{xf-number})$ gives an angle of about 32° for f/0.95. For these large angles of incidence the polarization efficiency of the PFA is reduced (Chipman et al., 2018a). Moreover, f-numbers this low might not focus the rays correctly. For the sufficiently large f-numbers stated this effect

seems to disappear and any further increase does not bring any noticeable improvements, as the transfer functions $\underline{A}$ (and consequently the calibration functions Eq. (3.2)) for high focal ratios are similar (e.g. Table 3.3: f/8-f/16 and Table 3.4: f/2.8-f/11 in the appendix). We also learn that the choice of lens does not seem to have an influence on the transfer function, as our tested lenses give similar results (see for example Table 3.5 in the appendix). The transfer function does however depend on the wavelength (as seen for instance by comparing Table 3.3: f/8 with Table 3.5). Summarizing, focal ratio and wavelength affect polarization measurements and researchers should consider these parameters, whereas, since we could not determine any significant differences between the tested lenses, their choice of lens is not otherwise constrained. It is important to note however, that polarization measurement accuracy in the periphery of the sensor might deteriorate due to increased chief ray angles. This is particularly important for small focal lengths.

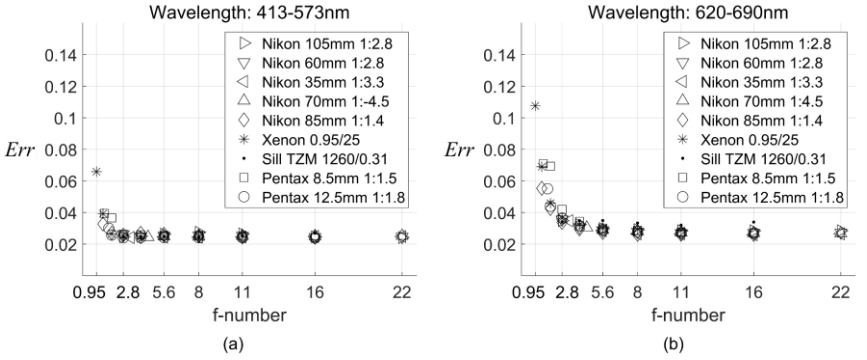

Fig. 3.6. Relative error *Err* for the tested lenses and focal ratios: (a) blue-green light and (b) red light.

3.3.4. LCD Monitor Test Case

A LCD monitor emitting green light was analyzed. The intensities were calibrated with Eq. (3.2) using the corresponding transfer matrices for f/0.95 and f/8 (see Table 3.4, appendix) and the Stokes parameters calculated with Eq. (3.1). We measured the angle of linear polarization (AOLP) using:

$$\mathrm{AOLP} = \frac{1}{2}\tan^{-1}\frac{S_2}{S_1} \tag{3.21}$$

and the degree of linear polarization (DOLP) applying Eq. (3.3) with $S_3 = 0$. Eight measurements were conducted and all 1224 x 1024 pixels evaluated. Table 3.2 summarizes the results. We rotated the camera to change the AOLP. The images $I_0, I_{45}, I_{90}, I_{135}$ showed a striped pattern due to the unused red and blue LCD pixels. We applied Gaussian filtering to unify the images. A LCD monitor emits light with DOLP=100%. A DOLP above 100% is physically not possible but calibrated results happen to be above this value. Looking at Table 3.2 it is striking that the measurements for an AOLP close to 0° seem to be more accurate with f/0.95 than with f/8. It is however important to note that these are only exemplary measurements and no general conclusions should be drawn from them. The uncalibrated measurements for f/0.95 are more accurate in the 0° direction than they are in the 90° direction, which is consistent with Fig. 3.5 (b) and the transfer function in Eq. (3.19). The maximum measurement errors in Table 3.2 are around 8% for f/0.95 and 3% for f/8. This is in line with the results for the calculated relative *Err* plotted in Fig. 3.6 (a).

Table 3.2. Measurement results for LCD monitor. Uncalibrated (raw) and calibrated data. Standard deviations for AOLPs were <0.5° and <0.7% for the DOLPs. Lens: Schneider Xenon 25mm f/0.95.

	mean AOLP		mean DOLP	
f-number	raw	calibrated	Raw	calibrated
0.95	-0.7°	-0.7°	98.5%	98.6%
	42.5°	43.8°	98.3%	99.3%
	89.4°	89.4°	92.4%	101.3%
	134.1°	134.7	98.4%	99.5%
8	-0.7°	-0.7°	97.4%	99.4%
	44.0°	44.1°	99.9%	99.4%
	89.3°	89.3°	97.4%	99.7%
	134.4°	134.4°	99.7%	99.4%

3.4. Conclusion

In this paper, the Sony polarization image sensor IMX250MZR was calibrated using different lenses and focal ratios and two wavelengths: blue-green (413-573nm) and red (620-690nm). The sensor has 2448 x 2048 pixels covered by a polarization filter array. Four neighboring single-pixels form a super-pixel, resulting in 1224 x 1024 available super-pixels. We have defined a parameter that quantifies the amount of calibration necessary and thus serves as an indicator for the polarization measurement quality. With the help of this parameter we show that polarization measurements are consistent for all super-pixels within quantifiable variances. Therefore, not every super-pixel has to be calibrated individually. We also deduce that dark noise does not significantly corrupt the results and hence does not have to be modeled, provided that the measured

intensity values are sufficiently large. Various lenses and focal ratios up to 22 were tested. It was demonstrated that polarization measurements with blue-green light are generally more precise than with red, as the sensor's extinction ratio is about three times higher for these shorter wavelengths (Sony Semiconductor Solutions Corporation, 2022). Moreover, the choice of lens does not influence the polarization measurement quality, but the results indicate that focal ratios below 2.8 disrupt the measurements. We finally determine that measurements conducted with f-numbers of above 2.8 (blue-green light) and 8 (red light) are no longer affected by the focal ratio and the upper error in these cases is estimated to be below 4%. This is however only valid for the central pixels. For a short focal length, a potential measurement deterioration towards the peripheral pixels due to an increasing influence of the chief ray angle cannot be excluded.

3.5. Appendix

Evaluated transfer functions $\underline{A}$ for some of the measurements conducted in section 3.3.3. They are given in Table 3.3-3.5 in the form of:

$$\underline{A} = \frac{1}{2}\begin{bmatrix} a_{11} & a_{12} & a_{13} & 0 \\ a_{21} & a_{22} & a_{23} & 0 \\ a_{31} & a_{32} & a_{33} & 0 \\ a_{41} & a_{42} & a_{43} & 0 \end{bmatrix}. \tag{3.22}$$

Table 3.3. Matrix entries for the transfer functions calculated with a Nikon Nikkor 85mm 1:1.4 lens. Wavelength: 620-690nm.

	a_{11}	a_{21}	a_{31}	a_{41}	a_{12}	a_{22}
f/1.4	1.017	1.003	0.961	1.020	0.957	-0.019
f/2	1.016	1.001	0.962	1.021	0.957	-0.018
f/2.8	0.992	1.004	0.990	1.014	0.958	0.000

f/4	0.990	1.004	0.993	1.012	0.963	0.002
f/5.6	0.991	1.008	0.993	1.008	0.968	0.001
f/8	0.993	1.008	0.991	1.009	0.971	0.000
f/11	0.993	1.011	0.990	1.006	0.973	0.000
f/16	0.994	1.009	0.989	1.008	0.974	-0.001
	a_{32}	a_{42}	a_{13}	a_{23}	a_{33}	a_{43}
f/1.4	-0.917	-0.022	-0.001	0.961	0.000	-0.961
f/2	-0.919	-0.020	-0.002	0.962	0.002	-0.962
f/2.8	-0.958	0.000	-0.002	0.977	0.002	-0.977
f/4	-0.969	0.003	-0.002	0.983	0.002	-0.983
f/5.6	-0.972	0.003	-0.001	0.987	0.001	-0.987
f/8	-0.972	0.001	-0.001	0.989	0.001	-0.989
f/11	-0.972	0.000	0.000	0.991	0.001	-0.990
f/16	-0.972	-0.001	0.000	0.992	0.000	-0.991

Table 3.4. Matrix entries for the transfer functions calculated with a Schneider Xenon 25mm f/0.95 lens. Wavelength: 413-573nm.

	a_{11}	a_{21}	a_{31}	a_{41}	a_{12}	a_{22}
f/1.4	1.028	1.015	0.941	1.017	0.985	-0.028
f/2	1.006	1.016	0.966	1.012	0.981	-0.012
f/2.8	0.991	1.013	0.984	1.013	0.976	-0.001
f/4	0.988	1.016	0.986	1.010	0.976	0.001
f/5.6	0.989	1.014	0.985	1.012	0.978	0.000
f/8	0.988	1.017	0.986	1.009	0.979	0.000
f/11	0.989	1.014	0.985	1.012	0.979	0.000
f/16	0.988	1.017	0.986	1.009	0.978	0.000

	a_{32}	a_{42}	a_{13}	a_{23}	a_{33}	a_{43}
f/1.4	-0.925	-0.033	0.002	0.989	-0.004	-0.987
f/2	-0.954	-0.015	0.001	0.999	-0.003	-0.997
f/2.8	-0.974	-0.002	-0.001	1.003	-0.001	-1.001
f/4	-0.977	0.000	0.000	1.005	-0.002	-1.003
f/5.6	-0.978	0.000	0.000	1.006	-0.002	-1.003
f/8	-0.978	-0.001	0.001	1.006	-0.003	-1.004
f/11	-0.978	-0.001	0.000	1.005	-0.002	-1.003
f/16	-0.978	-0.001	0.000	1.005	-0.003	-1.003

Table 3.5. Comparison of transfer functions calculated with different lenses. Focal ratio: f/8. Wavelength: 413-573nm.

	a_{11}	a_{21}	a_{31}	a_{41}	a_{12}	a_{22}
Nikon Micro-Nikkor 105mm 1:2.8						
f/8	0.988	1.017	0.986	1.009	0.980	-0.001
Nikon Micro-Nikkor 60mm 1:2.8						
f/8	0.988	1.016	0.986	1.010	0.981	0.000
Nikon Nikkor 35-70mm 1:3.3-4.5 with 35mm						
f/8	0.988	1.017	0.986	1.009	0.980	-0.001
Nikon Nikkor 35-70mm 1:3.3-4.5 with 70mm						
f/8	0.988	1.014	0.986	1.012	0.980	0.000
Nikon Nikkor 85mm 1:1.4						
f/8	0.989	1.014	0.985	1.012	0.981	0.000
Schneider Xenon 0.9/25						
f/8	0.989	1.014	0.985	1.012	0.979	0.000
Sill TZM 1260/0.31						
f/8	0.989	1.014	0.986	1.012	0.979	0.000

Pentax 8.5mm 1:1.5						
f/8	0.989	1.014	0.985	1.012	0.98	0.000
Pentax 12.5mm 1:1.8						
f/8	0.988	1.016	0.986	1.010	0.981	0.000

	a_{32}	a_{42}	a_{13}	a_{23}	a_{33}	a_{43}
Nikon Micro-Nikkor 105mm 1:2.8						
f/8	-0.979	0.000	0.000	1.002	-0.002	-1.000
Nikon Micro-Nikkor 60mm 1:2.8						
f/8	-0.980	-0.001	0.000	1.007	-0.002	-1.005
Nikon Nikkor 35-70mm 1:3.3-4.5 with 35mm						
f/8	-0.979	0	0.000	1.008	-0.002	-1.006
Nikon Nikkor 35-70mm 1:3.3-4.5 with 70mm						
f/8	-0.979	-0.001	0.000	1.007	-0.002	-1.005
Nikon Nikkor 85mm 1:1.4						
f/8	-0.980	-0.001	0.000	1.007	-0.002	-1.005
Schneider Xenon 0.9/25						
f/8	-0.978	-0.001	0.000	1.005	-0.002	-1.003
Sill TZM 1260/0.31						
f/8	-0.979	0	-0.001	1.003	-0.001	-1.001
Pentax 8.5mm 1:1.5						
f/8	-0.979	-0.001	0.000	1.008	-0.002	-1.006
Pentax 12.5mm 1:1.8						
f/8	-0.980	-0.001	0.000	1.007	-0.002	-1.005

4. Two-dimensional birefringence measurement technique using a polarization camera

The content of this chapter has been published in (Lane et al., 2021a):

Lane, C., Rode, D., & Rösgen, T. (2021a). Two-dimensional birefringence measurement technique using a polarization camera. *Applied Optics*, *60*(27), 8435. https://doi.org/10.1364/AO.433066

Author contribution statements:

Connor Lane developed the theory, designed the experimental setup, analysed the data, and wrote the manuscript. David Rode helped to carry out the experiments and sort out the references. Thomas Rösgen developed the camera software and directed the project. All authors discussed the results and helped formulate the manuscript.

Note:

The following refers to the author version. Please refer to the original paper for the typeset version. The text is quoted verbatim; however, the citation style and the numbering of the figures and equations have been aligned to this document and are therefore changed. The figures are reprinted with permission (see copyright transfer and licensing information (Optica Publishing Group, 2022)).

Disclosures:

The authors declare no conflicts of interest.

Abstract

A two-dimensional birefringence measurement method is described. In this procedure, we send light through a rotatable linear polarizer and subsequently through a transparent and birefringent specimen. A polarization camera measures the state of linear polarization from which the relative position of the refractive index axes and the relative phase difference are determined. The measurement range of the phase difference is up to π radians, which corresponds to an optical retardation of half the wavelength of the light. The imaging system can measure a large sample area within one measurement cycle. Measurement performance is demonstrated with a quarter-wave plate and an exemplary test case is shown.

4.1. Introduction

The ability to measure birefringence distributions is important for various applications. These include the analysis of inner stress by means of photoelasticity in optically anisotropic solids composed of transparent materials such as crystals, polymers or glasses. Besides these established applications, other potential use cases for birefringence imaging techniques are being explored. Examples include biomedical research (Boer et al., 1997; de Boer et al., 1998; Walther et al., 2019; Yasuno et al., 2002), material inspection systems (Ganapati et al., 2010), microfluidics (Yang et al., 2020) and polarization-sensitive optical diffraction tomography (Saba et al., 2021). In many applications, a two-dimensional birefringence measurement system is desirable. The system requirements are to identify the relative retardation and the position of the refractive index axes. Several researchers have proposed and discussed such measurement systems. Reviews on relevant techniques used in photoelasticity can be found in the literature (Ajovalasit et al., 1998, 2015; Ramesh, 2000; Ramesh et al., 2011; Ramesh & Ramakrishnan, 2016; Ramesh & Sasikumar, 2020; Solaguren-Beascoa

Fernández, 2011). Their utility can also be evaluated in the broader context of general two-dimensional birefringence. A common method is the phase shifting technique (Onuma & Otani, 2014; Otani, Shimada, & YoSHIZAWA, 1994; Otani, Shimada, Yoshizawa, et al., 1994; M. I. Shribak et al., 1999), applied in precise and fast 2-D analysis systems. Using circularly polarized light and a polarization image sensor, it allows determination of the position of the fast axis and phase differences of up to $\pi/2$ radians (Onuma & Otani, 2014). Stokes vector and Mueller matrix polarimetry have been used to characterize materials and measure the state of polarization (Azzam, 2016; Hall et al., 2013; Pezzaniti & Chipman, 1995). The literature offers several other studies dealing with photoelasticity, birefringence and polarimetry, e.g. (Glazer et al., 1996; Mei & Oldenbourg, 1994; Nurse, 1997; Oldenbourg & Mei, 1995; Patterson et al., 1997; M. I. Shribak & Oldenbourg, 2002; M. Shribak & Oldenbourg, 2003; Zhu et al., 1999). Approaches differ in experimental design and evaluation techniques. Most use rotating optical polarization components or variable retarders and determine birefringence by analyzing the resulting changes in light intensity. Technological advances in imaging and measurement systems continue to facilitate new approaches. The recent introduction of polarization sensitive cameras represents such an advancement and they are increasingly used in research studies, e.g. (Iwata et al., 2019; Liu et al., 2020; Oba & Inoue, 2016). Currently, most techniques are complex, require expensive hardware or are only able to measure phase differences of up to $\pi/2$, corresponding to a quarter of the applied wavelength. This range may be expanded by considering other information, for example conducting the measurements with two or more wavelengths (Ajovalasit et al., 2015), but the periodic nature of the relative retardation, a fundamental challenge to all methods (Patterson et al., 1997), may require the maximum measurement range of the phase difference in particular cases. We introduce a

measurement system that consists of a single rotatable linear polarizer and a polarization camera. The measurement range of the phase difference is up to π radians (half of the applied wavelength) and the relative position of the refractive index axes can be determined. However, fast and slow axis cannot be distinguished. The overall idea and concept are based on a previous study (Lane et al., 2021b), in which we analyzed birefringence of a fluid in a Taylor-Couette flow. There, the circular geometry of the experiment naturally lead to a rotation of the sample and thus polarizer and polarization camera could remain at fixed positions. The approach described in the present study could be more broadly appliable.

4.2. Theory

The basic optical measurement setup is shown in Fig. 4.1. Light from a source passes a linear polarizer $P(\phi)$. A global coordinate system X-Y is given as a reference. The polarizer is rotated by an angle ϕ. A transparent sample $X_{\Delta,\theta}$ with an unknown 2-D distribution of the birefringent properties Δ and θ is to be examined, where Δ is the relative phase difference and θ the angle of the refractive index axis n_1. We define this axis to be the fast ($n_1 < n_2$) vibration direction of the light. This definition sets θ to the range $[0, \pi]$. If the optical properties are assumed to be constant throughout the thickness of the sample, the phase shift Δ is given by

$$\Delta = 2\pi \cdot \delta n \cdot \frac{L}{\lambda}. \tag{4.1}$$

Here, λ is the wavelength of the light, L the thickness of the sample and $\delta n = |n_2 - n_1|$ the difference of the refractive indexes. $\delta n \cdot L$ is referred to as optical retardation.

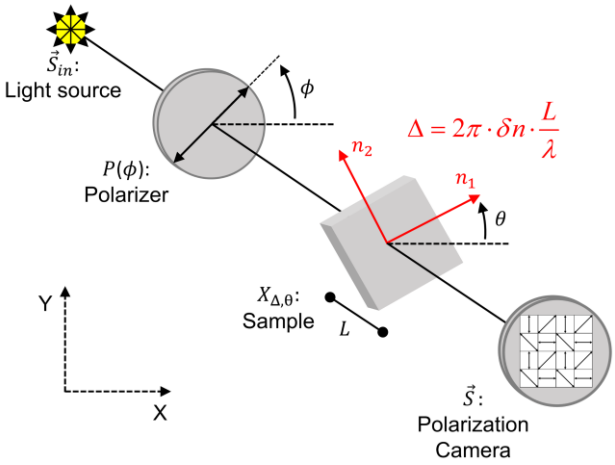

Fig. 4.1. Principle Optical setup.

A polarization camera detects the light which passes through the sample. The camera used in this study is based on a division-of-focal-plane polarization image sensor (Sony IMX 250 MZR (Sony Semiconductor Solutions Corporation, 2022)). The basic structure of such a polarization image sensor is shown in Fig. 4.2.

Small polarizers are aligned in four defined directions, forming a polarizer filter array. The direction depends on the position of the pixel. Arrays of these polarized pixel combinations enable the camera to simultaneously measure the intensities passing through the specified directions, which we define as $I_0, I_{45}, I_{90}, I_{135}$. Four neighboring pixels with polarizers oriented at 0°, 45°, 90° and 135° form a

so-called super-pixel as depicted in Fig. 4.2. In our setting, direction I_0 is in line with the X-axis. A polarization camera introduces errors such as field-of-view errors resulting from the spatial arrangement of the polarizer filter array (Ratliff et al., 2009) and errors introduced by optical imperfections of the polarizer filter array (Gimenez et al., 2020; Powell & Gruev, 2013). Alternatively, instead of the polarization camera, a second rotatable linear polarizer mounted in front of a monochrome camera could be used. The second polarizer would then be rotated to the corresponding positions: 0°, 45°, 90°, 135°. An advantage of such a setup would be the mitigation of the errors introduced by a polarization camera and to have the opportunity to apply polarizers of the highest possible quality. The advantage of the polarization camera, however, is the concurrent measurement of the four directions of polarization.

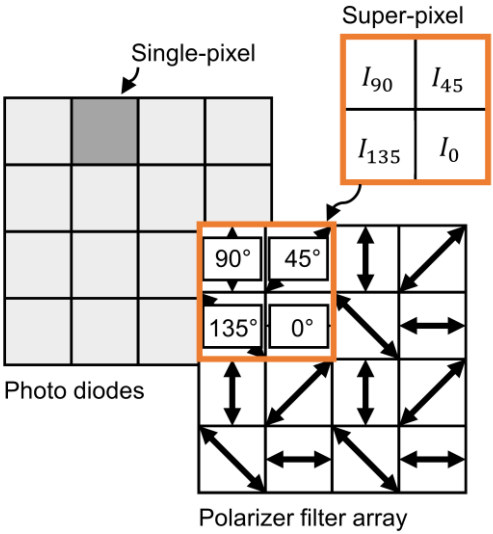

Fig. 4.2. Schematic structure of a division-of-focal-plane polarization image sensor.

With the definition of the Stokes parameters being

$$\vec{S} = \begin{bmatrix} S_0 \\ S_1 \\ S_2 \\ S_3 \end{bmatrix} = \begin{bmatrix} I_0 + I_{90} \\ I_0 - I_{90} \\ I_{45} - I_{135} \\ I_R - I_L \end{bmatrix}, \tag{4.2}$$

each super-pixel of the polarization image sensor can measure the first three parameters. Parameter S_3 requires information about the rotation direction of the light that cannot be directly measured with the polarization camera.

Stokes parameters and Mueller matrices are used to describe the state of polarization and its changes, respectively. The following vectors and matrixes refer to the fixed X-Y coordinate system and can be found in the literature, for example in (Chipman, 1994; Fuller, 1995b). We define $\vec{S}_{in}$ as the corresponding Stokes vector of an unpolarized light source and $P(\phi)$ as the Mueller matrix of a linear polarizer oriented at ϕ,

$$P(\phi) = \frac{1}{2}\begin{bmatrix} 1 & \cos 2\phi & \sin 2\phi & 0 \\ \cos 2\phi & \cos^2 2\phi & \sin 2\phi \cos 2\phi & 0 \\ \sin 2\phi & \sin 2\phi \cos 2\phi & \sin^2 2\phi & 0 \\ 0 & 0 & 0 & 0 \end{bmatrix}. \tag{4.3}$$

A linear retarder $X_{\Delta,\theta}$ inducing a phase shift Δ with an orientation angle of the fast axis θ can be expressed as

$$X_{\Delta,\theta} = \begin{bmatrix} 1 & 0 & 0 & 0 \\ 0 & \cos^2 2\theta + \sin^2 2\theta \cos\Delta & \cos 2\theta \sin 2\theta (1-\cos\Delta) & -\sin 2\theta \sin\Delta \\ 0 & \cos 2\theta \sin 2\theta (1-\cos\Delta) & \sin^2 2\theta + \cos^2 2\theta \cos\Delta & \cos 2\theta \sin\Delta \\ 0 & \sin 2\theta \sin\Delta & -\cos 2\theta \sin\Delta & \cos\Delta \end{bmatrix}. \tag{4.4}$$

The relation between incident and outgoing Stokes vector is then given by

$$\vec{S} = X_{\Delta,\theta} \cdot P(\phi) \cdot \vec{S}_{in}. \tag{4.5}$$

Using the normalized representation of the Stokes parameters $\vec{S}_N = 1/S_0 \cdot \vec{S}$ (note the difference to a regular vector normalization), the expressions for S_{1_N} and S_{2_N} that are independent of the light source intensity are derived,

$$\begin{aligned} S_{1_N}(\Delta,\theta,\phi) &= \tfrac{1}{2}(\cos 2\phi + \cos 2\phi \cos\Delta + \cos[2\phi - 4\theta] \times (1-\cos\Delta)), \\ S_{2_N}(\Delta,\theta,\phi) &= \tfrac{1}{2}(\sin 2\phi + \sin 2\phi \cos\Delta - \sin[2\phi - 4\theta] \times (1-\cos\Delta)). \end{aligned} \tag{4.6}$$

We can see that

$$S_{2_N}(\Delta,\theta+\frac{\pi}{4},\phi+\frac{\pi}{4}) = S_{1_N}(\Delta,\theta,\phi). \tag{4.7}$$

This is in line with the definition of S_{1_N} and S_{2_N}, as their corresponding intensities (I_0, I_{90} and I_{45}, I_{135}) are rotated by $\pi/4$. Due to the range for the degree of linear polarization (DOLP),

$$\mathrm{DOLP} = \frac{\sqrt{S_1^2 + S_2^2}}{S_0}, \tag{4.8}$$

S_{1_N} and S_{2_N} must fulfil

$$S_{1_N}^2 + S_{2_N}^2 \leq 1. \tag{4.9}$$

The position of the linear polarizer is described by the known angular coordinate ϕ. This reduces Eq. (4.6) to two equations with two unknowns (Δ, θ) and two measurable parameters (S_{1_N}, S_{2_N}). For a specific position of the linear polarizer, we can therefore derive explicit relations for Δ, θ, here done for the case $\phi = 0$,

$$\begin{aligned} \Delta &= \cos^{-1}[1 - \frac{S_{2_N}^2 + (1 - S_{1_N})^2}{1 - S_{1_N}}], \\ \theta &= \frac{1}{2}\tan^{-1}\frac{1 - S_{1_N}}{S_{2_N}}. \end{aligned} \tag{4.10}$$

Figures 4.3 (a), (b) show Eq. (4.6) for the case $\phi = 0$ and Fig. 4.3 (e), (f) the corresponding inverse relationships from Eqs. (4.10). From Eqs. (4.6) and (4.10) and Fig. 4.3 it is clear that the Stokes parameters S_{1_N} and S_{2_N} are periodic with period $\pi/2$ in θ (the range $[-\pi/4, 0]$ corresponding to $[\pi/4, \pi/2]$). Fig. 4.3 (f) shows the orientation angle for all possible combinations of S_{1_N} and S_{2_N} (with $S_{1_N}^2 + S_{2_N}^2 \leq 1$). It stays in the range [0, $\pi/2$]. This means that no distinction between fast and slow vibration axis can be made, as otherwise the period of θ would have to be π and the range of values [0, π]. The periodicity of Δ is 2π. When the retardation $\delta n \cdot L$ is a multiple of λ, the phase difference Δ is a multiple of 2π and the state of polarization will be linear again, orientated at ϕ equal to the state and orientation of the linear polarizer $P(\phi)$. Both relations in

Eq. (4.10) are not defined for $S_{1_N} = 1$ and $S_{2_N} = 0$. Such a Stokes vector can be anywhere on an isoclinic or isochromatic (blue dashed lines and black solid lines in Fig. 4.3 (a), (b)), with corresponding values for Δ and θ. Looking at Fig. 4.3 (e) we can see, that $\Delta = \pi$ applies for a circle defined by $S_{1_N}^2 + S_{2_N}^2 = 1$. In this case the light beam is fully linear polarized ($DOLP = 1$). Fully linear polarization is only possible if retardation $\delta n \cdot L$ is an odd multiple of $\lambda / 2$ (besides the discussed and trivial case of $S_{1_N} = 1$ and $S_{2_N} = 0$). This means that the relative phase between the two oscillating and perpendicular electromagnetic vibrations has shifted by an odd multiple of π, the location of maximum (relative) phase difference. Relations (4.10) also give insight to the direct measurement ranges of Δ and θ. Unless further information is supplied, it remains undefined how many periods of retardation have occurred. If the only available information is based on S_{1_N} and S_{2_N}, the period number, also known as order, remains unclear. Moreover, retardation could also be in the "second half" of the corresponding period number, meaning that retardation could be between either [0, $\lambda / 2$] or [$\lambda / 2$, λ], which corresponds to relative phase differences of [0, π] and [π , 2π]. Summarizing, the orientation of the refractive index axes can only be measured in the range [0, $\pi/2$], and it is not possible to distinguish between fast and slow axis. Phase differences Δ are measurable in the range [0, π]. However, for any measured (relative) phase difference Δ, the following (absolute) phase differences Δ^A are possible:

$$\Delta^A = N \cdot 2\pi \pm \Delta \quad \text{with} \quad N = 0,1,2,3,... \tag{4.11}$$

As the relation (4.10) is not defined for the case $S_{1_N} = 1, S_{2_N} = 0$, we suggest multiple measurements at different angles ϕ to determine the optical properties. Rotating the linear polarizer by ϕ will lead to distributions of $S_{1_N}(\phi)$ and $S_{2_N}(\phi)$. Figures 4.3 (c) and 4.3 (d) show distributions for the case $\theta = 0$. From such distributions, we will be able to clearly identify the optical parameters within the discussed ranges.

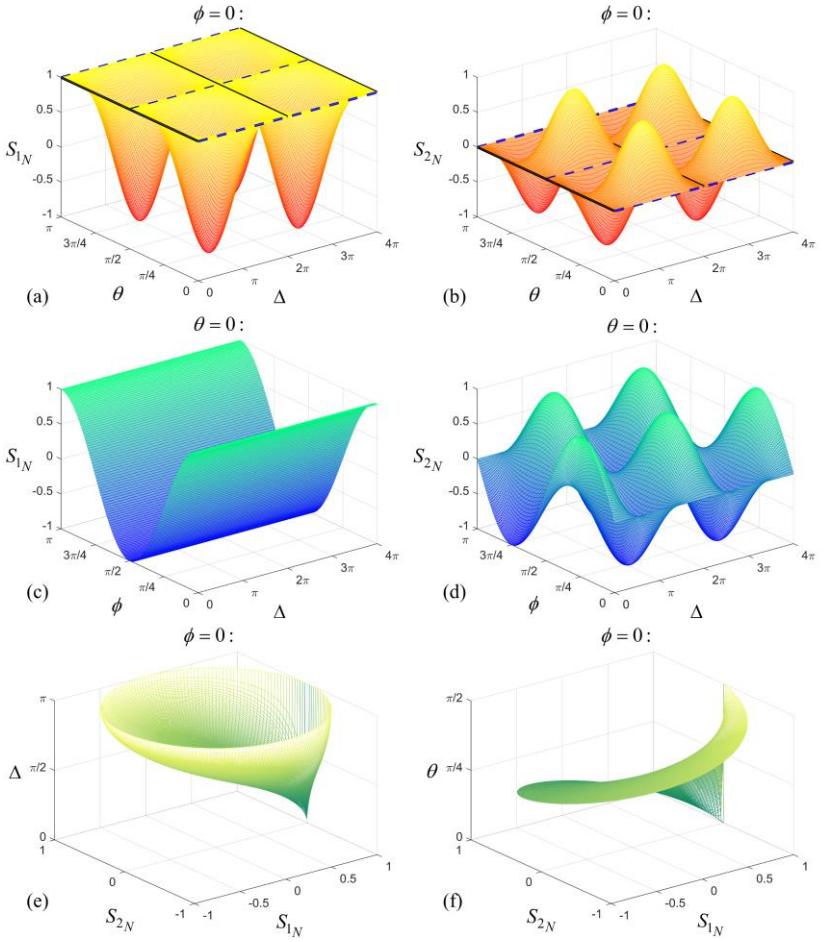

Fig. 4.3. Stokes parameters S_{1_N} and S_{2_N} in relation to the phase difference Δ and angle θ. (a) and (b): Eq. (4.6) for the case $\phi = 0$. Blue dashed lines indicate isoclinics (no change in polarization as linear polarization is in line with refractive index axes). Black solid lines indicate isochromatics (retardation being a multiple of λ). (c) and (d): Eq. (4.6) for the case $\theta = 0$. (e) and (f): Eq. (4.10), being the inverse relationships of Eq. (4.6) for the case $\phi = 0$. The phase difference Δ in

(e) is not defined for the case $S_{1_N} = 1$. The surface in (f) was created using atan2(), the 2-argument arctangent.

4.3. Material and methods

4.3.1. Applied materials

A halogen incandescent lamp was applied as light source and a white optical diffusor was placed between the lamp and the linear polarizer to illuminate the specimen as evenly as possible. The linear polarizer had an extinction ratio of 10,000:1 and was manually rotated using a continuous rotation mount (Thorlabs #RSP2/M). The test sample was an achromatic polymer quarter-wave plate (inducing a phase difference of $\pi/2$ rad) with a wavelength range of 450-600nm, retardance tolerance of 10nm and diameter 25mm (Edmund Optics Inc., article number #88-198). Placed before the specimen was a green bandpass filter (CWL 526nm, FWHM 53nm; Edmund Optics Inc #46-053). The camera was a monochrome polarization camera (Phoenix PHX050S-P from Lucid Vision Labs (LUCID Vision Labs, 2022) based on a Sony IMX250MZR CMOS (mono) sensor [34]) equipped with a Schneider Xenon 50mm/0.95 lens. The f-number was set to f/0.95. The camera resolution is 2448 x 2048 (5 MP) pixels with a pixel size of 3.45 x 3.45 micrometer. As indicated in Fig. 4.2, four neighboring single pixels, each having a different linear polarizer, form a super-pixel. This leads to a spatial resolution for Stokes parameter measurements of 1224 x 1024 (1.25 MP) super-pixels.

4.3.2. Measurement procedure

The linear polarizer is rotated by changing ϕ. Looking at relations (4.6) and Fig. 4.3 we see, that besides the periodicities in Δ and θ, the Stokes parameters S_{1_N}

and S_{2_N} are also periodic with period π in ϕ. To get full resolution along one period of ϕ, the polarizer will hence have to be rotated up to π radians.

For every polarizer position ϕ, the first three Stokes parameters are measured,

$$\begin{aligned} S_0(\phi) &= \frac{I_0(\phi) + I_{45}(\phi) + I_{90}(\phi) + I_{135}(\phi)}{2} \\ S_1(\phi) &= I_0(\phi) - I_{90}(\phi) \\ S_2(\phi) &= I_{45}(\phi) - I_{135}(\phi). \end{aligned} \tag{4.12}$$

Formally, the first Stokes parameter can be derived as $S_0 = I_0 + I_{90} = I_{45} + I_{135}$. We therefore average both measurements. The normalized form results following $\vec{S}_N = 1/S_0 \cdot \vec{S}$. Ideally, the degree of polarization (DOP) should equal one: $\mathrm{DOP} = 1$. The DOP is defined as (note the difference to the DOLP):

$$\mathrm{DOP} = \frac{\sqrt{S_1^2 + S_2^2 + S_3^2}}{S_0} \tag{4.13}$$

However, the measured Stokes vector will only be partially polarized ($\mathrm{DOP} < 1$). Noisy unpolarized light intensities arising from the environment and from imperfections of the optical components are unavoidable. This is particularly the case when a distributed light source instead of a laser is applied, as it is done in this study. Partially polarized Stokes vectors can be considered as a superposition of a fully polarized Stokes vector $\vec{S}_P$ and an unpolarized Stokes vector $\vec{S}_U$ (Chipman, 1994),

$$\vec{S} = \vec{S}_P + \vec{S}_U = \mathrm{DOP}\begin{bmatrix} S_0 \\ S_1/\mathrm{DOP} \\ S_2/\mathrm{DOP} \\ S_3/\mathrm{DOP} \end{bmatrix} + (1-\mathrm{DOP})\begin{bmatrix} S_0 \\ 0 \\ 0 \\ 0 \end{bmatrix}. \qquad (4.14)$$

The normalized representation of the fully polarized part of the Stokes vector measured at a polarizer position ϕ can be written as

$$\vec{S}_{P,N}(\phi) = \begin{bmatrix} 1 \\ S_{1_{P,N}}(\phi) \\ S_{2_{P,N}}(\phi) \\ - \end{bmatrix} = \begin{bmatrix} 1 \\ \dfrac{S_1(\phi)}{S_0(\phi)\cdot \mathrm{DOP}} \\ \dfrac{S_2(\phi)}{S_0(\phi)\cdot \mathrm{DOP}} \\ - \end{bmatrix}, \qquad (4.15)$$

where the *DOP* is unknown. As we cannot measure S_3, it is simply left out. This leads to measurable distributions of $S_{1_N}(\phi) = S_1(\phi)/S_0(\phi)$ and $S_{2_N}(\phi) = S_2(\phi)/S_0(\phi)$. Due to imperfect alignment of the polarizer camera an additional parameter $d\phi$ was introduced, that corrects for alignment errors. Together with the previous three unknowns, this gives two equations, sampled at the multiple different points ϕ, with four parameters (Δ, θ, DOP, $d\phi$),

$$S_{1_N}(\phi) = \frac{\mathrm{DOP}}{2}(\cos[2(\phi + d\phi)] + \cos[2(\phi + d\phi)]\cos\Delta + \cos[2\phi + 2d\phi - 4\theta](1-\cos\Delta)),$$
$$S_{2_N}(\phi) = \frac{\mathrm{DOP}}{2}(\sin[2(\phi + d\phi)] + \sin[2(\phi + d\phi)]\cos\Delta - \sin[2\phi + 2d\phi - 4\theta](1-\cos\Delta).$$
(4.16)

Rotating the linear polarizer $P(\phi)$ and taking images at different positions ϕ results in measured distributions of $S_{1_N}(\phi)$ and $S_{2_N}(\phi)$. Fitting Eq. (4.16) to these measurements gives the parameters $\Delta, \theta, \mathrm{DOP}, d\phi$. This can be simultaneously done throughout an area, resulting in a two-dimensional birefringence measurement.

4.3.3. Camera calibration

The camera was calibrated following the super-pixel calibration described in (Gimenez et al., 2020; Powell & Gruev, 2013). Test images for the training data were taken at three different intensity values (achieved by varying the exposure time) and at ten different polarizer positions $P(\phi)$, each having a step size of 20° between them. The training data was acquired using the same optical setup as shown in Fig. 4.1 but without a specimen $X_{\Delta,\theta}$. At first, aligning imperfections between polarizer $P(\phi)$ and polarization camera were corrected with $d\phi$. Therefore, the idealized distributions of the Stokes parameters $S_{1_N}(\phi)$ and $S_{2_N}(\phi)$ were fitted to the measurements:

$$\begin{aligned} S_{1_N}(\phi) &= \cos[2(\phi + d\phi)], \\ S_{2_N}(\phi) &= \sin[2(\phi + d\phi)]. \end{aligned} \tag{4.17}$$

These equations result when setting $\Delta = 0$ and *DOP* = 100% in Eq. (4.16). Fitting Eq. (4.17) to the measurements gives $d\phi$. The resulting distributions [Eq. (4.17)] (including $d\phi$) are then used as training data for the super-pixel calibration, which gives a calibration function as follows:

$$Cal(\vec{I}) = \underline{G} \cdot (\vec{I} - \vec{d}) \tag{4.18}$$

Here $\vec{I} = \left[I_0 \quad I_{45} \quad I_{90} \quad I_{135} \right]^T$ are the measured intensities, $\vec{d}$ is the darknoise offset and $\underline{G}$ the gain correction of the super-pixel. Each analyzed super-pixel was calibrated separately. However, variation among the super-pixels was negligible and we hence averaged the calibration function over all involved super-pixels. Figure 4.4 summarizes the calibration.

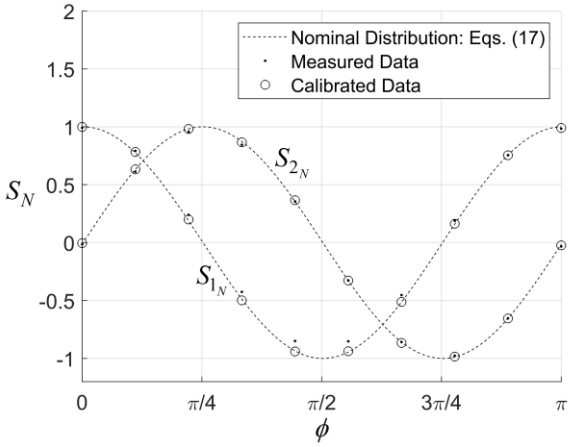

Fig. 4.4. Nominal, measured and calibrated data for an exemplary measurement point with $d\phi = -0.29°$.

4.3.4. Performance tests

In total we conducted a series of 6 tests. For every test, a region of 200 x 160 pixels (100 x 80 super-pixels) was analyzed. This gives a sufficient number of measurements (8000) without having to consider the computational effort fitting Eqs. (4.16). The position of the linear polarizer $P(\phi)$ was varied between 0° and 180°. At every position ϕ one image was taken with the polarization camera.

Starting at $\phi = 0°$ and increasing the angle by one degree for every step gave 181 evaluated polarizer positions. The intensities $I_0, I_{45}, I_{90}, I_{135}$ of the analyzed pixels were calibrated with Eq. (4.18). Following Eq. (4.12), the normalized Stokes parameters S_{1_N} and S_{2_N} were obtained for every evaluated polarizer position. This gives distributions along ϕ for every analyzed super-pixel. Fitting Eq. (4.16) to the measurements $S_{1_N}(\phi)$ and $S_{2_N}(\phi)$ leads to estimates for $\Delta, \theta, DOP, d\phi$. Repeating this for every super-pixel generates a two-dimensional distribution. Parameter $d\phi$ was fitted in section 4.3.3 for the camera calibration. However, it is fitted again for every measurement, as the results of section 4.3.3 did not always match the results we achieved when fitting parameter $d\phi$ concurrently with Eq. (4.16). One reason for this could be that the quarter-wave plate rotates the incident linear polarized light. The second reason is that we assume our manual positioning of the polarizer $P(\phi)$ to be slightly inconsistent from measurement to measurement.

4.4. Results and discussion

Figure 4.5 shows results for a test carried out with the quarter-wave plate. The results correspond to Test 2 in Table 4.1. Fig. 4.5 (a) shows an example of measured and fitted distributions of normalized Stokes parameters $S_{1_N}(\phi)$ and $S_{2_N}(\phi)$ for a super-pixel. The data was fitted with a nonlinear least-squares algorithm. Fig. 4.5 (b) shows the variation of Δ for all measured 100 x 80 super-pixels. All phase differences are in the range [1.584, 1.609]. In the following subsections, we analyze the two-dimensional measurement capability, compare the performed tests and discuss the number of polarizer positions $P(\phi)$ necessary

for satisfactory results. Finally, an exemplary test case is given to demonstrate the measurement system.

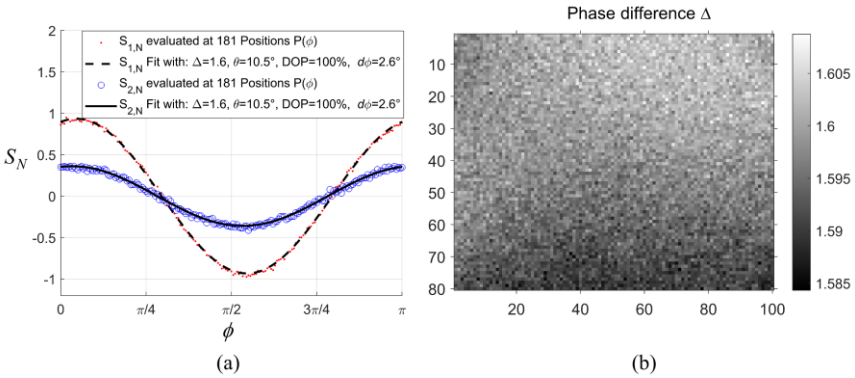

Fig. 4.5. Exemplary measurement results for a quarter-wave plate (The results correspond to Test 2 in Table 4.1): (a) Measured and fitted distributions for one super-pixel. (b) Variation of Δ for the analyzed area of 100 x 80 super-pixels.

4.4.1. Two-dimensional measurements

As each super-pixel is evaluated separately, a two-dimensional analysis is obtained. Table 4.1 summarizes the results for the six conducted tests. Average (av) and standard deviation (std) were calculated for the analyzed super-pixels. Looking at the average values of θ, our test scheme for the quarter wave-plate becomes obvious: 0°, 10°, 20°, 30° and 40°. Measurements of angle θ describe the relative position of one of the refractive index axes in the range [0°,90°] without distinguishing between slow and fast axis (compare section 4.2). Results for Test 2 are depicted in Fig. 4.5. The mean measured phase difference Δ throughout the wave plate is 1.597. This is reasonably close to the ideal phase difference of $\pi/2 \approx 1.571$ a quarter-wave plate is supposed to induce. The

difference of about 0.026 is well within the retardance tolerance of the quarter-wave plate:

$$\Delta = \frac{2\pi}{\lambda} \cdot \pm(\delta n \cdot L) = 2\pi \cdot \frac{\pm 10nm}{526nm} \approx \pm 0.12 \tag{4.19}$$

The degree of polarization *DOP* is close to 100%, indicating low ambient light influence. However, the conditions of these measurements were similar to the conditions of the calibration measurements, where the *DOP* was set to 100% and thus the calibration function will have eliminated most ambient conditions. Rather surprising are the results for the correction angle $d\phi$ of about 2.5°. In Fig. 4.4 and during the camera calibration, the misalignment between camera and initial polarizer position $P(\phi = 0)$ was found to be $d\phi < \pm 0.5°$. We therefore assume that the quarter-wave plate rotates the incident polarized light. Test 5 was conducted with strong ambient light. This influenced the degree of polarization (DOP) but was found to have little to no effect on the other parameters. Therefore, by introducing parameter DOP in relation (4.16) this approach can be applied when ambient light is present.

Table 4.1. Average (av) and standard deviation (std) of the 144 measurement points spaced over the two-dimensional area, conducted with (QW) and without (-) the quarter-wave plate.

Test	*1*	*2*	*3*	*4*	*5*	*6*
Specimen	QW	QW	QW	QW	QW	-
$\Delta\, av$	1.59	1.60	1.60	1.60	1.60	0.04
$std\ \Delta$	0.005	0.005	0.005	0.005	0.005	0.04
$\theta\, av$	0.3°	10.5°	20.2°	30.2°	40.7°	-
$std\ \theta$	0.1°	0.1°	0.1°	0.1°	0.1°	-

DOP *av*	100%	100%	100%	100%	95%	100%
std DOP	<1%	<1%	<1%	<1%	<1%	<1%
$d\phi$ *av*	1.5°	2.6°	2.2°	3.0°	2.3°	0.2°
std $d\phi$	0.2°	0.2°	0.2°	0.2°	0.3°	0.1°

4.4.2. Number of required polarizer positions

For each test in Table 4.1 we analyzed 181 polarizer positions $P(\phi)$ from $\phi = 0°$ up to $\phi = 180°$. This represents a rather large experimental effort, so this section investigates the possibility to decrease the number of polarizer positions. The question of how many different positions are necessary to achieve reasonable results is studied in Fig. 4.6 using an exemplary super-pixel. The parameters $\Delta, \theta, DOP, d\phi$ were fitted applying only a limited number of the available polarizer positions $P(\phi)$. At first, only one position was used. This is similar to equations (4.10), which calculate Δ, θ from single values for S_{1_N}, S_{2_N}. When only one position is considered, no results for the *DOP* and $d\phi$ are available, as our fitting algorithm requires at least the same number of equations as parameters. The *DOP* is then set to 100% and $d\phi = 0°$. We analyzed all 180 different positions, ranging from $\phi = 0° - 179°$. The results are shown in Fig. 4.6 and are labelled #1. We then plotted the results considering two, three, four, six and nine polarizer positions. The angles between the positions are shown in the x-axis. By assuming periodic continuation of the polarizer positions from $0 - \pi$ to $\pi - 2\pi$ (meaning position $\phi = 180°$+x is equal to position $\phi = x$), we analyzed all 180 possible combinations. For example, in the case of 3 positions, we considered

positions $\phi_1 = x, \phi_2 = x + 60°, \phi_3 = x + 2 \cdot 60°$ and varied x from 0°-179°. The starting position for the fitting algorithm was $\Delta_0 = \pi$, $\theta_0 = 0°$, $\mathrm{DOP}_0 = 100\%$, $d\phi = 0°$.

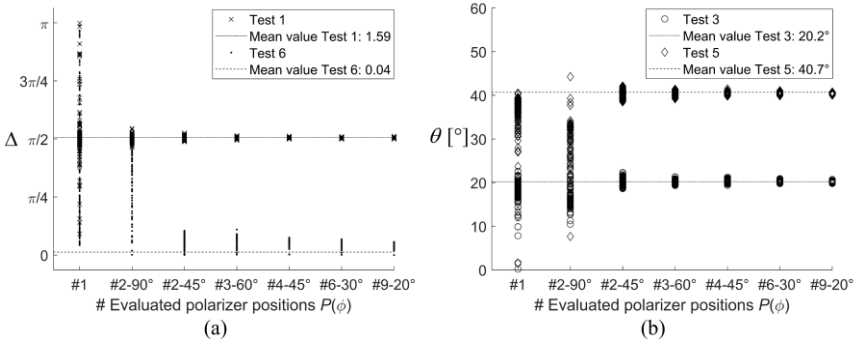

Fig. 4.6. Optimization results for one super-pixel. The number # on the x-axis corresponds to the number of polarizer positions considered in the fitting algorithm and the angle [°] to the relative difference of the positions: (a) Phase difference and (b) Relative position of the refractive index axis.

Figure 4.6 indicates that configurations #1 and #2-90° are not suitable for birefringence measurements. Acceptable results are available for #2-45°, #3-60° and thereafter. However, compared with Table 4.1, accuracy in the area close to $\Delta = 0$ is decreased. The general procedure is relatable to a phase-stepping method for a plane polariscope composed of two rotatable linear polarizers. One polarizes the incident light (Polarizer: orientation ϕ) and the other analyzes the transmitted light (Analyzer). The polarization camera herby concurrently acts as four analyzer positions (0°, 45°, 90°, 135°). The #2-45° configuration can be interpreted as a phase-stepping method that gives eight intensity measurements for the governing phase-stepping equations (Ajovalasit et al., 1998; Ramesh, 2000). This is summarized in Table 4.2 together with the method conducted by Nurse (1997) for

comparison. As Nurse (1997) is using a three-wavelength approach, we suggest the use of a color polarization camera in this context.

Table 4.2. Intensity measurements 1-8 of the equivalent Polarizer (P) and Analyzer (A) positions for a plane polariscope phase-stepping method of the #2-45° configuration in comparison with the procedure described by Nurse (1997). The fields marked with (-) indicate which measurements have not been conducted.

	1	2	3	4	5	6	7	8
#2-45° configuration:								
P:	0°	0°	0°	0°	45°	45°	45°	45°
A:	0°	45°	90°	135°	0°	45°	90°	135°
Nurse (1997):								
P:	0°	-	0°	0°	45°	-	45°	45°
A:	0°		90°	135°	0°		90°	135°

4.4.3. Error analysis

This subsection investigates the effect of inevitable measurement errors on the result quality. Assuming an equal measurement uncertainty for S_{1_N} and S_{2_N} of δS_N, the error propagation on phase difference and extinction angle are modelled from the ideal relations as

$$\frac{d\Delta}{dS_N} = \frac{1}{\frac{dS_N}{d\Delta}} = \frac{1}{\left\| \begin{bmatrix} \frac{\partial S_{1_N}}{\partial \Delta} \\ \frac{\partial S_{2_N}}{\partial \Delta} \end{bmatrix} \right\|_2} = \frac{1}{\sqrt{\left(\frac{\partial S_{1_N}}{\partial \Delta}\right)^2 + \left(\frac{\partial S_{2_N}}{\partial \Delta}\right)^2}} = \frac{1}{\left|\sin[2(\phi-\theta)]\cdot\sin\Delta\right|}, \tag{4.20}$$

and

$$\frac{d\theta}{dS_N} = \frac{1}{\frac{dS_N}{d\theta}} = \frac{1}{\left\| \begin{bmatrix} \frac{\partial S_{1_N}}{\partial \theta} \\ \frac{\partial S_{2_N}}{\partial \theta} \end{bmatrix} \right\|_2} = \frac{1}{\sqrt{\left(\frac{\partial S_{1_N}}{\partial \theta}\right)^2 + \left(\frac{\partial S_{2_N}}{\partial \theta}\right)^2}} = \frac{1}{2(1-\cos\Delta)}. \tag{4.21}$$

We can see that measurement errors for the phase difference Δ are larger when Δ is close to zero or multiples of π. This can be seen in the Δ results of Table 4.1. For all super-pixels, the same calibration function [Eq. (4.18)] was applied, as differences between the calibration functions were negligible. Because of the similar super-pixel performance, the standard deviations of Tests 1-5 are small (std Δ = 0.005). However, in agreement with Eq. (4.20), these small differences are intensified in Test 6, causing the resulting non-zero average value of 0.04 and the standard deviation to be nearly ten times higher (std Δ = 0.04). Equation (4.20) also explains the slower convergence to the mean value of Test 6 in Fig. 4.6 (a). Measurement results for θ tend to be inaccurate if Δ is zero (in this case, θ does not exist) or a multiple of 2π. The term $\sin[2(\phi-\theta)]$ in relation (4.20) explains the poorly performing cases of configurations #1 and #2-90° in section 4.4.2. If the polarizer positions ϕ happen to inconveniently lead to $\sin[2(\phi-\theta)]=0$, measurements will be corrupted.

4.4.4. Exemplary test case

The images in Fig. 4.7 show an exemplary test case with three plastic cuvettes and one glass cuvette as specimens. Internal stresses in the plastic cuvettes induce

birefringence whereas little to no birefringence is seen with the glass cuvette. The visible result is the cumulated birefringence of both surfaces. The optical materials and measurement method of section 4.3 were used and 4 polarizer positions were taken into account: $\phi = 0°, 45°, 90°, 135°$. Any desired spatial resolution is possible with the actual camera resolution being the limiting factor. In this case, we analyzed every eighth super-pixel position. Each intensity $I_0, I_{45}, I_{90}, I_{135}$ was derived by averaging the corresponding 37 pixels in a circular neighborhood with a diameter of 8 super-pixels. Fig. 4.7 (c) is a vector plot where the length corresponds to the measured phase difference Δ and the orientation to the relative position of the refractive index axes between [$-\pi/4, \pi/4$]. Fig. 4.7 (d) is a two-dimension contour plot visualizing coherent areas. We can see that phase differences range from 0 to π, therefore some areas will most likely exceed the measurement limit of π radians. However, these cases exceeding the limit are few and occur in close proximity.

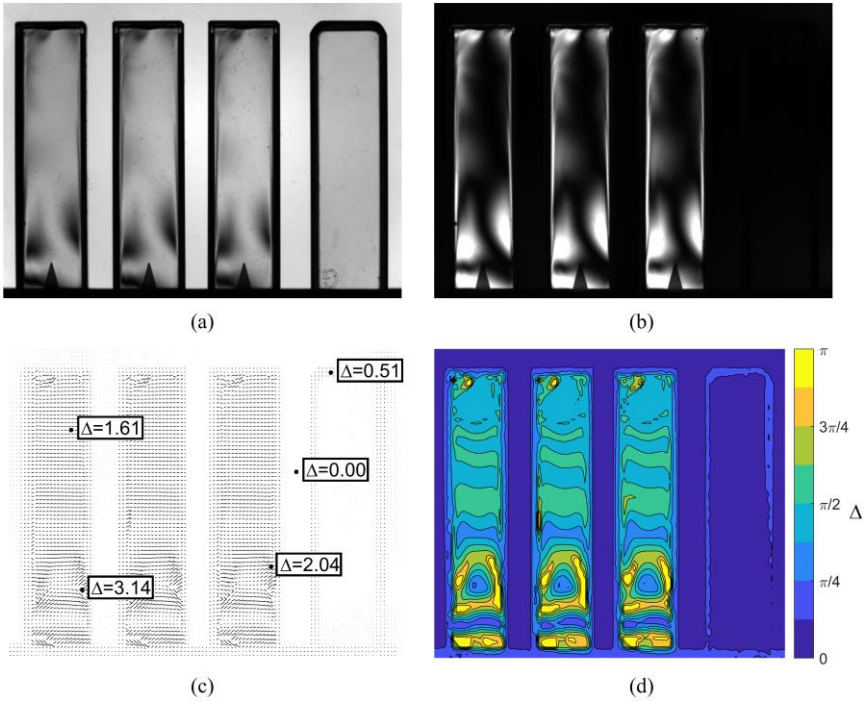

Fig. 4.7. Two-dimensional birefringence measurement of an exemplary test case with three plastic cuvettes (first three from the left) and a glass cuvette (right): (a) Parallel polarizers ($\phi = 0, I_0$). (b) Crossed polarizers ($\phi = 0, I_{90}$). I_0 and I_{90} refer to the corresponding images of the polarization camera. (c) Vector plot with the length of the vector corresponding to the measured phase difference Δ and the orientation to the relative position of the refractive index axes. (d) Filled 2-D contour plot with 7 isolines separating 8 levels of birefringence. Plot (c) and (d) show, that the three plastic cuvettes to the left have a similar birefringence distribution, resulting from internal stresses presumably due to the same manufacturing process. The glass cuvette to the right does not show any birefringence above $\Delta > \pi/4$ but the edges induce phase differences between $\pi/8 < \Delta < \pi/4$.

4.5. Conclusion

The described technique presents a practical approach to measure two-dimensional birefringence. The proposed procedure is able to identify optical retardations of up to half the wavelength of light (phase differences π rad) and gives the relative positions of the refractive index axes. In comparison to methods based on circularly polarized light, the use of linearly polarized light increases the measurement range for retardation but cannot distinguish between the fast and the slow axis. It may represent an attractive alternative to previous methods, especially in the case of phase differences larger than $\pi/2$. The experimental setup and data analysis are comparatively simple and enable the rapid evaluation of a large sample area. The use of a polarization-sensitive camera in this measurement context is promising and suggests that further research in the field should be undertaken.

5. Optical characterization method for birefringent fluids using a polarization camera

The content of this chapter has been published in (Lane et al., 2021b):

Lane, C., Rode, D., & Rösgen, T. (2021b). Optical characterization method for birefringent fluids using a polarization camera. *Optics and Lasers in Engineering*, *146*, 106724. https://doi.org/10.1016/j.optlaseng.2021.106724

Author contribution statements:

Connor Lane developed the theory, designed the experimental setup, analysed the data, and wrote the manuscript. David Rode helped to carry out the experiments and sort out the references. Thomas Rösgen developed the camera software and directed the project. All authors discussed the results and helped formulate the manuscript.

Note:

The following refers to the author version. Please refer to the original paper for the typeset version. The text is quoted verbatim; however, the citation style and the numbering of the figures and equations have been aligned to this document and are therefore changed. The figures are reprinted with permission (see Elsevier permissions (Elsevier, 2022)).

Funding:

This research did not receive any specific grant from funding agencies in the public, commercial, or not-for-profit sectors.

Declaration of Competing Interest:

The authors declare that they have no known competing financial interests or personal relationships that could have appeared to influence the work reported in this paper.

Abstract

Various techniques exist for characterizing a birefringent fluid by means of extinction angle and birefringence. We summarize these techniques and present a new procedure. The approach derives the first three Stokes parameters from images of a polarization camera and uses them to calculate the corresponding streaming birefringence by applying the Mueller matrix calculus. The required theory and a suitable experimental set-up are described. We apply the new measurement procedure to two Xanthan gum solutions and characterize their optical properties. The results agree with published data. Advantages of the new measurement technique are ease of handling, high robustness against optical imperfections and the possibility to measure a continuous response to shear in a single test series.

Keywords: Optical Characterization; Birefringence; Polarization Camera; Stokes Parameter; Mueller Calculus; Xanthan Gum Solutions

5.1. Introduction

If a fluid is composed of optically anisotropic particles or molecules, shear induced birefringence may occur during flow. At rest, Brownian motion randomly orientates the constituents. Therefore, on a larger scale, the fluid appears isotropic. Shear and viscous forces, on the other hand, cause local alignment leading to a preferential orientation that induces birefringence as a form of optically anisotropic response (Cerf & Scheraga, 1952; Pih, 1980; Tsvetkov,

1964). Physically the alignment is based on either the stretching and orientation of long polymer-like chains or the deformation or orientation of suspended macromolecules or colloidal particles (Jeffery, 1922; Pih, 1980). Birefringent fluids exhibit shear-dependent polarization behavior, an effect called photoelasticity. Maxwell (1874) used this effect to visualize fluid motion and documented the phenomenon in 1873, and it has continuously attracted attention ever since. Reviews are given by Cerf and Scheraga (1952), Pih (1980) and Peterlin (1976), and a summary of these reviews can be found in the study conducted by Hu et al. (2009). Known birefringent fluids are for example Canada balsam (Maxwell, 1874), vanadium pentoxide (Freundlich, 1916; Humphry, 1922), cetyltrimethylammonium bromide (CTAB) (Decruppe et al., 1995), bentonite (Decruppe et al., 1989), tobacco mosaic virus (Decruppe et al., 1989; Hu et al., 2009; Sutera & Wayland, 1961), milling yellow (Peebles et al., 1964) and Xanthan (Chow & Fuller, 1984; Kaap, 2010; Meyer et al., 1993; Smyth et al., 1995; Yevlampieva et al., 1999) solutions. We focus on Xanthan solutions in this study.

Birefringent fluids can be used in flow measurement and visualization techniques. They have a major advantage in that they allow non-invasive measurement and therefore offer the possibility of studying shear rates and shear stresses within the bulk fluid (C. Sun & Huang, 2016). This is particularly interesting for the study of biomedical flows where flow-induced stresses can evoke physiological responses. Currently no single ideal measurement technique has been established and this allows room for new approaches (Deplano & Siouffi, 1999; Papaioannou & Stefanadis, 2005). Various research groups have applied birefringence techniques for this purpose (Rankin et al., 1989; Y.-D. Sun et al., 1999), and new measuring methods are emerging (Schneider, 2013). In biomedical flows, shear

rates of all scales are of interest including the range below 100 1/s (Walker et al., 2014).

When the incident light beam is perpendicular to the flow direction and the shear gradient, the optical properties of the birefringent fluid are similar to those of a uniaxial crystal plate with two main optical axes and their corresponding refractive indices n_1 and n_2 (Tsvetkov, 1964). The optical response of the fluid is then characterized by two quantities (Pindera & Krishnamurthy, 1978). The first is the birefringence Δn. This is the absolute difference between the two main refractive indexes n_1, n_2:

$$\Delta n = |n_2 - n_1| \tag{5.1}$$

The second is the extinction angle χ. This is the angle between the flow direction and the refractive index axis. The relationship between flow direction, refractive index axis and the resulting extinction angle χ is illustrated in Fig. 5.1.

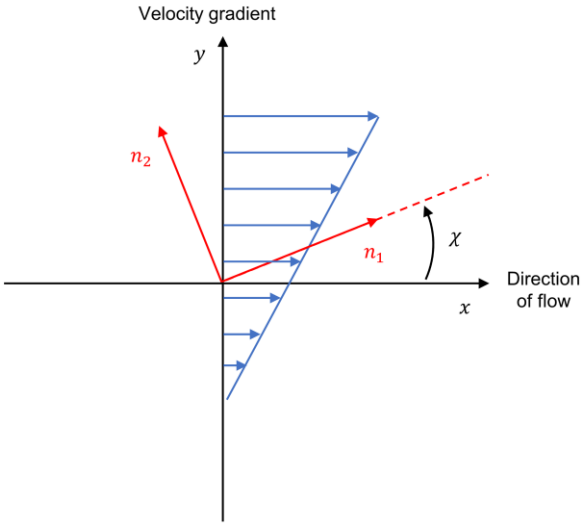

Fig. 5.1. Extinction angle χ of a birefringent flow in the velocity field $u = [Gy, 0, 0]^T$.

Peterlin and Stuart (1939a, 1939b) investigated and summarized the relationship between a flow field u in Cartesian coordinates:

$$u = [Gy, 0, 0]^T \tag{5.2}$$

with the velocity gradient and shear rate $\dot{\gamma} = G$, the particle orientation of rigid submicroscopic optically anisotropic ellipsoids and the position of the resulting main optical axes n_1, n_2. Following their findings, it is notable that the refractive index axis is not necessarily aligned with the particle axis of the ellipsoids, and that birefringence is related to size, shape and optical properties of the particles and the solute, whereas the extinction angle only depends on the size and shape of the particles.

Both properties are functions of the shear rate $\dot{\gamma}$:

$$\Delta n = f(\dot{\gamma}) \tag{5.3}$$

$$\chi = g(\dot{\gamma}) \tag{5.4}$$

These relationships summarize the optical response of a material under shear. Theoretical approaches relating birefringence to strain rates have been published by Wayland (1964, 1960), and Aben and Puro (1993, 1997). Wayland developed a 2D orientation theory that relates birefringence and optical axes directions to the principal strain rate. He assumed ellipsoidal particles and took into account their optical anisotropy, their rotary-diffusion coefficient and axial ratio as well as their mean index of refraction and the volume concentration of the solution. Aben and Puro presented a photoelastic tomography approach for 3D flow birefringence studies by assuming weak birefringence and interpreting integrated photoelasticity as tensor-field tomography. With the help of the Radon transform, Aben and Puro derived 3D field equations which link the optical response of the flow to its velocity field.

For the experimental characterization of birefringent fluids, various test devices and measurement procedures have been developed to determine Eqs. (5.3) and (5.4). Cerf and Scheraga (1952) as well as Chow and Fuller (1984) summarize the basic concepts. Most test procedures are of the Taylor-Couette type in which the fluid is placed in the gap between two concentric cylinders. This apparatus is considered best practice (Tsvetkov, 1964). Rotating the inner or the outer cylinder causes the fluid to be sheared. If the gap is small compared to the cylinder radius, the velocity gradient within the gap is close to constant. The resulting birefringence in the gap is most easily studied by placing two crossed linear polarizers at the top and the bottom of the cylinders, viewing the gap from one

end of the longitudinal axis and illuminating from the other end. Light passing through the first linear polarizer will be linearly polarized with half the intensity $I_{in}/2$. When the fluid is at rest the gap appears dark. When rotating one of the two cylinders, the fluid is subject to shear and the shear induces birefringence. As a consequence, the resulting light emerging from the gap after passing through the fluid is in general elliptically polarized. Depending on the amount of birefringence, the gap will appear bright with a dark cross. This cross is referred to as the isoclinic cross. The isoclinic cross occurs when one of the refractive index axes is in line with the linear polarization. The perceivable light intensity varies with (Pih, 1980):

$$I_{90}(\phi) = \frac{I_{in}}{2} \cdot \sin^2[2(\chi + \phi)] \cdot \sin^2[\pi \Delta n \frac{L}{\lambda}]. \tag{5.5}$$

Here L is the path length, λ the wavelength of the light, and ϕ the angular coordinate. The measurable intensity pattern Eq. (5.5) depends on the optical parameters Δn and χ. The subscript indicates the angle of the polarizers relative to each other. The basic test set-up, as stated by Chow and Fuller (1984), is shown in Fig. 5.2. Figure 5.3 shows part of the resulting isoclinic cross and defines the parameter α as the angle between refractive index axis and plane of vibration of the incident light, in our case corresponding to the horizontal polarizer (Peebles et al., 1964):

$$\alpha = \chi + \phi. \tag{5.6}$$

Generally, the refractive index axis n_1 referred to by α could be the fast axis n_1, with $n_1 < n_2$, or the slow axis. The definition in Fig. 5.3 does not distinguish between fast and slow axis.

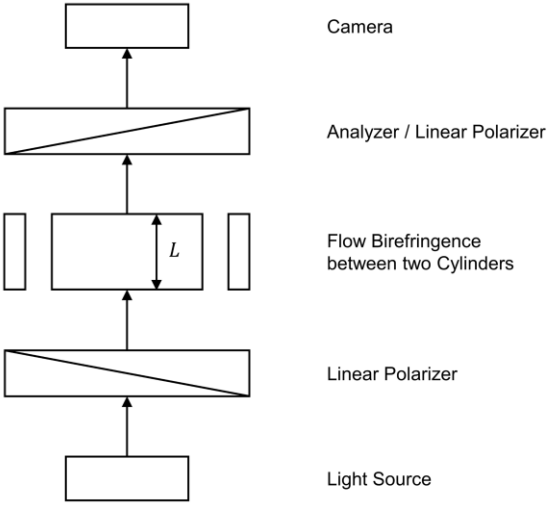

Fig. 5.2. Basic test setup for birefringence studies, as described by Chow and Fuller (1984).

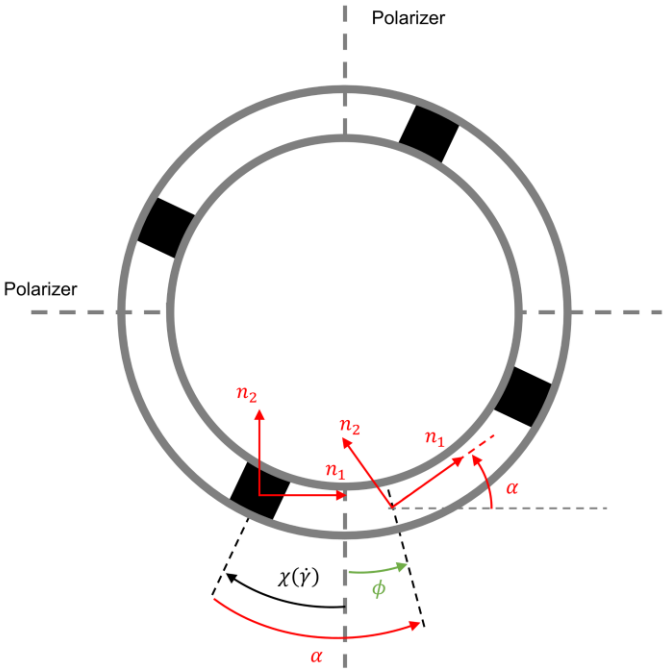

Fig. 5.3. Isoclinic Cross and associated extinction angle of a birefringent fluid in a Taylor-Couette type setting (Peebles et al., 1964).

Chow and Fuller (1984) describe different methods for measuring Δn and χ. The standard approach requires multiple measurements. First, the position of the isoclinic cross and the extinction angle have to be determined. The isoclinic cross occurs when the first sine term in Eq. (5.5) becomes zero and thus the light intensity becomes zero. This is equal to $(\phi + \chi)$ being zero or multiples of $\pi/2$. Rotating $\pm 45°$ from these locations gives the maximum intensity and birefringence can then be derived from the second sine term in Eq. (5.5):

$$\Delta n = \frac{\lambda}{\pi \cdot \mathrm{L}} \sin^{-1} \sqrt{I_{90}/(I_{in}/2)} \,. \tag{5.7}$$

This procedure has to be repeated for each desired velocity gradient and is therefore laborious. Osaki et al. (1979) use a similar approach, measuring at two different points separated by 45° from each other. From these two measurements the two parameters Δn and χ are derived. Although being faster, this approach still requires two consecutive measurements per velocity gradient.

Due to these drawbacks, Chow and Fuller (1984, 1985) designed a technique called 'two color flow birefringence' which uses two lasers of different wavelengths. With this method two separate measurements can be taken simultaneously and so only one measurement setting is required. Extinction angle and birefringence are measured simultaneously. The disadvantages of this method are the complexity of setting up the lasers and the sensitivity of the lasers to disturbances such as air pockets (Fuller, 1990). Fundamentally, this approach implies that the material parameter Δn is wavelength independent. Although the difference in wavelength might be small, the authors indicate that each system must be checked to ensure that any dispersion of Δn at the chosen wavelengths is negligible. This technique has however been successfully used by other researchers (Quinzani et al., 1994).

Another well-established approach is to use a single monochromatic laser and combine the so-called null method with the classical method of Senarmont (De Senarmont, 1840; Janeschitz-Kriegl, 1969; Jerrard, 1948). In the null method, the position of the isoclinic cross (χ) is determined by rotating a crossed polarizer/analyser pair. The method of Sénarmont, also referred to as Sénarmont compensation, uses a rotatable analyser together with a polarizer and a quarter-wave plate to determine small retardations (birefringence) with an accuracy on the order of magnitude of the wavelength of the light. Again, the required manual operation may be considered a drawback of the technique.

A precise method to measure birefringence has also been presented by Matsuura et al. (1978). They used an advanced setup transmitting circularly polarized light through a birefringent medium and applied a Babinet-Soleil plate and a rotating analyser to convert the elliptically polarized wave back into a circularly polarized wave.

Considering Eq. (5.5) it becomes clear that the appearance of the isoclinic cross is due to the first sine term being zero linked with the material parameter χ. The most common and easiest way to measure χ is therefore to use two crossed polarizers and to measure the angle between the polarizers and the cross as indicated in Fig. 5.3. If the second sine term in Eq. (5.5) becomes zero the whole gap appears dark. This is referred to as an isochromatic fringe. In this case, the following relationship holds:

$$\pi \cdot \Delta n \frac{L}{\lambda} = N \cdot \pi \tag{5.8}$$

with N being the fringe order (= 0, 1, 2, 3, …) and hence:

$$\Delta n = N \cdot \frac{\lambda}{L}. \tag{5.9}$$

Birefringence Δn can be therefore measured by counting the isochromatic fringes N as the speed of the rotating cylinder is increased. The order N=0 corresponds to zero birefringence when the liquid is at rest. This simple but effective procedure can be found in McHugh et al. (1987) and is often used to determine the birefringence of milling yellow (Peebles et al., 1964; Schneider, 2013). The method can only measure defined points (isochromatic fringes) and it requires the fluid to show strong birefringence within the range of shear rates investigated, as Eq. (5.9) has to show multiple fringe orders.

In order to use optical fluids for quantitative measurements, reliable data for Δn and χ are necessary. However, variance in the published data of Δn for similar solutions suggests that the optical properties vary depending on how the fluids are produced and the general material quality. Fig. 5.4 shows published results for different Xanthan based birefringent fluids. In practice researchers are therefore advised to calibrate their birefringent fluid. For calibration a simple and convenient characterization method is desirable. It should not require an advanced set-up or a laborious procedure and should be suitable for different types of birefringent fluids. The intention of this study is to present such an approach. Our method allows simultaneous measurement of Δn and χ even in transient flows whilst using only one light source. It can also be fully automated, and no manual adjustments have to be made. As the light source fully illuminates the flow chamber, single disturbances from air pockets do not affect the accuracy of measurements. By using Stokes parameters to determine Δn any effects from optical elements and surfaces of the test configuration are eliminated.

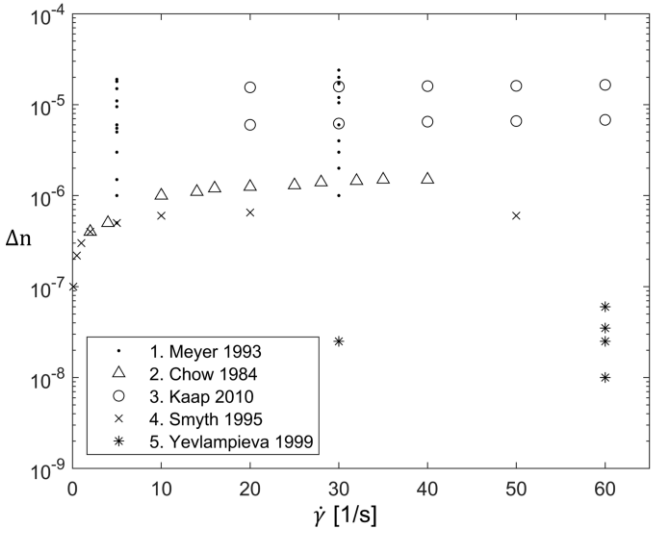

Fig. 5.4. Birefringence for various Xanthan based fluids. Solutions differ in Xanthan concentration and solvent composition: 1. Meyer et al. (1993), Xanthan: 0.05-0.4 wt%, Solvent: Water; 2. Chow and Fuller (1984), Xanthan: 0.03 wt%, Solvent: 90% Glycerin, 10% Water; 3. Kaap (2010), Xanthan: 0.25, 0.5 wt%, Solvent: Water; 4. Smyth et al. (1995), Xanthan: 0.05 wt%, Solvent: Water with 75 wt% fructose; 5. Yevlampieva et al. (1999), Xanthan: 0.011-0.054 , Solvent: Water.

5.2. Materials and Methods

In this section we outline the theoretical approach and experimental evaluation of the measurement procedure. With the help of a polarization camera we can measure three of the four Stokes parameters that characterize the polarization state of an electromagnetic light wave. With this measured data for the polarization state, we can derive the material characteristics Δn and χ inducing birefringence.

5.2.1. Theory

A polarization camera has small polarizers on each pixel. The polarizers vary in direction depending on the pixel position. A schematic representation of a polarized pixel array is given in Fig. 5.5.

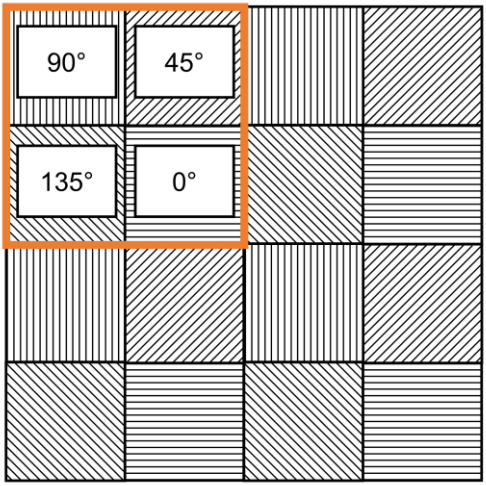

Fig. 5.5. Schematic representation of the polarized pixel arrays in a polarization camera.

A polarization camera is therefore able to simultaneously measure the intensities passing the horizontal (0°), vertical (90°) and two diagonal (45° and 135°) polarizers. The intensities are referred to as: $I_0, I_{45}, I_{90}, I_{135}$. With these intensities, the first three Stokes parameters can be determined (Chipman, 1994):

$$\vec{S} = \begin{bmatrix} S_0 \\ S_1 \\ S_2 \\ S_3 \end{bmatrix} = \begin{bmatrix} I_0 + I_{90} \\ I_0 - I_{90} \\ I_{45} - I_{135} \\ I_R - I_L \end{bmatrix}. \tag{5.10}$$

Ideally, the first Stokes parameter can be computed as $S_0 = I_0 + I_{90} = I_{45} + I_{135}$. The fourth Stokes parameter requires information about the rotation direction of the light (I_R, I_L) and therefore cannot be directly measured with a polarization camera. Stokes parameters describe the state of polarization. Changes in this state resulting from optical components can be modelled with the help of Mueller matrices (Chipman, 1994).

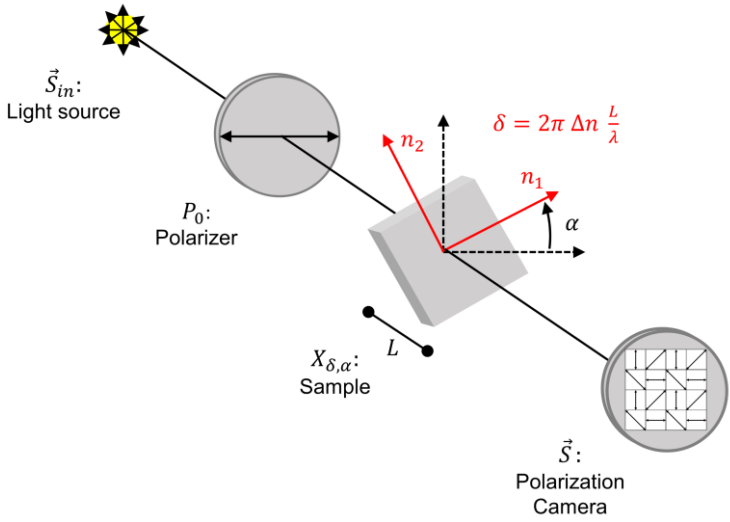

Fig. 5.6. Basic elements of the optical set-up used in this study. Unpolarized light from a light source is linearly polarized before travelling through a birefringent fluid that is represented as linear retarder with refractive indexes n_1 and n_2 and orientation angle α. The resulting Stokes vector $\vec{S}$ is determined by a polarization camera.

The basic elements of the optical set-up used in this study are outlined Fig. 5.6. A light source emits unpolarized light of intensity I_{in}. The corresponding Stokes vector representation is

$$\vec{S}_{in} = \begin{bmatrix} I_{in} \\ 0 \\ 0 \\ 0 \end{bmatrix}. \tag{5.11}$$

The Mueller matrix of the linear polarizer P_0 with axis orientation 0° is

$$P_0 = \frac{1}{2}\begin{bmatrix} 1 & 1 & 0 & 0 \\ 1 & 1 & 0 & 0 \\ 0 & 0 & 0 & 0 \\ 0 & 0 & 0 & 0 \end{bmatrix} \tag{5.12}$$

and the respective matrix of a birefringent medium $X_{\delta,\alpha}$, represented as a linear retarder with δ being the linear phase retardance and α the orientation angle α of the fast axis n_1 $(n_1 < n_2)$

$$X_{\delta,\alpha} = \begin{bmatrix} 1 & 0 & 0 & 0 \\ 0 & \cos^2 2\alpha + \sin^2 2\alpha \cos\delta & \cos 2\alpha \sin 2\alpha(1-\cos\delta) & -\sin 2\alpha \sin\delta \\ 0 & \cos 2\alpha \sin 2\alpha(1-\cos\delta) & \sin^2 2\alpha + \cos^2 2\alpha \cos\delta & \cos 2\alpha \sin\delta \\ 0 & \sin 2\alpha \sin\delta & -\cos 2\alpha \sin\delta & \cos\delta \end{bmatrix}. \tag{5.13}$$

The orientation angle α lies in the range of $[0, \pi]$. The resulting Stokes vector of the light, emitted from the light source and travelling through the polarizer and the birefringent medium can be calculated as

$$\vec{S} = X_{\delta,\alpha} \cdot P_0 \cdot \vec{S}_{in}. \tag{5.14}$$

The resulting output parameters are

$$\begin{bmatrix} S_0 \\ S_1 \\ S_2 \\ S_3 \end{bmatrix} = \begin{bmatrix} \frac{I_{in}}{2} \\ \frac{I_{in}}{2} - \frac{I_{in}}{2}\sin^2 2\alpha\ (1-\cos\delta) \\ \frac{I_{in}}{2}\cos 2\alpha\ \sin 2\alpha\ (1-\cos\delta) \\ \frac{I_{in}}{2}\sin 2\alpha\ \sin 2\delta \end{bmatrix}. \tag{5.15}$$

Taking Eq. (5.10) into account, we also get

$$\begin{aligned} I_0 &= \frac{I_{in}}{2} - \frac{I_{in}}{2}\sin^2 2\alpha\ \sin^2\frac{\delta}{2}, \\ I_{90} &= \frac{I_{in}}{2}\sin^2 2\alpha\ \sin^2\frac{\delta}{2}. \end{aligned} \tag{5.16}$$

The second equation in Eqs. (5.16) is equal to Eq. (5.5). As the polarization camera cannot measure S_3, we shall neglect this fourth Stokes parameter in the following. Using the normalized representation of the Stokes vector $\vec{S}_N = \vec{S}/S_0$ and applying some trigonometry, the remaining first three parameters can be written as

$$\begin{aligned} S_{0_N} &= 1, \\ S_{1_N} &= 1 - \frac{1}{2}(1-\cos 4\alpha)(1-\cos\delta), \\ S_{2_N} &= \frac{1}{2}\sin 4\alpha(1-\cos\delta). \end{aligned} \tag{5.17}$$

The relation between phase retardation δ and the difference of the refractive indexes Δn is given as (Otani, Shimada, Yoshizawa, et al., 1994)

$$\delta = 2\pi \Delta n \frac{L}{\lambda} \tag{5.18}$$

For a known path length L and wavelength λ, δ and Δn are linearly related. We learn from Eqs. (5.17) that the Stokes parameters S_{1_N} and S_{2_N} are periodic with period $\pi/2$ in α and with 2π in δ. The first periodicity means that this approach cannot distinguish between fast and slow vibration axis (n_1 and n_2). The second periodicity leads to Eq. (5.9).

Using (5.17), the Stokes parameters S_{1_N} and S_{1_N} can be computed in the $\delta - \alpha$ space, as shown in Fig. 5.7. For this, α was varied between $0 - \pi$ and δ between $0 - 4\pi$. The latter corresponds to fringe orders 0 ($\delta = 0$; $\Delta n = 0$) and 2 ($\delta = 4\pi$; $\Delta n = 2\lambda/L$).

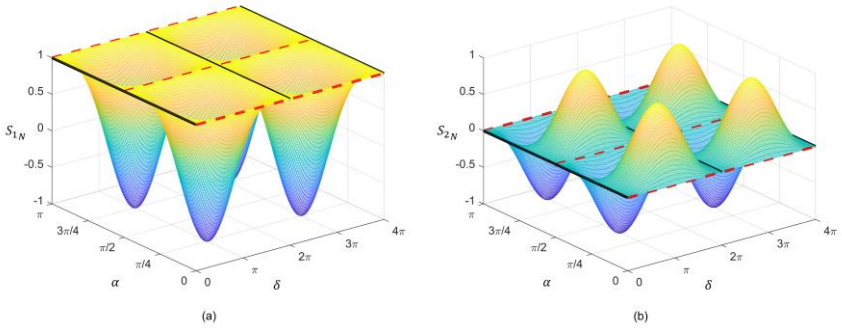

Fig. 5.7. Computed results for the Stokes parameter and as functions of δ and α. No change in polarization can be seen for $\alpha = [0, \pi/2, \pi]$ (Isoclinic cross, red dashed lines) or $\delta = N \cdot 2\pi$ (isochromatic fringes, black solid lines).

In theory, knowing S_0, S_1, S_2 at one point is sufficient to calculate δ and α at this point, as (5.15) gives

$$\begin{aligned} \alpha &= \frac{1}{2}\tan^{-1}\frac{S_0 - S_1}{S_2} \\ \delta &= \cos^{-1}\left[1 - \frac{S_2^2 + (S_0 - S_1)^2}{S_0(S_0 - S_1)}\right] \end{aligned} \tag{5.19}$$

In practice however, measurements with a polarization camera showed that it is not reliable to derive δ and α correctly from a single point measurement. This is particularly the case in the area of isoclinics, where α is close to 0 or $N \cdot \pi/2$ where the orientation of the linear polarization is aligned with one of the main refractive indices n_1 or n_2. The polarization then remains unchanged, and hence one cannot derive δ. In this study we measure the distributions of S_{1_N} and S_{2_N} along an extended circular arc segment and obtain δ and α by fitting Eqs. (5.17) to the measured distributions. Isoclinics therefore present no longer a problem, as they are part of the distributions.

Eqs. (5.19) however help us to understand the measurement ranges of δ and α. The inverse of the cosine function is only defined for values between $[0, \pi]$, but results for δ could also lie between $[-\pi, 0]$. In order to determine the sign, knowledge about the direction of rotation and therefore the fourth Stokes parameter S_3 would be required. Without S_3, any resulting δ is either between $[0, \pi]$ or between $[-\pi, 0]$. Clearly, the range $[-\pi, 0]$ is equal to $[\pi, 2\pi]$ due to periodicity. The measurable range of δ is thus $[0, \pi]$ and that of α is $[-\pi/4, \pi/4]$, which corresponds to $[0, \pi/2]$ due to the periodicity. It is noted once again

that this approach cannot distinguish between fast and slow vibration axes, hence the measurement range. Onuma and Otani (2014) used a similar set-up to the one outlined in Fig. 5.6 but placed a quarter-wave plate at 45° behind the linear polarizer P_0 to create circular polarized light. The authors employed this approach for two-dimensional birefringence distribution measurements and quantified α and δ by measuring I_0, I_{45}, I_{90}, I_{135} at every point. The use of circular polarized light seems to be advantageous compared to the linear arrangement if α and δ are to be determined from single point measurements of I_0, I_{45}, I_{90}, I_{135}, as no isoclinics appear. However, the (dynamic) measurement ranges for δ and α are different. In the circular case, the range for the phase difference δ is $[0, \pi/2]$ and that of α is $[-\pi/2, \pi/2]$ (Onuma & Otani, 2014). As a consequence, the (dynamic) measurable range for the retardation δ is halved, whereas it is doubled for α. When using circular polarized light, the location of the fast axis can be determined. The approach is therefore advantageous when determining two-dimensional birefringence with retardations up to values of $\pi/2$, as it can distinguish fast and slow axes of the birefringent sample. If phase differences δ are larger than $\pi/2$ however, the use of a linear configuration appears advantageous, with the drawback that information about the position of the fast axis is lost. When characterizing birefringent fluids, the extinction angle χ only describes the relative position of the refractive index axes. Moreover, phase differences are likely to exceed values of $\pi/2$. For these reasons, linearly polarized light is recommended for the characterization of birefringent fluids and is used in this study.

5.2.2. Material

For this study two Xanthan solutions of 0.2 and 0.3 wt% were prepared by dissolving Xanthan powder in demineralized water. The powder was stirred into the solution until fully dissolved. Being a food additive, Xanthan is safe to handle and cheap. It shows good birefringence behaviour that has been studied in previous literature (Chow & Fuller, 1984; Kaap, 2010; Meyer et al., 1993; Smyth et al., 1995; Yevlampieva et al., 1999). The Xanthan gum powder used in this study was purchased from Sigma Aldrich. The mixtures were both prepared a week before testing and the error in concentration is about $\Delta c = \pm 0.05$ wt%.

5.2.3. Experimental Procedure

The experimental set-up based on the concept introduced in section 5.1 is shown in Fig. 5.8. A small DC motor rotates the inner cylinder at a given rotation speed. The height of the inner cylinder, equaling the path length L, is 25mm. Two glasses at the top and bottom allow optical access. The outer radius of the inner cylinder and the inner radius of the outer cylinder are 48mm and 49mm respectively, leading to a gap width of 1mm. Due to the gap being small in comparison with the diameter, a constant shear rate within the gap is assumed and modeled as

$$\dot{\gamma} = \frac{\Omega R_{inner}}{R_{outer} - R_{inner}} \tag{5.20}$$

Here Ω is the angular velocity and R_{inner}, R_{outer} the radii of the respective cylinders. In each test sequence, 49 single measurements were conducted by evenly increasing the angular velocity from 0-0.9 1/s, leading to shear rates between 0-43 1/s. All experiments were therefore well below the critical Taylor number (Taylor, 1923), ensuring laminar flow without instabilities. At every measurement point the angular velocity was kept steady for 5 seconds before the

measurements to eliminate any time-dependent birefringence effects (Chow & Fuller, 1984). Light from a halogen incandescent lamp was filtered using a long- and a short pass filter, principally limiting transmission to a spectrum of 650-690nm. This red light was then linearly polarized with an extinction ratio of 10000:1, collimated and redirected through the Taylor-Couette flow. A monochrome polarization camera (Lucid Vision Labs Phoenix PHX050S-P, Schneider Xenon 50mm/0.95 lens) mounted above the set-up captured the optical response created by the birefringent fluid. Preliminary investigations showed that camera-related errors did not influence the results significantly. For each concentration, 15 test series were conducted. For the last 5 series the testing conditions were slightly modified to study the impact of several external parameters: First, a variation of the light source intensity led to the same measurement results. This is not surprising, as the procedure is based on normalized Stokes parameters. Second, the linear polarizer was rotated $\pm 1°$ from its original position. A change of angle of the incident linear polarized light changes the extinction angle in the same manner with respect to a global coordinate system. Taking this into account, the measured results for χ remain the same. Third, unpolarized ambient light was employed. Considering the following two equations, Eq. (22) and Eq. (23), the results were not noticeably affected.

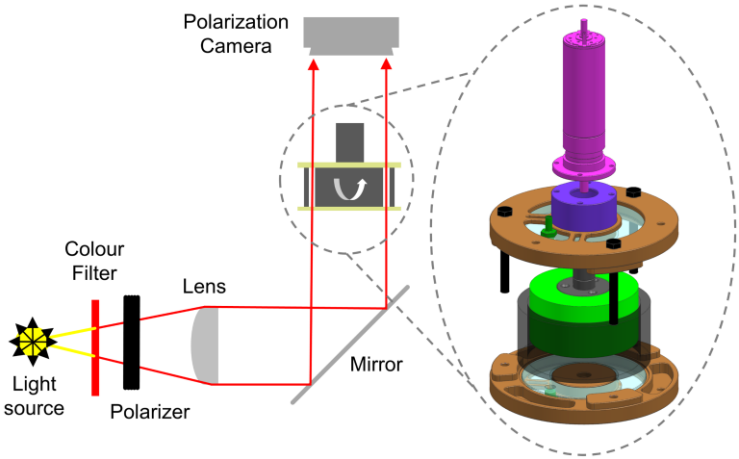

Fig. 5.8. Experimental set-up of the Taylor-Couette flow: Light from a light source is filtered, polarized and sent through the sheared flow. A polarization camera mounted above the experiment captures the optical response.

With the test set up being at rest, the polarization camera was adjusted in such a way that maximum light intensity is measured at I_0^{rest}, minimum intensity at I_{90}^{rest} and equal intensities for I_{45}^{rest} and I_{135}^{rest}. This setting is closest to the desired set-up outlined in Fig. 5.6, with a 0° linear polarizer. However, the image of I_{90}^{rest} still detects some light passing through the gap. These residual intensities arise from stray light reflections. Therefore, the measured Stokes vector will not be completely polarized. This is quantified by the degree of polarization (DOP)

$$\mathrm{DOP} = \frac{\sqrt{S_1^2 + S_2^2 + S_3^2}}{S_0}, \tag{5.21}$$

A partially polarized Stokes vector (DOP<1) can be considered as a superposition of a fully polarized Stokes vector $\vec{S}_P$ and an unpolarized Stokes vector $\vec{S}_U$ (Chipman, 1994):

$$\vec{S} = \vec{S}_P + \vec{S}_U = \mathrm{DOP}\begin{bmatrix} S_0 \\ S_1/\mathrm{DOP} \\ S_2/\mathrm{DOP} \\ S_3/\mathrm{DOP} \end{bmatrix} + (1-\mathrm{DOP})\begin{bmatrix} S_0 \\ 0 \\ 0 \\ 0 \end{bmatrix} \tag{5.22}$$

We assume that the DOP remains constant during one test series (during the increase of shear rate $\dot{\gamma}$) but will vary as a function of ϕ due to non-uniform lighting, irregularities induced by the optical path and reflections from the black cylinder surfaces which are manufactured from Polyoxymethylene (POM). Figure 5.9 indicates the automated image analysis. The intensities $I(\phi)$ were measured at select angular coordinates, with ϕ being the angle as defined in Fig. 5.3.

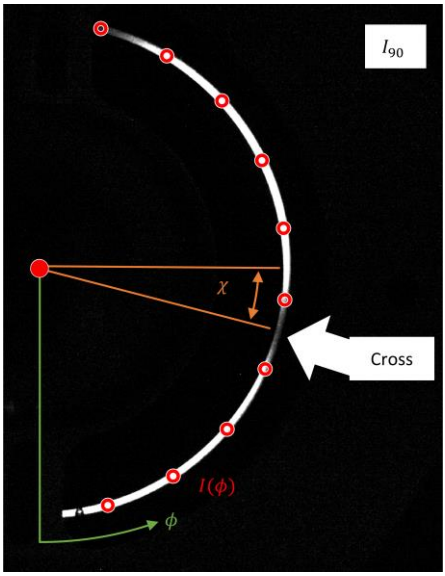

Fig. 5.9. Schematic representation of the intensity evaluation along half of the Taylor-Couette flow under shear. The isoclinic cross is visible to the naked eye.

At rest, the fluid is not birefringent. The Stokes vector will therefore be composed of a purely linear polarized part (linear polarizer) and an unpolarized part (stray contribution). If only linear polarized components are present, S_3 is zero by definition. The DOP can then be calculated as

$$\mathrm{DOP}(\phi) = \frac{2\sqrt{\left(I_0^{rest}(\phi) - I_{90}^{rest}(\phi)\right)^2 + \left(I_{45}^{rest}(\phi) - I_{135}^{rest}(\phi)\right)^2}}{I_0^{rest}(\phi) + I_{45}^{rest}(\phi) + I_{90}^{rest}(\phi) + I_{135}^{rest}(\phi)} \tag{5.23}$$

At every shear rate, the four images of the polarization camera were used to obtain the first three Stokes parameters

$$
\begin{aligned}
S_0^M(\phi) &= \frac{I_0(\phi) + I_{45}(\phi) + I_{90}(\phi) + I_{135}(\phi)}{2}, \\
S_1^M(\phi) &= I_0(\phi) - I_{90}(\phi), \\
S_1^M(\phi) &= I_{45}(\phi) - I_{135}(\phi).
\end{aligned}
\tag{5.24}
$$

Together with the $\mathrm{DOP}(\phi)$, the polarized part of the measured Stokes vector is given as

$$
\vec{S}_P^M(\phi) = \mathrm{DOP}(\phi) \begin{pmatrix} S_0^M(\phi) \\ S_1^M(\phi) / \mathrm{DOP}(\phi) \\ S_2^M(\phi) / \mathrm{DOP}(\phi) \\ - \end{pmatrix}
\tag{5.25}
$$

Here, as $S_3(\phi)$ cannot be measured, it is simply left out. With this approach we measure the distribution of $\vec{S}_P^M(\phi)$ along the gap. In the following, we will drop subscript P but all Stokes parameter refer to the fully polarized part $\vec{S}_P^M(\phi)$.

5.2.4. Data Fitting

In order to compare the measurements with the theoretical distributions Eqs. (5.17), a coordinate transformation is applied for each measurement point at every shear rate, following the geometry relationships outlined in Fig. 5.3. It is important to note that the extinction angle χ is a function of the shear rate and thus the relation between α and ϕ, Eq. (5.6), is a function of the shear rate as well. Eqs. (5.17) can be written as

$$S_{1_N} = \frac{1}{2} + \frac{1}{2}\cos\delta + \frac{1}{2}\cos 4\alpha\ (1-\cos\delta),$$
$$S_{2_N} = \frac{1}{2}\sin 4\alpha\ (1-\cos\delta). \tag{5.26}$$

Using a numerical optimization algorithm, Eqs. (5.26) can be fitted to the measured distributions. We would like to note that for the numerical fitting of the phase difference δ only the magnitude of the two amplitudes $1/2\cdot(1-\cos\delta)$ were considered. This was done in order to avoid distortions due to centerline offset errors.

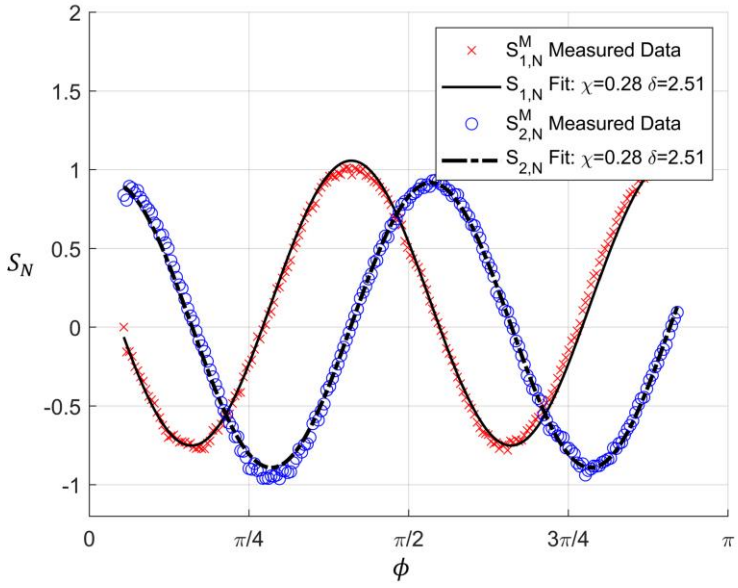

Fig. 5.10. Experimental data $\vec{S}_P^M(\phi)$ and numerical fits for the Stokes Parameter S_{1_N} and S_{2_N} as a function of ϕ. Experiment: 0.3 wt%, $\dot{\gamma}$ =8.2 1/s.

Figure 5.10 shows an example of the normalized Stokes parameters $S_{1_N}^M$ and $S_{2_N}^M$ resulting from the polarized part of the measured Stokes parameters $\vec{S}_P^M(\phi)$ Eq. (5.25). The corresponding numerical fits are also plotted in the figure. Each fit gives an associated extinction angle χ and phase difference δ for the corresponding shear rate $\dot{\gamma}$. This characterises the optical response of the fluid to shear:

$$(\chi, \delta)_{\dot{\gamma}} = Fit[S_1^M(\phi), S_2^M(\phi)]_{\dot{\gamma}} . \tag{5.27}$$

The birefringence value is then calculated using

$$\Delta n = \frac{\lambda}{2\pi L}\delta \tag{5.28}$$

In this study we used a wavelength of 670nm, which is the centerline value of the transmitted light spectrum ranging from 650-690nm. The path length is 25mm. Fitting the optical parameters is independently done for every conducted test series at every measured shear rate $\dot{\gamma}$. Considering the fitting algorithm for δ, it is important to notice that the algorithm takes into account that with increased shear rate the birefringence has to generally increase. This assures that ambiguous solutions do not occur, as the fitted Stokes parameters are periodic with period 2π in δ. Moreover, as discussed in section 5.2.1., any solution of δ being within $[0, \pi]$ could also lie between $[\pi, 2\pi]$. This is also considered in the fitting algorithm. The algorithm requires the step size of the measured shear rates $\dot{\gamma}$ to be small enough to ensure an unambiguous allocation.

The fitting algorithm exhibits weaknesses for phase differences δ close to zero and π. This is due to inevitable measurement uncertainties of the normalized

Stokes parameters. If we assume measurement uncertainties of S_{1_N} and S_{2_N} to be of equal magnitude dS_N, the error propagation considering phase difference and extinction angle can be modelled from Eqs. (5.26) by the derivative of the inverse

$$\frac{d\delta}{dS_N} = \frac{1}{\frac{dS_N}{d\delta}} = \frac{1}{\left\| \begin{bmatrix} \frac{\partial S_{1_N}}{\partial \delta} \\ \frac{\partial S_{2_N}}{\partial \delta} \end{bmatrix} \right\|} = \frac{1}{\sqrt{\left(\frac{\partial S_{1_N}}{\partial \delta}\right)^2 + \left(\frac{\partial S_{2_N}}{\partial \delta}\right)^2}} = \frac{1}{\left|\sin[2(\chi+\phi)]\cdot \sin\delta\right|},$$

(5.29)

and

$$\frac{d\chi}{dS_N} = \frac{1}{\frac{dS_N}{d\chi}} = \frac{1}{\left\| \begin{bmatrix} \frac{\partial S_{1_N}}{\partial \chi} \\ \frac{\partial S_{2_N}}{\partial \chi} \end{bmatrix} \right\|} = \frac{1}{\sqrt{\left(\frac{\partial S_{1_N}}{\partial \chi}\right)^2 + \left(\frac{\partial S_{2_N}}{\partial \chi}\right)^2}} = \frac{1}{2(1-\cos\delta)}. \quad (5.30)$$

Plotting the uncertainty propagations (Fig. 5.11) shows that the extinction angle χ cannot be measured precisely when δ is close to 0 (or multiples of 2π, i.e. the definition of isochromatics). Propagation of uncertainty for the phase difference δ is large when $(\chi+\phi)$ is 0 or multiples of $\pi/2$. This means that the amount of birefringence cannot be measured along an Isoclinic. It also underlines the statements made in section 5.2.1. regarding Eqs. (5.19), that single point measurement of the Stokes parameter are not reliable for determining χ and δ. Our proposed measurement procedure evaluates the Stokes parameters along a

distribution of ϕ that inevitably includes $(\chi+\phi)=\pi/4$ (and/or multiples of it), so we assume that the parameter $(\chi+\phi)$ does not affect the quality of our results. However, measurement uncertainties of δ remain large at $\delta = N \cdot \pi$ (with $N = 0,1,2, ...$), as shown in Fig. 5.11 (a).

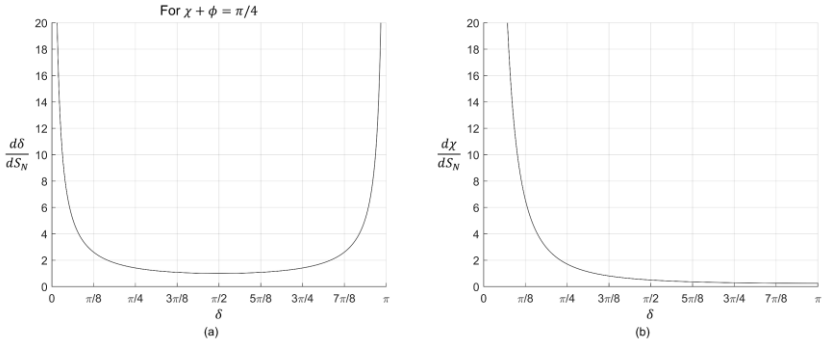

Fig. 5.11. Propagation of measurement uncertainties. (a) Phase difference δ: Measured data close to $\delta = 0, \pi$ are unreliable due to inevitable small uncertainties in dS_N. The plot was created for $\chi + \phi = \pi/4$. (b) Extinction angle χ: If the phase difference is a multiple of 2π (location of an Isoclinic), the extinction angle cannot be measured.

Plotting distributions of S_{1_N} and S_{2_N} for various shear rates in the $\alpha - \dot{\gamma}$ space - implying the knowledge of χ - leads to 3-dimensional plots that show strong similarities to the theoretical results described in section 5.2.1. Such resulting data plots are shown in Fig. 5.12 (a) and (b) for the 0.2 wt% solution and in Fig. 5.13 (a) and (b) for the 0.3 wt% solution. Figures 5.12 (c), (d) and 5.13 (c), (d) exemplify the corresponding superimpositions of the experimental results onto the theoretical distributions in the $\alpha - \delta$ space.

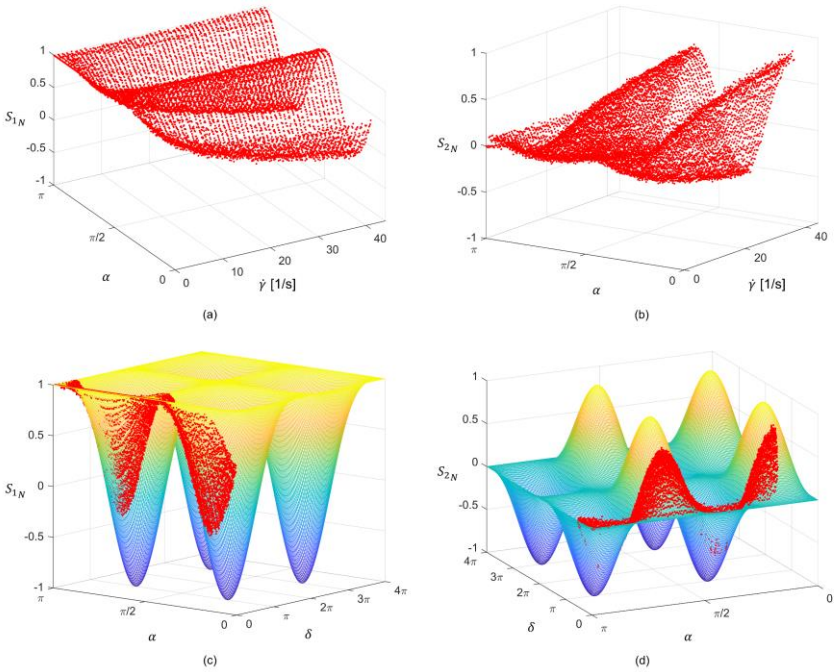

Fig. 5.12. Experimental data of the Stokes Parameters for a Xanthan Solution of 0.2 wt%. (a) $S_{1_N}^M$ and (b) $S_{2_N}^M$: Data as a function of α and $\dot{\gamma}$. (c) $S_{1_N}^M$ and (d) $S_{2_N}^M$: Superimposed with the theoretical distributions of Fig. 5.7.

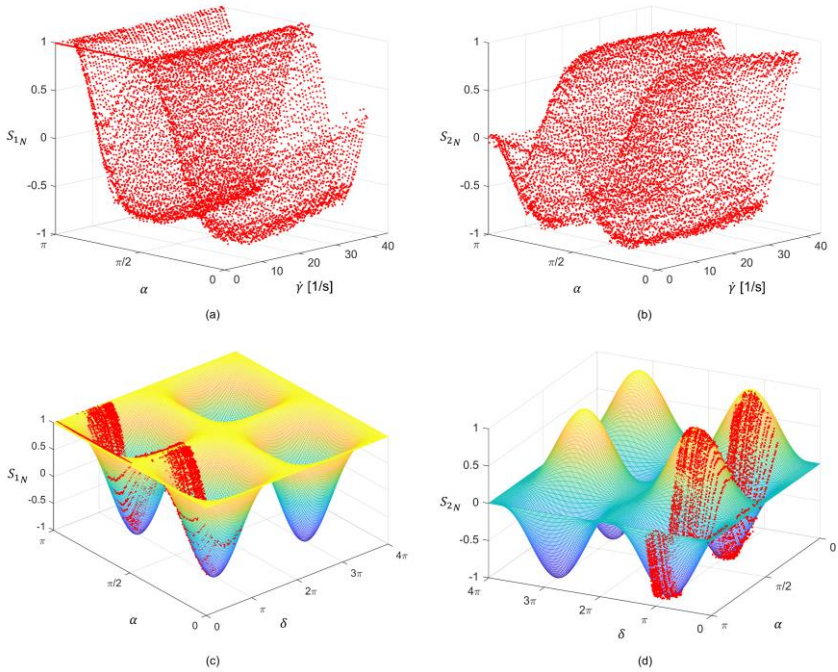

Fig. 5.13. Experimental data of the Stokes Parameters for a Xanthan Solution of 0.3 wt%. (a) $S_{1_N}^M$ and (b) $S_{2_N}^M$: Data as a function of α and $\dot{\gamma}$. (c) $S_{1_N}^M$ and (d) $S_{2_N}^M$: Superimposed with the theoretical distributions of Fig. 5.7.

5.3. Results and Discussion

The results of the experiments described in section 5.2 can be compared with the relevant literature. Advantages and drawbacks of the applied optical characterization method can then be identified. The data considered are the mean values of the experimental series. The error bars indicate full range between minimum and maximum values within which all experiments fall.

5.3.1. Measurement of extinction angle

The evaluated extinction angles χ are shown in Fig. 5.14 for Xanthan solutions of 0.2 and 0.3 wt%, respectively. Within measurement errors, the curve of 0.3 wt% is slightly lower than the 0.2 wt% curve. The shapes of both curves follow the usual result of decreasing extinction angle with increasing shear rate (Chow & Fuller, 1984). Both figures also show that our results are in good agreement with the corresponding data published by Meyer et al. (1993), and thus we conclude that our measurements are consistent. The variances are bigger for the 0.2 wt% Xanthan solutions. The reason for this may be the parameter sensitivity of the experiments on the δ -axis, as discussed in section 5.2.4. and shown in Fig. 5.11 (b). This parameter selection is defined by the experimental design parameters: path length *L* and wavelength λ (compare Eq. (5.18)). For the 0.2 wt% case, most data fits are half way up the slope and not close to the peak, which is defined to be at $\delta = \pi$ and thus at $\Delta n = \lambda/(2L) = 1.32 \cdot 10^{-5}$ in our case. Therefore, the amplitudes of the corresponding Stokes parameter distributions are lower for the 0.2 wt% compared to the 0.3 wt% solution, which are gathered closer to the peak. The fits are more consistent throughout the test series of 0.3 wt%, leading to smaller deviations of the resulting extinction angles χ and suggesting that measurement accuracy is higher in the region around $\delta = \pi$ and thus $\Delta n = \lambda/(2L) = 1.32 \cdot 10^{-5}$ (or multiples thereof).

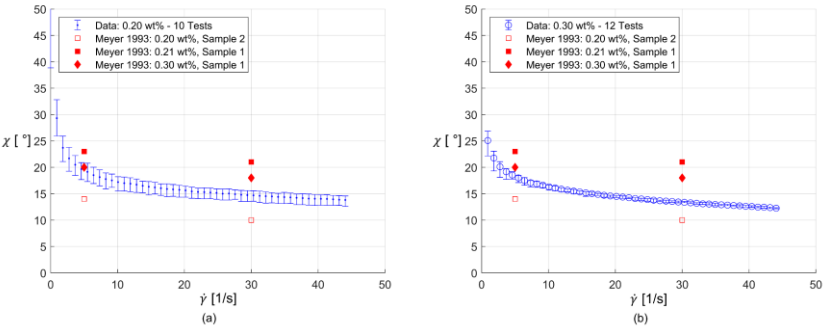

Fig. 5.14. Shear rate dependent extinction angle χ for Xanthan solutions compared with relevant literature data (Meyer et al., 1993). (a) 0.2 wt%. (b) 0.3 wt%.

5.3.2. Measurement of birefringence

Birefringence results are plotted in Fig. 5.15 together with the data published by Meyer et al. (1993) The measurements are in the correct order of magnitude and appear consistent. It can be seen that variances are higher in the area around $\Delta n = \lambda/(2L) = 1.32 \cdot 10^{-5}$ (equal to $\delta = \pi$). This is in line with the considerations discussed in section 5.2.4. and Fig. 5.11 (a). As outlined in section 5.2.1., results for Δn are not unique within one period, as any resulting Δn can be either between [0, $\lambda/(2L)$] or between [$\lambda/(2L)$, λ/L]. Therefore, the fitting algorithm shows decreased accuracy for birefringence values close to $\lambda/(2L)$, as Δn could be allocated below or above the value of $\lambda/(2L)$. (This would also hold for values close to λ/L. For all other values the assignment is unambiguous due to the assumption of monotonically increasing birefringence. Figure 5.15 shows that a higher concentration in Xanthan leads to higher birefringence. The shapes of both curves are similar to the shape of the curve plotted by Chow and Fuller

(1984) in Fig. 5.4. At low shear rates, the gradient of the curve is highest and with increasing shear rates the gradient decreases. Meyer et al. (1993) examined two different Xanthan samples from two different suppliers. Despite using similar concentrations, both samples showed different birefringence (data points plotted with and without filling effect in Fig. 5.15).

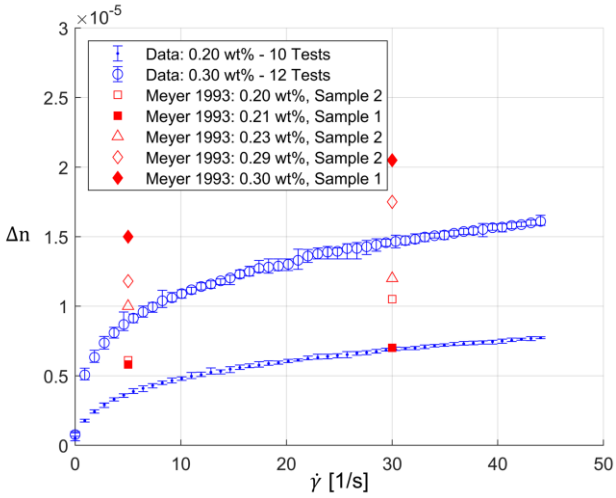

Fig. 5.15. Shear rate dependent birefringence of Xanthan solutions of 0.2 and 0.3 wt% in comparison with the literature (Meyer et al., 1993).

The discrepancy between our results and the data published by Meyer et al. could therefore be related to material differences not taken into account in this study. Another source of error may come from the experimental set-up. Many of the established birefringent measurement techniques described in section 5.1 apply a laser with a narrowly defined wavelength λ. Meyer et al. use a helium-neon laser with 632.8nm wavelength to obtain the data given in the plots. We use a halogen lamp and two filters to narrow the transmitted wavelengths down to the range between 650 – 690nm (see section 5.2.3.) and substitute a wavelength of 670nm

to obtain our results. Therefore, an influence of λ within this range cannot be excluded and the propagated error in birefringence is estimated as

$$Error\,\Delta n = \frac{\Delta\lambda}{L} = \frac{20nm}{2.5cm} \approx 0.1 \cdot 10^{-5}\,. \tag{5.31}$$

5.4. Conclusions

The new measurement procedure to characterize birefringent fluids represents an attractive alternative to previous methods. The advantages are a continuous analysis with increasing shear rates, high resilience towards optical imperfections in the beam path and the possibility to determine extinction angle and birefringence simultaneously. Compared to established methods, the experimental set-up appears easier to handle. It was successfully applied to measure extinction angle and birefringence of two Xanthan Gum solutions. The results are in agreement with the literature. It is expected that the accuracy of the method can be improved further by employing a narrowband light source (e.g. LED or laser) instead of the present finite bandwidth source

6. Birefringent properties of aqueous Cellulose Nanocrystal suspensions

The content of this chapter has has been published in (Lane, Rode, et al., 2022b):

Lane, C., Rode, D., & Rösgen, T. (2022b). Birefringent properties of aqueous cellulose nanocrystal suspensions. *Cellulose*, 1-15. https://doi.org/10.1007/s10570-022-04646-y

Author contribution statements:

Connor Lane developed the theory, designed the experimental setup, analysed the data, and wrote the manuscript. David Rode helped to carry out the experiments and sort out the references. Thomas Rösgen developed the camera software and directed the project. All authors discussed the results and helped formulate the manuscript.

Note:

The following refers to the author version. Please refer to the original paper for the typeset version. The text is quoted verbatim; however, the citation style and the numbering of the figures and equations have been aligned to this document and are therefore changed. The figures are reprinted with permission (see Rights and Permission, Author reuse (Springer, 2022)).

Funding

The authors declare that no funds, grants, or other support were received during the preparation of this manuscript.

Competing Interests

The authors have no relevant financial or non-financial interests to disclose.

Abstract

Birefringence measurements of aqueous cellulose nanocrystal (CNC) suspensions are reported. Seven suspensions with concentrations between 0.7-1.3 percentage per weight are sheared in a Taylor-Couette type setting and characterized using a birefringent measurement technique based on linear polarized light and acquisition with a polarization camera. Steady state measurements with shear rates up to 31 1/s show extinction angles of 23-40° and birefringence in the order of 1e-5. The findings demonstrate the utility of CNC suspensions for flow birefringence studies.

Keywords: Flow birefringence, Cellulose nanocrystal suspensions, Optical characterization, Polarization camera, Taylor-Couette flow

6.1. Introduction

Birefringent fluids are composed of optically anisotropic particles (colloidals) or macromolecules (polymers) (Merzkirch, 2001). At rest, these particles or macromolecules are randomly orientated by Brownian motion and the fluid appears optically isotropic. When under the effect of shear, the particles align in a preferential direction and the fluid becomes birefringent. This phenomenon is also known as flow birefringence and has been studied ever since it was first described by Maxwell (1874). Flow birefringence and birefringent fluids are of interest for two reasons: the study of particles, macromolecules or polymer chains (Cerf & Scheraga, 1952; Fuller, 1995a; Janeschitz-Kriegl, 1983; Wayland, 1964); and the visualization and study of flows and shear rates (Pih, 1980). Macromolecular stretching and orientation as well as particle alignment lead to

birefringence and influence the rheology. Birefringence is therefore linked to the rheological behavior and researchers have studied this relation. Several birefringent fluids have been researched. For example, the macromolecules of Xanthan gum solutions have been studied by means of flow birefringence(Chow & Fuller, 1984; Meyer et al., 1993; Smyth et al., 1995; Yevlampieva et al., 1999). Flow-induced birefringence measurements have also been linked to the stress in the material by the so-called stress-optical rule (Fuller, 1995a; Janeschitz-Kriegl, 1983). If this rule applies, birefringence is linearly proportional to the principal stress difference. Researchers apply the stress-optical rule to study the rheo-optical and structural behavior of fluids (Calabrese, Varchanis, et al., 2021; Ober et al., 2011).

Many flow visualization studies use Milling Yellow (Durelli & Norgard, 1972; Peebles et al., 1964; Rankin et al., 1989; Schneider, 2013; Y.-D. Sun et al., 1999), an industrial dye and a test fluid for simulating blood flows (Schmitz & Merzkirch, 1984). Other fluids have also been successfully investigated (Funfschilling & Li, 2001; Hu et al., 2009; Mackley & Hassell, 2011; Martyn et al., 2000; Tomlinson et al., 2006).

Cellulose nanocrystals (CNCs) are currently attracting much attention, and several potential applications are being explored and discussed (Habibi et al., 2010; Lagerwall et al., 2014). CNCs are rod-like particles and have birefringent optical properties (Parker et al., 2018). Aqueous cellulose suspensions have been reported to be birefringent when the crystals are aligned magnetically (Frka-Petesic et al., 2015), electrically (Bordel et al., 2006) or mechanically (Calabrese, Varchanis, et al., 2021; Chowdhury et al., 2017; Ebeling et al., 1999; Hausmann et al., 2018). In this study, velocity gradients in laminar flows cause mechanical alignment. Flow birefringence has been used to study the birefringence relaxation of CNCs (Tanaka et al., 2019). The complex strain-optical coefficient was

measured experimentally using a custom-built apparatus for oscillatory flow birefringence measurements (Tanaka et al., 2018) and was compared to theoretical values, for which the CNCs dimensions were measured by transmission electron microscopy. They concluded that birefringence relaxation is well-described by the theory for rigid rods and that flow birefringence is an efficient tool to determine the length distribution function of the CNCs. It was also noted that birefringence relaxation is less sensitive to internal motions such as tension and bending than to rotational motions.

In general, a birefringent fluid is characterized by two properties (Pindera & Krishnamurthy, 1978). The first is the relationship between shear rate $\dot{\gamma}$ and the magnitude of birefringence, expressed as $\Delta n(\dot{\gamma})$, where Δn is the difference between the main refractive indices n_1 and n_2. If we define n_1 as the refractive index associated with the fast axis, meaning $n_1 < n_2$, this gives $\Delta n = n_2 - n_1$. The second property refers to the orientation of the refractive index axes and is commonly described by the extinction angle $\chi(\dot{\gamma})$. In order to measure optical properties, various polarized light imaging techniques have been proposed. Common experimental techniques use specially designed flow channels (Calabrese, Haward, et al., 2021), plate-plate geometries (Hausmann et al., 2018; Mykhaylyk et al., 2016) or Taylor-Couette type settings (Cerf & Scheraga, 1952). The advantage of the latter is the straightforward identification of the extinction angle in the annular gap between the concentric cylinders. If two crossed linear polarizers are utilized in a Taylor-Couette type setting, one in front of the birefringent fluid and the other behind, an isoclinic cross appears, marking the orientation of the refractive index axes. The extinction angle is defined as the smaller of the two angles between the isoclinic cross and the linear polarizers. Possible values range between 0° and 45°.

If the refractive index of an ellipsoidal particle along the symmetry axis differs from the indices along the semi-axes, the optical response of one particle is similar to that of a uniaxial crystal with an extraordinary and an ordinary refractive index, n_e and n_0, respectively. A uniaxial crystal is said to be positive if $n_e > n_o$ and negative if $n_e < n_o$. For rod-like CNC particles, studies have reported $n_e > n_o$ (Frka-Petesic et al., 2015; Iyer et al., 1968; Klemm et al., 1998), making them optically positive. Peterlin (1938) and Peterlin and Stuart (1939a, 1939b) (in German) presented a three-dimensional distribution function of rigid rotational ellipsoidal particles in a laminar flow with a constant velocity gradient. Part of that theory was evaluated numerically (Cressely et al., 1985; Nakagaki & Heller, 1975; Scheraga et al., 1951). Peterlin and Stuart (1939a, 1939b) applied the hydrodynamic equations of motion based on the work by Jeffery (1922) and added a rotational diffusion coefficient D_r to model the effect of Brownian motion. They showed that the extinction angle is a result of the distribution function and argue that the fluid behaves like a biaxial crystal. If the ellipsoidal particles are aligned electrically or magnetically, the fluid behaves like a uniaxial crystal with the optical axis in the direction of alignment. In a flow with a constant velocity gradient (gradient perpendicular to the flow direction), the particles align in a preferential direction within the flow plane but the in-plane alignment distribution is different to the out-of-plane distribution, resulting in the biaxial crystal behavior (three different main refractive indices). Peterlin and Stuart (1939a, 1939b) did not take particle-particle interactions into account. Therefore, their theoretical findings are limited. However, their conclusion that a sheared fluid behaves like a biaxial crystal due to the three-dimensional distribution function is thought to be transferable. Due to the symmetric setting here, one main refractive index axis is perpendicular to the flow plane.

A single rod-like particle in a fluid flow with constant velocity gradient is primarily oriented as indicated in Fig. 6.1 (Calabrese, Haward, et al., 2021; Cerf & Scheraga, 1952; Mykhaylyk et al., 2016). The relation between alignment and rotational diffusion is described by the Péclet number $Pe = \dot{\gamma}/D_r$. Rotational diffusion is dominant when $Pe < 1$ whereas the velocity gradient dominates when $Pe > 1$. For $Pe \approx 1$, the rods start to align in a preferential orientation, causing the onset of shear thinning and birefringence. At small velocity gradients ($Pe \approx 1$) the preferred orientation of the rods is $\chi = 45°$ due to the hydrodynamic tensile and compression forces, which are at an angle of 45° to the direction of flow. With higher velocity gradients ($Pe \gg 1$), the longitudinal axis of the rods is increasingly parallel to the direction of flow, leading to $\chi \to 0°$ (Scheraga et al., 1951). For optically positive, rod-like particles, the extinction angle lies between the direction of flow and the slow refractive index axis n_2 ($n_2 > n_1$). This is because of the larger extraordinary optical index of the longitudinal axis of the particles $n_e > n_o$.

The intention of this study is to present streaming birefringence measurements of CNC water suspensions. Utilizing a Taylor-Couette type setting, the optical properties $\Delta n(\dot{\gamma})$ and $\chi(\dot{\gamma})$ are determined as functions of the shear rate. The results are of interest for two reasons. First, they help characterizing aqueous CNC suspensions and are therefore of interest to researchers studying the suspension physics. Second, the measurements indicate that these types of birefringent fluids can be used to visualize and study fluid flows and could present an alternative to current birefringent fluids.

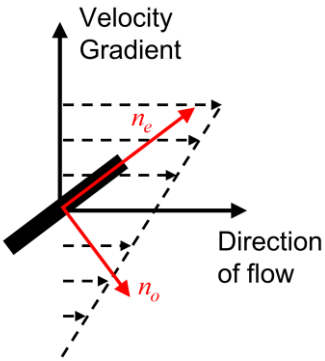

Fig. 6.1. Indicated position of an optically positive rod-like particle with $n_e > n_o$. Dotted lines represent the laminar velocity field with a constant gradient

6.2. Materials and methods

6.2.1. Material

Aqueous CNC suspensions were prepared by dispersing CelluForce NCC® powder (CelluForce Inc., www.celluforce.com) in distilled water. Jakubek et al. (2018) measured the average length and width of CelluForce CNC (spray dried) by transmission electron microscopy (87nm, 7.4nm; axial ratio ~11; longest reported length ~250nm) and atomic force microscopy (77nm, 3.5nm; axial ratio ~22, longest reported length ~200nm). Bertsch et al. (2018) also use atomic force microscopy and arrive at similar results (79nm, 4.8nm; axial ratio ~16; longest reported length ~400nm). Seven suspensions with different concentrations (weight percentage, wt%) CNC were studied: 0.7, 0.8, 0.9, 1.0, 1.1, 1.2, 1.3 wt%. The mixtures were allowed one week to settle before the experiments so that the nanocrystals could disperse homogeneously. The distilled water had a conductivity of <0.07 $\mu S/cm$ and the error in concentration is estimated to be $\Delta c = \pm 0.03 wt\%$.

6.2.2. Experimental setup

The experimental setup is shown in Fig. 6.2. It is the same apparatus as documented in Lane et al. (2021b) with only small modifications. Unpolarized light from a halogen bulb (150W EKE) is emitted through a 600nm bandpass filter (600FS10-50 from Andover Corporation, HBW 10nm). The light is then polarized by a linear polarizer (extinction ratio 10,000:1). The polarized light is collimated and redirected by a mirror upwards through a Taylor-Couette flow cell. The linear polarizer was placed in such a way that the light is fully p-polarized (electric field in the plane of incidence on the mirror). The Taylor-Couette experiment consists of a feedback-controlled DC motor with a tachometer and a 415:1 reduction gear rotating the inner cylinder at a selected angular velocity Ω, two glass windows at top and bottom enabling optical access and an outer cylinder sealing the setup. The height of the inner cylinder is 25mm and the radius $r_{inner} = 48mm$. The inner radius of the outer cylinder is $r_{outer} = 49.5mm$, resulting in a gap width of 1.5mm. The shear rate in a Taylor-Couette flow can be derived from (Davey, 1962) and is given as

$$|\dot{\gamma}(r)| = \frac{2 \cdot \Omega}{r^2} \cdot \frac{r_{inner}^2 \cdot r_{outer}^2}{r_{outer}^2 - r_{inner}^2} . \tag{6.1}$$

We approximate the close to constant shear rate with the shear rate in the middle of the gap $\dot{\gamma}(r_{middle})$, where $r_{middle} = (r_{inner} + r_{outer})/2$. The relative difference between inner and outer shear rate is

$$\frac{|\dot{\gamma}(r_{inner}) - \dot{\gamma}(r_{outer})|}{|\dot{\gamma}(r_{middle})|} = \frac{(r_{outer}^2 - r_{inner}^2) \cdot (r_{inner} + r_{outer})^2}{4 \cdot r_{inner}^2 \cdot r_{outer}^2} \approx 6\% . \tag{6.2}$$

With this design, shear rates between 0-31 1/s were tested. A monochrome polarization camera (Lucid Vision Labs Phoenix PHX050S-P, Nikon Nikkor 35-70mm 1:3.3-4.5, applied f-number: f/3.3) placed above the setup measured the optical response. The default gain setting was used, and the exposure time was set to ensure a dynamic range of about 70%. The camera was not calibrated, as measurement errors are estimated to remain below 4% for this setting (Lane, Rode, et al., 2022a).

Using a linear polarizer has the advantage that phase differences up to π radians can be measured. However, only the relative positions of the refractive index axes can be determined, and no distinction between fast axis and slow axis is possible.

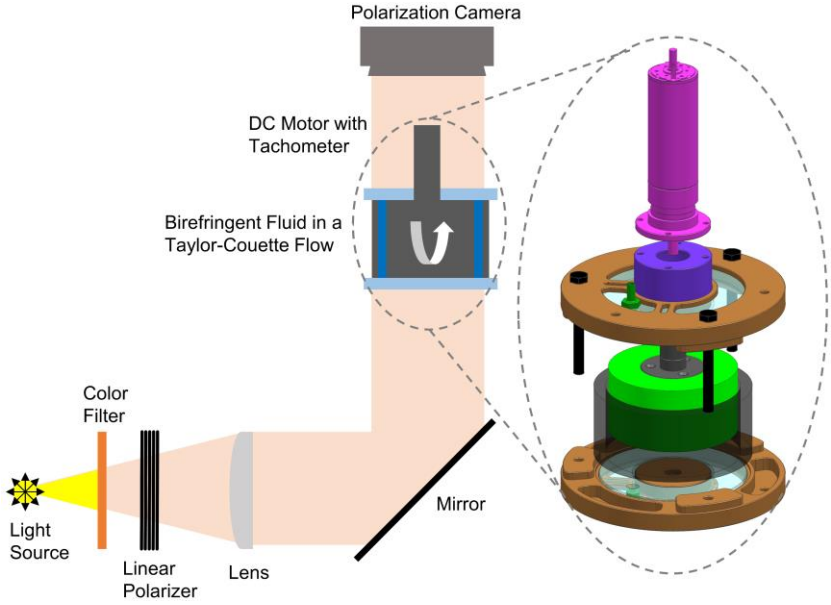

Fig. 6.2. Experimental setup of the Taylor-Couette flow. Light from a light source is color filtered (600nm), polarized and directed through the Taylor-Couette flow. A polarization camera measures the optical response in the gap. The figure is adapted from Lane et al. (2021b).

6.2.3. Optical characterization

The polarization camera used in this study is a division-of-focal-plane polarimeter that features small polarizers on every pixel. The polarizers have the directions 0°, 45°, 90°, 135° and vary in a regular pattern. The measured light intensities passing the corresponding polarizers are referred to as $I_0, I_{45}, I_{90}, I_{135}$. These intensities give the first three of the four Stokes parameters,

$$\begin{aligned} S_0 &= \frac{I_0 + I_{45} + I_{90} + I_{135}}{2} \\ S_1 &= I_0 - I_{90} \\ S_2 &= I_{45} - I_{135}. \end{aligned} \tag{6.3}$$

A polarization camera is therefore able to measure the Stokes parameters in Eq. (6.3) with a single snapshot. If light is only partially polarized, meaning that the light is composed of a polarized part and an unpolarized part, the fully polarized part can be expressed with the help of the degree of polarization ($DOP \leq 1$). Applying the DOP and normalizing the Stokes parameters by S_0 results in two normalized expressions for the fully polarized part of the light (Chipman, 1994):

$$\begin{aligned} S_{1_{N,P}} &= \frac{S_1}{DOP \cdot S_0} \\ S_{2_{N,P}} &= \frac{S_2}{DOP \cdot S_0}. \end{aligned} \tag{6.4}$$

The DOP in the experiments was typically between 90-95%. By linking Stokes parameters to the birefringent properties of the flow, it is possible to optically characterize the fluid. The suspension is sheared due to the rotating inner cylinder and therefore becomes birefringent. The axis n_2 is located at an angle α, and

the extinction angle χ describes the relative position between axis n_2 and flow direction. The situation is schematically shown in Fig. 6.3. The drawing outlines the relation between extinction angle χ, angular coordinate ϕ and absolute position α of the slow axis n_2:

$$\alpha = \phi + \chi \,. \tag{6.5}$$

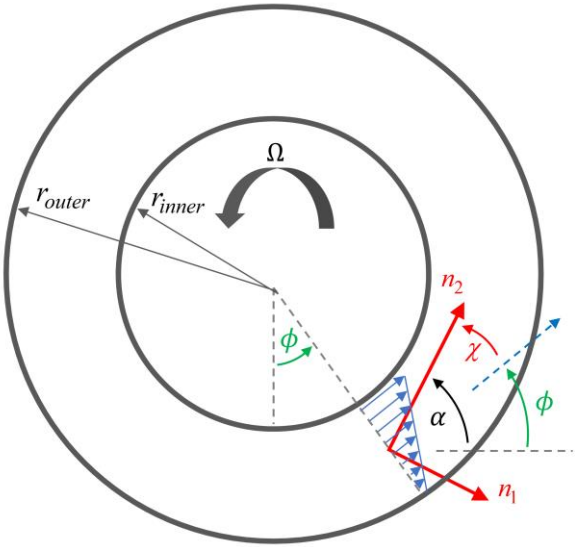

Fig. 6.3. Relation between extinction angle χ, angular coordinate ϕ and absolute position of the optical axes α.

The Mueller matrix in Lane et al. (2021b) relates χ to the fast axis, which would be n_1 in our case. However, as the method cannot distinguish between fast and slow axis, we relate χ directly to n_2, the correct reference axis. To make sure

that this axis is the slower axis, we used a circular polarizer and analyzed the results following the theory described by Onuma and Otani (2014). This approach distinguishes fast and slow axis but can only measure phase differences up to $\pi/2$ radians. The measurements were not used to quantify the optical properties but to determine the position of the fast and slow refractive index axes. The measurements confirmed that fast and slow axis are indeed located as indicated in Fig. 6.3. (It is worth mentioning that the mirror reverses the direction of circular polarization. Left-handed circularly polarized light is therefore right-handed circularly polarized after reflection. Also, if right-handed circular polarized light undergoes a phase shift of π, it is left-handed circular polarized and the equations require a proper adaptation). The relationship between phase differences δ and difference of the refractive indices is given as:

$$\Delta n = \frac{\lambda}{2\pi L}\delta \,. \tag{6.6}$$

Here, λ is the wavelength of the light (600nm) and L the optical path length, equaling the height of the inner rotating cylinder (25mm).

We use the measurement technique described in a previous study (Lane et al., 2021b) to characterize the birefringent fluid. At each position ϕ, the polarization camera records the intensities $I_0(\phi), I_{45}(\phi), I_{90}(\phi), I_{135}(\phi)$. The degree of polarization for each location is estimated when the fluid is at rest, hence not being birefringent:

$$DOP(\phi) = \frac{\sqrt{S_{1,rest}^2(\phi) + S_{2,rest}^2(\phi)}}{S_{0,rest}(\phi)} \,. \tag{6.7}$$

With Eq. (6.3) and Eq. (6.7), the normalized expressions in Eq. (6.4) can be measured at every position ϕ, giving $S_{1_{N,P}}(\phi)$ and $S_{2_{N,P}}(\phi)$. If we assume that the birefringent fluid can be approximated as a linear retarder with δ being the phase difference and α the position of an axis, theoretical expressions for the normalized Stokes parameters $S_{1_{N,P}}$ and $S_{2_{N,P}}$ are obtained by applying Mueller calculus. If the linear polarizer in Fig. 6.2 is in line and hence parallel to the I_0 direction of the polarization camera, the normalized Stokes parameters resulting from Mueller calculus are:

$$\begin{aligned} S_{1_{N,P}}(\phi) &= 1-\frac{1}{2}(1-\cos[4(\phi+\chi)])(1-\cos\delta) \\ S_{2_{N,P}}(\phi) &= \frac{1}{2}\sin[(4(\phi+\chi)](1-\cos\delta). \end{aligned} \tag{6.8}$$

Measuring $S_{1_{N,P}}(\phi)$ and $S_{2_{N,P}}(\phi)$ as functions of the angular coordinate and fitting Eq. (6.8) to the measured distributions gives estimates for the extinction angle χ and the phase difference δ. The distributions in Eq. (6.8) are periodic with period $\pi/2$ in χ and therefore the resulting extinction angle remains in the range between [0°,90°]. For this reason, the distributions in Eq. (6.8) cannot distinguish between fast and slow axis. The results for the phase difference δ using Eq. (6.8) are within the range $[0,\pi]$. Fig. 6.4 (a) and (b) show sample measurements of the Stokes parameters as function of the polar coordinate ϕ and the correspondingly fitted distributions. In total, 200 measurement points with ϕ varying between [-3°,154°] were analyzed. From the fits, parameters χ and δ are determined. Without any further information, it cannot be determined if the result for δ is within the range $[0,\pi]$ or within $[\pi, 2\pi]$. At the beginning of a

measurement, the fluid is at rest and no birefringence occurs, corresponding to $\delta = 0$. If the shear rate is increased by small enough steps, the measured phase differences that lie between $[0, \pi]$ can be unwrapped to higher intervals. For example, the measurements $[0, \pi/2, \pi, \pi/2, 0, \pi/2, \pi]$ correspond to $[0, \pi/2, \pi, 3\pi/2, 2\pi, 5\pi/2, 3\pi]$. With the unwrapping procedure, birefringence of multiple order retardance can be determined. This can be seen in Fig. 6.4 (c) where the measured phase differences δ are expanded to higher values. The measurement error resulting from the fitting procedure is discussed by Lane et al. (2021b). For phase differences close to $\delta = 0, 2\pi, \ldots$, the measurement error for the extinction angle χ is high. This becomes obvious when comparing Fig. 6.4 (a) and Fig. 6.4 (b). The accuracy of the χ measurements for the periodic distributions in Fig. 6.4 (a) is significantly larger compared to the distributions shown in Fig. 6.4 (b). The reason for this is found in Eq. (6.8), indicating that the amplitude of the distributions is directly linked to the phase difference δ. If δ is below a certain limit, we therefore neglect the corresponding χ measurement. In this study, a limit of $\delta \geq \pi/4$ was chosen for which the measured extinction angles χ are considered valid. Finally, we would like to note that the fitting of δ appeared more robust compared to the fitting of χ. Many measurement points showed a strong discontinuity for χ at $\delta = 0, 2\pi, \ldots$. The CNC suspensions are strongly birefringent, and we assume that an unwanted re-alignment of the fluid at the top and bottom surfaces of the cylinder gap disturbs the measurements of χ. The optical influence of the unwanted alignment seems minimal in areas where the gap is parallel or perpendicular to the linear polarization of the incident light. Therefore, the presented measurements of χ were obtained by only considering the 20 measurement points for which ϕ is within [-3°,5°] or

[86°,94°]. For δ however, all 200 measurement points were used, as depicted in Fig. 6.4.

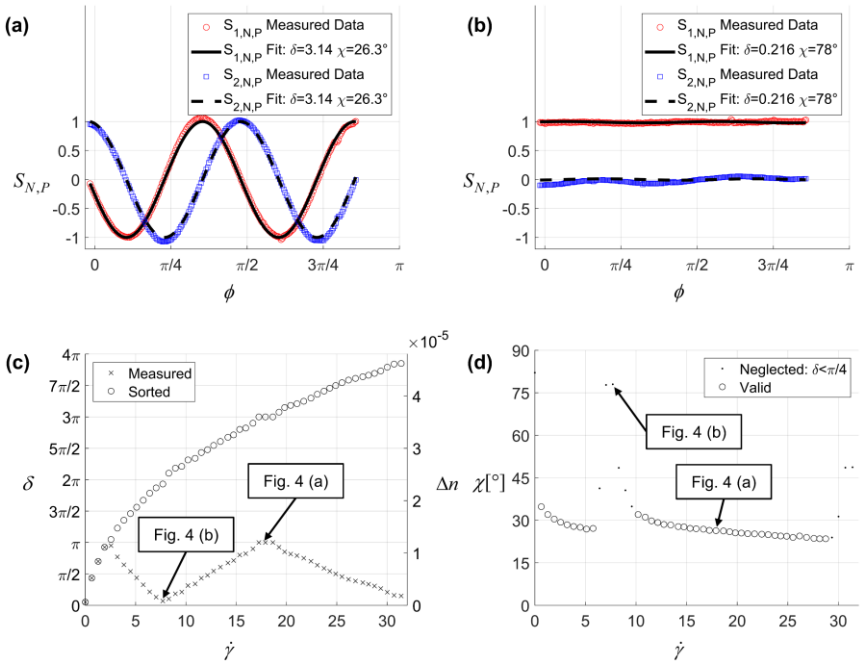

Fig. 6.4. Birefringence measurements with a linear polarizer. Suspension: 1.3 wt% CNC. **(a)** and **(b)** Results obtained by fitting Eq. (6.8) to the measured distributions of Eq. (6.4) are shown in (a) for $\dot{\gamma} = 17.6$ and (b) for $\dot{\gamma} = 7.6$. **(c)** The fitted results for δ are between $[0, \pi]$, sorting them according to the periodic nature gives the correct phase difference. Birefringence Δn is calculated with Eq. (6.6). **(d)** Measurement results for the extinction angle χ using the measurement points for which ϕ is between [-3°,5°] or [86°,94°].

6.2.4. Experimental procedure

Fifty different shear rates between 0-31 1/s were studied. Fig. 6.4 shows the result for the suspension with 1.3 wt%. The first measurement was done at rest. After

each stepwise increase, the shear rate was kept steady for five seconds before recording ten images and averaging them. From the mean image the corresponding parameters δ, χ were derived. Phase differences were sorted following the procedure depicted in Fig. 6.4 (c). The relationship between birefringence Δn, shear rate $\dot{\gamma}$, and mass fraction $w = w_{CNC} / w_{total}$ is modeled as:

$$\Delta n = (A \cdot \dot{\gamma})^n \cdot w^m . \tag{6.9}$$

6.3. Results and discussion

Measurement results for the extinction angle χ are shown in Fig. 6.5 (a) and are given in Table 6.1 in the appendix. All measurements that are considered valid (compare Fig. 6.4 for the distinction between valid and non-valid measurements) are within 23-40°. Increasing the shear rate tends to decrease the extinction angle, which is in line with common theory as discussed in the introduction. For all suspensions most of the decrease can be seen between 0-5 1/s. After 5 1/s, the extinction angle decreases rather slowly. We explain outliers such as the 35° measurement for 1.0 wt% at a shear rate of 24.9 1/s with measurement limitations and its uncertainties. Birefringence measurements Δn are shown in Fig. 6.5 (b), (c) and (d). The values can be looked up in Table 6.2 in the appendix. It is important to note that measurement errors of δ are high for phase differences close to $\delta = 0, \pi, 2\pi$ (Lane et al., 2021b). The non-zero values at zero shear rate in Table 6.2 are therefore thought to result from measurement inaccuracies. Eq. (6.9) was fitted to the measurements and the result is plotted for comparison. The determined parameters are A=0.1070 s, n =0.537 and m=2.445, giving a root-mean-square-error of 9e-7. Fig. 6.5 (d) shows the measurements and the fit in a base-10 logarithmic scale for the shear rates. We can see that the fit is working

particularly well for the 1.1 wt% and 1.3 wt% suspension. Increasing the shear rate generally increases birefringence. The increase in birefringence per shear rate decreases for higher shear rates as the slope decreases. A rather sharp increase at low shear rates and a levelling off at higher velocity gradients has been similarly found for Xanthan gum solutions (Chow & Fuller, 1984; Lane et al., 2021b). Birefringence of Milling Yellow suspensions has been reported to be proportional to the shear rate at low shear rates but also shows a levelling off at higher shear rates (Peebles et al., 1964). The studied CNC suspensions display birefringence of magnitude 1e-5 and are in the same order as Xanthan gum (Lane et al., 2021b) and Milling Yellow (Peebles et al., 1964). Hence CNC suspensions appear as an attractive alternative for flow visualization studies due to their stability, ease of preparation and low cost.

The critical concentration for interparticle interactions of aqueous CNC is reported to be 0.5 wt% and the critical volume fraction for the isotropic cholesteric phase transition is at about 3-4 wt% (Bertsch et al., 2019). Below a concentration of 0.5 wt%, CNCs are assumed to be isotropically oriented. Above 0.5 wt%, cholesteric tactoids are formed. The suspensions in this study are above 0.5 wt% and we hence expect interparticle interactions.

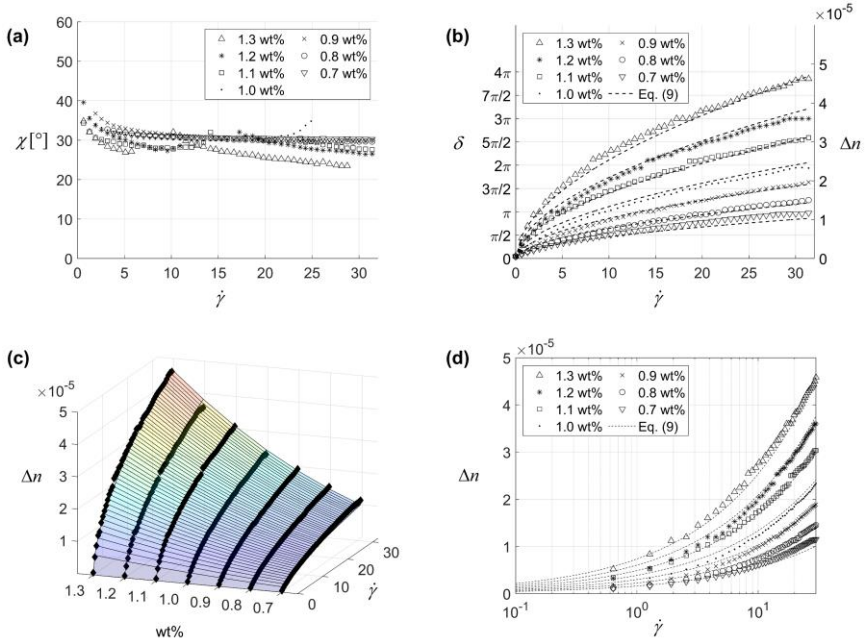

Fig. 6.5. Steady state response as function of mass fraction and shear rate. **(a)** Extinction angle measurements. **(b)** Birefringence Δn measurements and fitted Eq. (6.9) with A=0.1070 s, n=0.537, m=2.445 and a root-mean-square-error of 9e-7. **(c)** Measurement points and surface plot of Eq. (6.9). **(d)** Birefringence Δn measurements and fitted Eq. (6.9) in a base-10 logarithmic scale for the shear rates.

It was stated in the introduction that the relation between shear alignment and rotational diffusion is described by the Péclet number $Pe = \dot{\gamma}/D_r$. The rotational diffusion coefficient D_r for interacting rods decreases with increasing rod concentration (Doi & Edwards, 1978; Maguire et al., 1980; Teraoka & Hayakawa, 1989). This is because the rotational motion of a rod is increasingly restricted by its neighbors (Tao et al., 2005). Therefore, the required shear rate for the onset of particle alignment decreases with increasing concentration. It can be seen in Fig.

6.5 (d) that the birefringence data seems to shift to the left with increasing concentration, which is in line with the theory. Shafiei-Sabet et al. (2012) report rheology measurements of aqueous CNC suspensions. Their 1 wt% CNC suspension is thought to be comparable to the suspensions used in this study (CNC powder dispersed in distilled water; average length: 100nm, average width: 7nm). The steady-state shear viscosity measurements for the 1wt% suspension show a Newtonian plateau at low shear rates ($< \sim 10^{-2}\,1/s$), a shear thinning region at intermediate shear rates ($\sim 10^{-2}\,1/s - \sim 10^{0}\,1/s$); and a second plateau at higher shear rates. The onset of shear thinning is related to the onset of shear alignment ($Pe \approx 1$), and the shear rate corresponding to the onset of shear thinning can be taken as an estimate for the rotational diffusion coefficient (Corona et al., 2018). We therefore assume that all our measurements (except at zero shear rate) are taken in the shear aligned regime.

As expected, increasing the amount of CNC increases the birefringence response. Calabrese et al. (Calabrese, Haward, et al., 2021) studied the birefringence of a 0.1 wt% CNC dispersion that had been similarly prepared (CNC purchased from CelluForce, diluted in deionized water). However, they purchased an aqueous dispersion (never-dried) from CelluForce whereas this study uses re-suspended CNC powder. The CNC dimensions reported by Calabrese et al. (Calabrese, Haward, et al., 2021) are: average length 260nm; average diameter 4.8nm; aspect ratio ~54; longest reported length ~700nm. Shear induced birefringence is reported to be $\Delta n \approx 3 \cdot 10^{-6}$ ($\dot{\gamma} \approx 100\,1/s$) and $\Delta n \approx 9 \cdot 10^{-6}$ ($\dot{\gamma} \approx 400\,1/s$). Compared to these values our birefringence results are much higher. This is plausible as we are using much higher CNC concentrations. For shear rates below 40 1/s the fluid from Calabrese et al. (Calabrese, Haward, et al., 2021) is considered isotropic ($\Delta n = 0$). The onset of shear alignment and therefore equally

the rotational diffusion ($Pe \approx 1$) is reported to be 40 1/s. The authors propose a proportionality of $\Delta n \sim \dot{\gamma}^{0.9}$. The exponent 0.9 is significantly different to our result, 0.537. We consider several possible reasons for this difference. Calabrese et al. (Calabrese, Haward, et al., 2021) are using a CNC suspension in the dilute regime and the relation between rotational diffusion coefficient D_{r0} (no particle interaction) and rod length is given as $D_{r0} \sim l^{-3}$ (Doi & Edwards, 1978). The suspensions in this study are thought to be above the dilute regime and hence particle interactions have to be considered. According to Maguire et al. (1980) the rotational diffusion coefficient for interacting rods is concentration and rod length dependent, giving $D_r \sim c^{-2} l^{-9}$. Our different exponent could therefore be explained by a different particle interaction behavior due to the different concentrations and the shorter rod lengths. The morphological properties are dependent on the drying method (Peng et al., 2012) and this might also explain the difference.

Calabrese et al. (Calabrese, Haward, et al., 2021) report that extensional forces, described by the extensional rate $\dot{\varepsilon}$, are four times more effective in aligning CNCs than shear forces, stating $\Delta n \sim \dot{\gamma}^{0.9} \sim (4 \cdot \dot{\varepsilon})^{0.9}$. As we only study shear forces in the Taylor-Couette flow this aspect has not been researched and it is not clear if the factor 4 is transferable to our suspensions.

6.4. Appendix

Table 6.1. Extinction angle data as plotted in Fig. 6.5 (a). Note that the fields marked with (-) are empty due to measurement limitations when $\delta < \pi/4$ (Compare Fig. 11 (b) in (Lane et al., 2021b)).

Shear Rate [1/s]	Extinction angle χ [°]						
	0.7 wt%	0.8 wt%	0.9 wt%	1.0 wt%	1.1 wt%	1.2 wt%	1.3 wt%
0.0	-	-	-	-	-	-	-
0.6	-	-	-	-	34.3	39.6	34.8
1.3	-	-	-	35.9	32.1	35.5	32.1
1.9	-	-	36.8	34.1	30.7	33.8	30.4
2.6	-	-	35.4	33.2	30.2	32.6	29.3
3.2	-	32.7	34.4	32.6	29.8	31.7	28.4
3.8	31.8	32.4	33.7	32.2	29.7	31.0	27.8
4.5	31.6	32.2	33.4	31.8	29.1	30.4	27.5
5.1	31.5	32.0	33.0	31.5	29.0	30.0	26.9
5.8	31.4	31.7	32.7	31.2	28.7	29.5	27.1
6.4	31.3	31.4	32.4	31.0	28.5	29.0	-
7.0	31.1	31.3	32.2	30.9	28.7	28.6	-
7.7	31.1	31.2	31.9	30.7	28.1	28.2	-
8.3	31.0	31.1	31.8	30.6	28.0	27.6	-
9.0	31.0	31.0	31.6	30.5	28.0	28.0	-
9.6	31.0	30.9	31.5	30.4	28.1	27.3	-
10.2	30.9	30.8	31.3	30.3	27.8	27.9	32.0
10.9	30.9	30.7	31.2	30.2	28.2	28.5	31.1
11.5	30.9	30.6	31.1	30.0	28.2	-	29.8
12.1	30.8	30.6	31.0	30.2	28.1	-	29.2
12.8	30.7	30.5	31.0	30.0	29.0	-	28.5
13.4	30.7	30.4	30.8	30.0	29.4	-	28.4
14.2	30.7	30.5	30.8	30.0	32.0	-	27.8

14.7	30.6	30.5	30.5	29.9	-	-	27.7
15.3	30.7	30.4	30.5	30.0	-	-	27.2
15.9	30.6	30.3	30.4	30.1	-	-	27.0
16.7	30.6	30.2	30.3	30.1	-	-	26.9
17.3	30.6	30.1	30.3	29.9	-	32.0	26.5
17.9	30.6	30.1	30.2	29.8	-	31.1	26.3
18.6	30.5	30.1	30.1	30.1	-	31.0	26.3
19.3	30.5	30.0	30.1	30.1	-	30.5	26.0
19.8	30.5	30.0	30.0	30.2	-	29.8	25.6
20.4	30.5	30.0	30.0	30.6	-	29.3	25.5
21.0	30.4	29.9	29.9	30.7	-	29.3	25.3
21.7	30.5	29.9	29.8	31.1	-	29.0	25.2
22.4	30.4	29.9	29.8	31.2	-	28.8	25.1
23.1	30.4	29.8	29.7	31.6	-	28.5	24.9
23.7	30.4	29.8	29.8	32.5	30.5	28.2	24.7
24.3	30.4	29.8	29.7	33.7	29.5	28.0	24.5
24.9	30.4	29.8	29.7	34.8	29.6	27.8	24.4
25.5	30.4	29.8	29.6	-	29.3	27.6	24.0
26.2	30.5	29.7	29.7	-	28.8	27.4	24.5
26.9	30.3	29.7	29.6	-	28.6	27.5	24.0
27.6	30.3	29.7	29.6	-	28.3	27.3	23.6
28.2	30.3	29.6	29.7	-	28.3	27.3	23.5
28.7	30.4	29.7	30.1	-	28.0	27.1	23.5
29.4	30.3	29.6	29.8	-	28.0	26.9	-
30.0	30.3	29.7	29.8	-	27.7	26.7	-
30.7	30.3	29.7	29.8	-	27.7	26.4	-
31.4	30.2	29.6	30.0	-	27.6	26.5	-

Table 6.2. Birefringence data as plotted in Fig. 6.5 (b) and (c). Note that the values in brackets have been obtained within $\pm\pi/16$ of $\delta \approx 0, \pi$ and are therefore thought to be potentially affected by measurement uncertainties (Compare Fig. 11 (a) in (Lane et al., 2021b)). These measurement inaccuracies are thought to be the main reason for the non-zero values at zero shear rate.

Shear Rate [1/s]	Birefringence $\Delta n \cdot 10^5$						
	0.7 wt%	0.8 wt%	0.9 wt%	1.0 wt%	1.1 wt%	1.2 wt%	1.3 wt%
0.0	(0.05)	(0.05)	(0.06)	(0.06)	(0.06)	(0.07)	(0.07)
0.6	0.11	0.12	0.16	0.20	0.34	0.33	0.52
1.3	0.16	0.18	0.24	0.33	0.53	0.54	0.84
1.9	0.21	0.24	0.32	0.42	0.67	0.72	1.12
2.6	0.25	0.29	0.39	0.52	0.81	0.89	(1.20)
3.2	0.29	0.35	0.45	0.60	0.94	1.03	1.45
3.8	0.33	0.40	0.51	0.67	1.03	(1.20)	1.60
4.5	0.36	0.44	0.58	0.75	(1.16)	(1.20)	1.74
5.1	0.40	0.48	0.63	0.81	(1.20)	1.28	1.88
5.8	0.42	0.51	0.68	0.89	(1.27)	1.43	2.01
6.4	0.45	0.55	0.73	0.94	1.34	1.53	2.16
7.0	0.49	0.60	0.78	1.00	1.43	1.61	2.25
7.7	0.52	0.63	0.83	1.07	1.51	1.70	2.32
8.3	0.54	0.65	0.86	(1.13)	1.58	1.81	2.55
9.0	0.57	0.70	0.92	(1.16)	1.62	1.86	2.61
9.6	0.60	0.72	0.96	(1.20)	1.71	1.93	2.67
10.2	0.61	0.75	0.99	(1.24)	1.75	2.04	2.78
10.9	0.65	0.79	1.04	1.29	1.82	2.08	2.81
11.5	0.66	0.81	1.07	1.35	1.87	2.18	2.93
12.1	0.69	0.85	(1.13)	1.38	1.92	2.22	2.98
12.8	0.71	0.86	(1.15)	1.44	1.97	(2.32)	3.07
13.4	0.74	0.90	(1.20)	1.47	2.03	(2.33)	3.13
14.2	0.75	0.92	(1.20)	1.52	2.07	2.53	3.24

14.7	0.78	0.96	(1.21)	1.55	2.13	2.54	3.26
15.3	0.79	0.97	(1.27)	1.59	2.15	2.61	3.37
15.9	0.81	0.99	1.29	1.65	2.23	2.66	3.41
16.7	0.84	1.03	1.35	1.66	2.26	2.67	3.48
17.3	0.85	1.05	1.36	1.70	2.29	2.76	(3.60)
17.9	0.87	1.07	1.39	1.76	(2.32)	2.80	(3.60)
18.6	0.90	1.10	1.44	1.78	2.50	2.81	(3.60)
19.3	0.91	(1.13)	1.47	1.79	2.50	2.88	3.68
19.8	0.93	(1.13)	1.48	1.84	2.53	2.95	3.79
20.4	0.94	(1.13)	1.50	1.89	2.57	3.00	3.84
21.0	0.96	(1.17)	1.54	1.92	2.61	3.02	3.86
21.7	0.98	(1.18)	1.58	1.94	2.64	3.06	3.90
22.4	1.01	(1.25)	1.62	1.97	2.66	3.11	3.96
23.1	1.02	(1.27)	1.63	2.00	2.69	3.15	4.02
23.7	1.03	1.29	1.67	2.02	2.71	3.21	4.09
24.3	1.05	1.30	1.69	2.05	2.73	3.27	4.15
24.9	1.06	1.32	1.71	2.08	2.78	3.31	4.21
25.5	1.08	1.34	1.73	2.11	2.81	3.36	4.25
26.2	1.09	1.36	1.76	2.14	2.85	3.40	4.30
26.9	1.11	1.38	1.79	2.16	2.88	3.42	4.33
27.6	1.12	1.40	1.82	2.20	2.92	3.47	4.37
28.2	(1.14)	1.41	1.84	2.23	2.97	3.49	4.40
28.7	(1.14)	1.42	1.86	2.27	3.00	3.57	(4.44)
29.4	(1.15)	1.43	1.87	2.30	3.03	3.60	(4.50)
30.0	(1.15)	1.45	1.89	(2.34)	3.04	3.60	(4.58)
30.7	(1.15)	1.48	1.93	(2.34)	3.05	3.60	(4.63)
31.4	(1.17)	1.50	1.96	(2.33)	3.11	3.60	(4.62)

7. Shear rate imaging using a polarization camera and a birefringent aqueous cellulose nanocrystal suspension

The content of this chapter has been excepted for publication at the *20th international symposium on applications of laser and imaging techniques to fluid mechanics, 11-14 July 2022, Lisbon, Portugal* (Lane, Baumann, et al., 2022):

Lane, C., Baumann, F., & Rösgen, T. (2022). Shear rate imaging using a polarization camera and a birefringent aqueous cellulose nanocrystal suspension. *20th International Symposium on Applications of Laser and Imaging Techniques to Fluid Mechanics, Lisbon, Portugal*, forthcoming.

Author contribution statements:

Connor Lane developed the theory, designed the experimental setup, analysed the data, and wrote the manuscript. In the scope of his master thesis, Frédéric Baumann helped design the flow channel, and proved the feasibility of the measurement technique as it stands. Thomas Rösgen developed the camera software and directed the project. All authors discussed the results and helped formulate the manuscript.

Note:

The following refers to the accepted version of the paper. This version may differ from the final published version. Please refer to the original paper for the typeset version. The citation style and the numbering of the figures and equations have been aligned to this document and are therefore changed.

Abstract

Two aqueous cellulose nanocrystal suspensions are used to experimentally measure the shear and strain rates in a two-dimensional fluid flow. Cellulose nanocrystals are rod-like particles that align when subjected to shear, whereas at rest, they are randomly orientated by Brownian motion. The alignment causes birefringence, a phenomenon also known as flow-induced birefringence. The amount of birefringence is measured using a rotatable linear polarizer and a polarization camera. The linear polarizer is rotated to nine different positions. At each position, light from a light source becomes linear polarized before entering the birefringent fluid. Because of the birefringence the state of polarization is changed. This change is measured by the polarization camera. From the nine measurements the two-dimensional birefringence distribution is determined and from the amount of birefringence the strain rate is derived with the help of the data published by Lane et al. (2022b). We define Λ_0 as the angle between the (maximum) strain rate and the direction of flow. A shearing flow leads to $\Lambda_0 = 45°$, whereas $\Lambda_0 = 0°$ and $\Lambda_0 = 90°$ describe a flow down the centerline of a symmetrically converging and diverging channel, respectively. The measured strain rates are compared to simulations. The reference data in (Lane, Rode, et al., 2022b) was taken at $\Lambda_0 = 45°$. For $\Lambda_0 \approx 45°$, measurements and simulations correspond well to each other. If $\Lambda_0 \approx 0°$ is assumed, measured strain rates appear too high whereas they are too low for $\Lambda_0 \approx 90°$. These results may be of interest for two reasons. First, shear rate imaging gave satisfying results in areas where $\Lambda_0 \approx 45°$. Therefore, we propose the study of shear rates in a two-dimensional shearing flow by means of the presented method. Second, the results indicate that the flow state affects the degree of particle alignment and thus birefringence. This finding is in line with the statements made by Wayland (1960, 1964). The study of particle alignment and its influencing factors is of interest, and the

experimental approach presented here is thought to be practicable for such studies.

Keywords: Shear Birefringence, Cellulose Nanocrystals, Polarization Camera

7.1. Introduction

Some types of birefringent fluids are composed of suspended anisotropic particles (Merzkirch, 2001). At rest, Brownian motion randomly orientates these particles, and the birefringent fluid is optically isotropic. Local velocity gradients align the particles and, as a result, the fluid becomes optically anisotropic. This phenomenon is also referred to as flow-induced birefringence and can be used to visualize and study fluid flows (Hu et al., 2009; Pih, 1980; Rankin et al., 1989) as well as to assess particle alignment and rheological properties (Fuller, 1995a; Janeschitz-Kriegl, 1983). The amount of birefringence is expressed by the difference between the two main refractive indices, Δn. Generally, Δn is a function of the shear rate $\dot{\gamma}$, where increasing $\dot{\gamma}$ increases Δn. Various experimental methods have been applied to determine $\Delta n(\dot{\gamma})$ and therefore to characterize a birefringent fluid (Calabrese, Haward, et al., 2021; Lane et al., 2021b; Mykhaylyk et al., 2016).

Many flow birefringence studies use an industrial dye called Milling Yellow (Peebles et al., 1964; Schneider, 2013; Y.-D. Sun et al., 1999). However other fluids such as solutions of tobacco mosaic virus have also been used (Hu et al., 2009). Cellulose nanocrystals (CNCs) are rod-like particles, and the refractive index of their longitudinal axis is larger than the refractive index of the semi-axes (Frka-Petesic et al., 2015). A recent study reports birefringence measurements of aqueous CNC suspensions and suggests their use in flow birefringence studies (Lane, Rode, et al., 2022b).

In this study the birefringence response Δn of aqueous CNC suspensions in a two-dimensional flow is measured with a polarization camera and the corresponding shear rates are derived by applying the data from Lane et al. (2022b). By comparing the measurements to analytical solutions as well as simulations, we confirm the results from Lane et al. (2022b) and show that aqueous CNC suspensions are promising birefringent fluids for shear rate imaging.

7.2. Material and methods

7.2.1. Experimental set-up

The experimental set-up is shown in Fig. 7.1. It consists of a light source (halogen bulb; 150W EKE) and a color filter (600nm bandpass filter; 600FS10-50 from Andover Corporation, HBW 10nm). The light is polarized by a rotatable linear polarizer (Techspec Glass polarizer 50.8 m; Edmund Optics Inc #66-183; extinction ratio 10,000:1) which is placed in a continuous manual rotation mount (Thorlabs Part RSP2/M). The light then travels through the birefringent fluid flow and is finally captured by a polarization camera (Phoenix PHX050S-P, Lucid Vision Labs (LUCID Vision Labs, 2022)) which is equipped with a high resolution telecentric lens (TC4MHR036-C from Opto Engineering; working f/#: 30). Polarization measurement errors from the polarization camera are estimated to be below 3% due to the sufficiently large f-number (Lane, Rode, et al., 2022a).

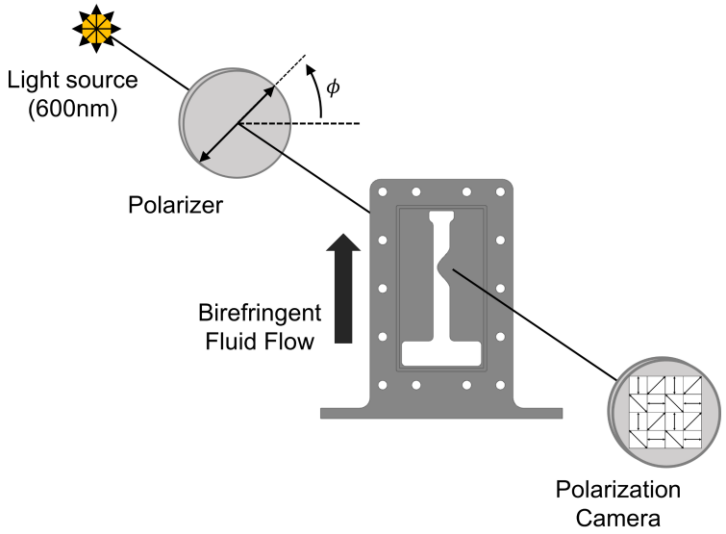

Fig. 7.1. Experimental set-up.

The flow channel was prepared using an additive manufacturing technique (3D Printer: Form3 from Formlabs; Material: Clear Resin). The channel dimensions can be seen in Fig. 7.2 (a). The cosine shaped constriction is described as:

$$y = 3\text{mm} + 3\text{mm} \cdot \cos\left[\frac{x}{10\text{mm}} \cdot \pi\right] \quad \text{for } -10\text{mm} \le x \le 10\text{mm}\,. \qquad (7.1)$$

Except for the constriction, the channel is 8mm wide and has a depth of 25mm. The flow direction is upwards. The main 3D printed part is shown in Fig. 7.2 (b). The front and back surfaces were milled in order to create plane surfaces. Additionally, a sealing groove was machined into each surface. Two glass plates level with the surfaces sealed the flow channel.

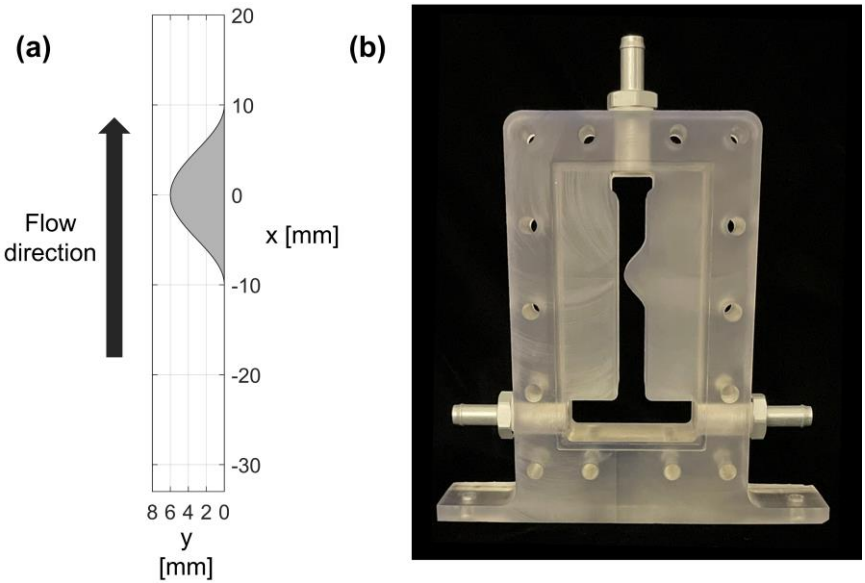

Fig. 7.2. (a) Flow channel dimensions and (b) 3D printed part

7.2.2. Two-dimensional birefringence measurements

We apply the measurement technique described in (Lane et al., 2021a). The linear polarizer is rotated to nine different positions: $\phi = 0° + 20° \cdot N$ with $N = 1,2, \dots, 9$. At each position, the light transmitted through the birefringent flow is captured by the polarization camera. The polarization camera measures the state of linear polarization. From the nine measurements, the relative phase difference δ is calculated, from which the birefringence is determined:

$$\Delta n = \frac{\lambda}{2\pi \cdot L} \delta \,. \tag{7.2}$$

Here, L=25 mm is the path length and λ the wavelength (600nm). Equation (7.2) requires that the optical properties are constant along the path length. We assume

an essentially two-dimensional flow due to the width / depth aspect ratio of the channel (8mm / 25mm) and therefore expect Eq. (7.2) to be a valid approximation.

The measurement technique described in (Lane et al., 2021a) has a measurement range for the phase difference of π rad (half the wavelength). We limit ourselves to this measurement range (corresponding to $\Delta n = 1.2 \cdot 10^{-5}$) since in this case the measured (relative) phase differences are the actual phase differences and Eq. (7.2) is directly applicable.

7.2.3. Aqueous cellulose nanocrystal suspensions

Two aqueous CNC suspensions with 1.0 wt% (weight percentage) and 1.2 wt% CNC were prepared by dispersing CelluForce NCC® powder (CelluForce Inc., www.celluforce.com) into distilled water. Lane et al. (2022b) used similar suspensions and report their birefringence response to shear. The measurement technique applied here can only measure birefringence in the range $0 \leq \Delta n \leq 1.2 \cdot 10^{-5}$. Therefore, only the values in that region are of interest to us. These values are shown in Table 7.1. Table 7.1 served as a look-up table for deriving $\dot{\gamma}(\Delta n)$ from Δn measurements. Linear interpolation was used between the tabulated values.

Table 7.1. Birefringence measurement data taken from Lane et al. (2022b). We only consider the values $\Delta n \leq 1.2 \cdot 10^{-5}$, as our measurement technique can only measure birefringence up to $\Delta n = 1.2 \cdot 10^{-5}$. The values in brackets are potentially affected by measurement uncertainties.

	Shear rate [1/s]						
wt%	0	0.6	1.3	1.9	2.6	3.2	3.8
	Birefringence $\Delta n \cdot 10^5$:						
1.0	(0.06)	0.2	0.33	0.42	0.52	0.60	0.67

1.2	(0.07)	0.33	0.54	0.72	0.89	1.03	(1.20)

	Shear rate [1/s]								
wt%	4.5	5.1	5.8	6.4	7.0	7.7	8.3	9.0	9.6
	Birefringence $\Delta n \cdot 10^5$:								
1.0	0.75	0.81	0.89	0.94	1.00	1.07	1.13	1.16	(1.20)

7.2.4. Fluid flow simulation with Ansys Fluent

A two-dimensional fluid flow simulation of the flow channel depicted in Fig. 7.2 (a) was performed using Ansys Fluent. The flow was assumed to be laminar, and the CNC suspensions were modelled as Newtonian fluids with a constant viscosity of 10 mPa·s. This was done even though it is commonly known that CNC suspensions are non-Newtonian, as they display shear-thinning (Shafiei-Sabet et al., 2012). However, the Newtonian simulations corresponded well with the measurements in the straight channel section (linear shear rate profile).

7.2.5. Measurement assumption

If u and v are the velocity components in x- and y-direction, respectively, and subscripts x and y indicate the directional derivates, we define the (maximum) strain rate $\dot{\varepsilon}$ as:

$$\dot{\varepsilon} = \sqrt{2u_x^2 + 2v_y^2 + (u_y + v_x)^2} = \sqrt{4u_x^2 + (u_y + v_x)^2}. \tag{7.3}$$

Note that the 2D incompressibility condition $u_x = -u_y$ was used above. We also define Λ_0 (Wayland, 1960, 1964) as the angle between the direction of $\dot{\varepsilon}$:

$$\frac{1}{2}\text{atan2}\left(u_y + v_x, 2u_x\right), \tag{7.4}$$

and the direction of flow:

$$\text{atan2}\left(v, u\right). \tag{7.5}$$

The angle Λ_0 can take values in the range [0°,90°]. Wayland (1960, 1964) argues that the angle Λ_0 affects birefringence and that Δn is therefore a function of $\dot{\varepsilon}$ and Λ_0, giving $\Delta n = \Delta n(\dot{\varepsilon}, \Lambda_0)$. For $\Lambda_0 = 45°$ the flow is a shearing flow in which different layers move parallel to each other at different speeds. The results shown in Table 7.1 were measured in a Taylor-Couette flow (i.e., a shearing flow) where $\Lambda_0 = 45°$ and $\dot{\varepsilon} = \dot{\gamma} = u_y$. If $\Lambda_0 = 0°$, the fluid is strained in the direction of the flow, for example down the centerline of a symmetrically converging channel flow. In comparison, the flow down the centerline of a symmetrically diverging channel flow is strained perpendicular to the flow direction, giving $\Lambda_0 = 90°$. In this study we use the values in Table 7.1 for all strain rates by setting: $\Delta n(\dot{\varepsilon}, \Lambda_0) \approx \Delta n(\dot{\gamma}, \Lambda_0 = 45°)$.

7.3. Results and discussion

7.3.1. Straight channel section

Figure 7.3 (a) shows the simulation and Fig. 7.3 (b) the measurements of the straight channel and the beginning of the constriction. The measurements were done using the 1.2 wt% CNC suspension. The figures are qualitatively and quantitatively similar. Most strain rates are in the range of 0-4 s^{-1} (except in the top right-hand corner of Fig. 7.3 (a) with values >4s^{-1}). Figure 7.3. (c) compares simulation and measurement results in the range -18mm ≤ x ≤ -16mm to the

theoretical solution of a plane Poiseuille flow. A straight channel flow is a shearing flow, and the linear shear rate profile is evident (note that $\dot{\epsilon} = \dot{\gamma}$ here). The figures show that if $\dot{\varepsilon} = \dot{\gamma}$ the proposed measurement technique gives reasonable results. The measurements also confirm part of the results published in Lane et al. (2022b).

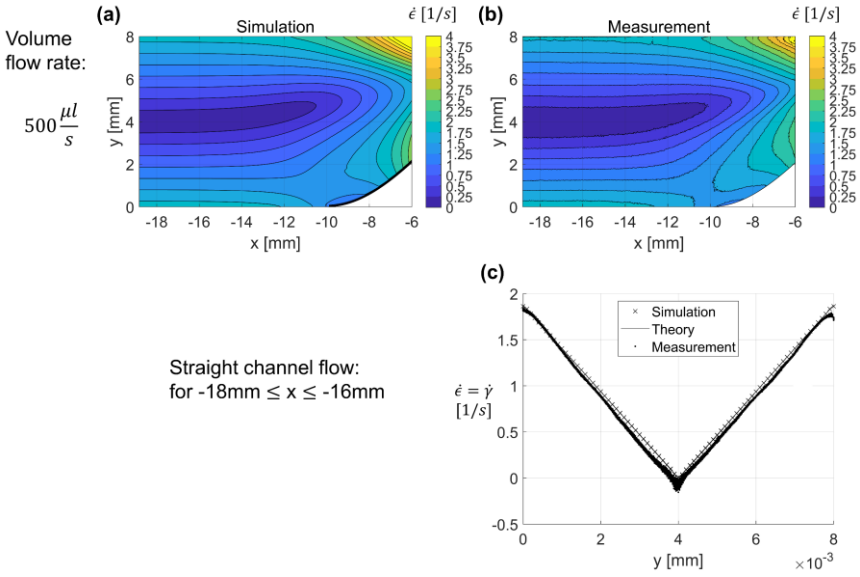

Fig. 7.3. Volume flow rate 500 $\mu l/s$ (equivalent to an average flow velocity of 2.5 mm/s). CNC suspension 1.2 wt%. Flow direction from left to right. (a) Simulation and (b) Measurement results. (c) Comparison of simulation, theory (plane Poiseuille flow), and measurements for the straight channel section.

7.3.2. Cosine shaped constriction

Figure 7.4 shows simulation and measurement results for three different flow rates in the cosine shaped constriction. Shear rates are in the range 0-10 s^{-1}. By comparing all three pairs: (a)-(b), (c)-(d), and (e)-(g) we notice that measurements

close to the wall compare well to the simulations, whereas measurements in the center of the channel display noticeable differences.

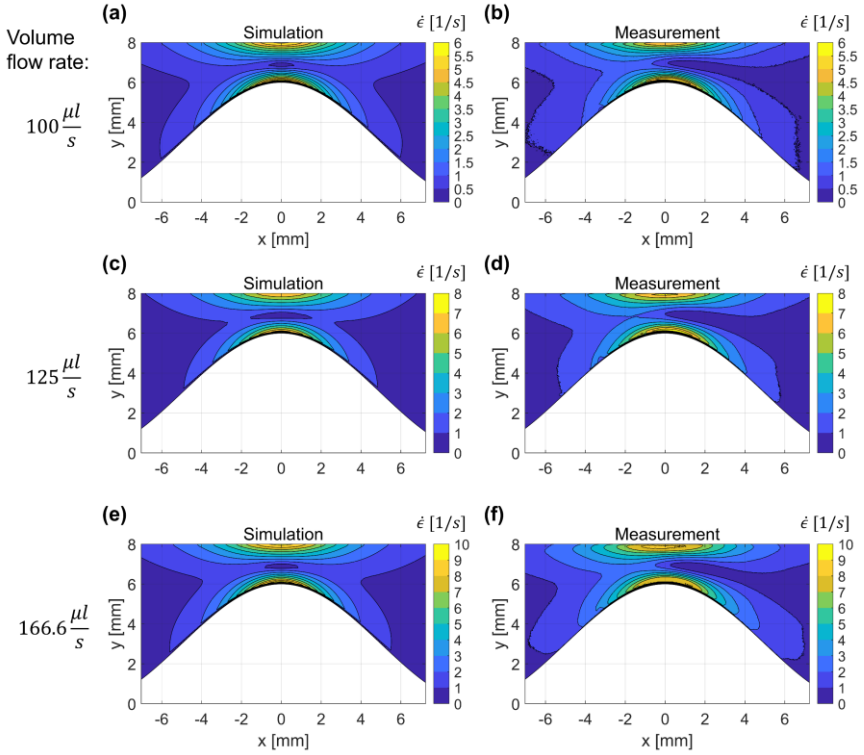

Fig. 7.4. Simulation vs. Measurement for flow rates 100 $\mu l/s$: (a) and (b), 125 $\mu l/s$: (c) and (d), and 166.6: (e) and (f). Flow direction from left to right. CNC suspension 1.0 wt%.

The flow profile should be symmetric about the x=0mm axis. The measured shear rate profiles clearly do not show this symmetry. The center shear rates are higher in the converging part than in the diverging area. We argue that the flow state, expressed by angle Λ_0, affects particle alignment and hence the birefringence response. Angles Λ_0 can easily be calculated from simulation results using Eq.

(7.4) and (7.5). Figure 7.5 shows results for a volume flow rate of 125 µl/s. The angles in the center are close to 0° and 90° in the converging and diverging channel, respectively. Calabrese et al. (2021) studied the effects of shearing and extensional flows on the alignment of CNC. For $\Lambda_0 = 90°$ the rods were orientated perpendicular to the flow direction and for $\Lambda_0 = 0°$ the rods were orientated parallel to the flow direction. For $\Lambda_0 = 45°$ the rods were orientated at about 20-30° towards the direction of flow. The rod orientation for $\Lambda_0 = 45°$ was also studied by Lane et al. (2022b) (referred to as extinction angle). Similar to Calabrese et al. (2021), rods were orientated within 23-40° towards the direction of flow. We conclude that the order of alignment for $0° < \Lambda_0 < 45°$ may be higher than it is for $45° < \Lambda_0 < 90°$. This would explain the asymmetrical shear rate distribution of Fig. 7.4 (b), (d), and (f).

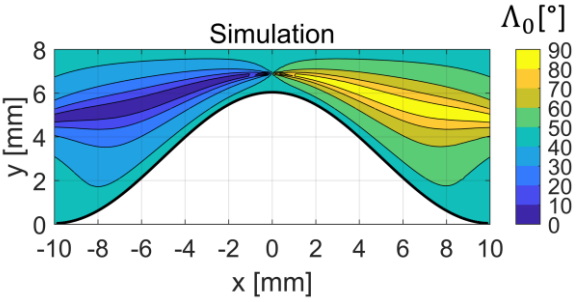

Fig. 7.5. Simulation of the angle Λ_0 between (maximum) strain rate $\dot{\epsilon}$ and direction of flow. Flow rate 125 $\mu l/s$.

7.4. Conclusion

Strain rates have been experimentally measured using a birefringent aqueous CNC suspension, a rotatable linear polarizer, and a polarization camera. The measurement accuracy seems to depend on the flow type. For a shearing flow (i.e., with an angle between maximum strain rate and direction of flow of $\Lambda_0 =$

45°) the achievable accuracy is good. If, however, the angle is close to 0° or 90°, measurement accuracy is affected. For $0° < \Lambda_0 < 45°$, measured strain rates are slightly too high, whereas they are slightly too low in regions where $45° < \Lambda_0 < 90°$. It appears that the combination of strain rate in flow direction and shear rate is more efficient in aligning the particles than the combination of strain rate perpendicular to the flow direction and shear rate. The results encourage the use of aqueous CNC suspensions for birefringent flow studies, either for shear rate imaging or for the study of shear- and strain-induced particle alignment.

8. Overall conclusion and outlook

8.1. Discussion

8.1.1. Summary

Several aspects have to be taken into account when measuring flow birefringence, such as an appropriate measurement technique, a feasible experimental design, and the actual appearance of the physical property. All three aspects were studied within this thesis.

The first two papers titled ‘Calibration of a polarization image sensor and investigation of influencing factors’ (Lane, Rode, et al., 2022a) and ‘Two-dimensional birefringence measurement technique using a polarization camera’ (Lane et al., 2021a) focus on aspects of an appropriate measurement technique. The recent introduction of polarization cameras that are based on polarization image sensors (division-of-focal-plane polarimeters) offer new opportunities that have been explored. In the first paper we define an error that quantifies the polarization measurement quality and investigate the influence of lens design, focal length, and f-number on the measurement quality. The findings provide guidance for researchers using these types of cameras. The second paper describes a two-dimensional birefringence measurement technique that uses a polarization camera. The presented approach adds to the many available birefringence measurement techniques. Advantages are its simplicity as well as the comparatively large measurement range of half the wavelength of the light. Disadvantages are that the technique cannot distinguish between the fast and slow refractive index axis and that it requires several measurements.

The third paper, ‘Optical characterization method for birefringent fluids using a polarization camera’ (Lane et al., 2021b), combines the previously discussed measurement technique with a well-known experimental design, the Taylor-Couette flow. Studying flow birefringence between two rotating cylinders is a common approach for which the paper presents a simple and convenient measurement approach.

In our study ‘Birefringent Properties of Aqueous Cellulose Nanocrystal Suspensions’ (Lane, Rode, et al., 2022b) we measured the amount of flow birefringence of a rather new type of birefringent fluid and propose its use in future studies. The findings are thought to be of interest to researchers studying cellulose nanocrystals as they characterize the response of the suspensions to shear. The results also show that these types of fluids qualify as birefringent fluids that can be used to study or visualize fluid flows.

In our final paper (Lane, Baumann, et al., 2022) presented at the *20th International Symposium on Applications of Laser and Imaging Techniques to Fluid Mechanics* conference we describe an experimental design that enables two-dimensional flow birefringence measurements and argue that not only the shear rate, but also the flow state, affects the degree of particle alignment and hence birefringence. We propose further research following these findings in section 8.2.

Several aspects within the frame of flow birefringence measurements have been studied. Some of the findings can be transferred to other research areas. The work conducted on polarization image sensors and birefringence measurement is thought to be of interest to researchers in the field of polarization imaging systems and photoelasticity. We also hope that the birefringence data of aqueous cellulose nanocrystal suspensions is relevant to the cellulose community. However, the

main objective in this thesis was to improve measurement practicability and the understanding of flow-induced birefringence as well as shear rate imaging. We have addressed some relevant aspects and hope to have given inspiration for subsequent studies.

8.1.2. Personal conclusion

Flow birefringence is an interesting phenomenon that deserves attention. It is important to realize that birefringence is primarily related to the alignment of anisotropic particles or macromolecules and not directly to stresses or strain rates. Increasing the order of alignment generally increases the amount of birefringence and the refractive index axes indicate the direction of this alignment. The degree of particle alignment is a function of the amount of stress or strain rate. However, relating flow birefringence solely to stresses and strain rates (as it is done in photoelasticity for solids) bears the risk of oversimplifying things. In particular, the results of section 7 indicate that the flow state, characterized with the help of angle Λ_0 (the angle between maximum strain rate and flow direction), influences particle alignment. Particle alignment in fluid flows is, of course, of interest to researchers and for this purpose birefringence measurements are being used, as they are very attractive in this context.

To draw reliable conclusions on local stresses and shear rates with the help of birefringence measurements I suggest combining them with velocity measurements (for example using particle image velocimetry). From the velocity measurements the flow state can be derived (angle Λ_0), and with this information stresses and strain rates can be estimated more reliably. This, however, requires appropriate reference data. Alternatively, some assumptions on the fluid flow, such as assuming a shear-dominated flow, have to be made.

As many studies do, this work has limited itself to the two-dimensional case. In the general three-dimensional case not only do the optical measurement techniques become more sophisticated, but also the relation between particle alignment and flow state is thought to be more complex. I therefore believe that the field of flow birefringence will continue to offer many research challenges as well as opportunities. In the following section we will be looking at opportunities that seem promising.

8.2. Potential future studies

8.2.1. The effect of the two-dimensional flow state on birefringence

Regarding the effect of the flow state on the amount of birefringence, as mentioned in section 2.4.1 and discussed in section 7, the birefringence response of aqueous cellulose nanocrystal (CNC) suspensions in a fluid flow is not only a function of the effective shear rate (or rather maximum strain rate), but also of the flow state. The flow state can be expressed with the help of angle Λ_0, which was defined in Eq. (2.32) (alternatively, it can be calculated with Eq. (7.4) and (7.5)). We propose further studies on this subject matter. For example, flow channels identical or similar to the one shown in Fig. 7.2 seem appropriate to study the influence of the flow state. First of all, researchers should make sure that their fluid simulations are accurate. In section 7.2.4 a Newtonian behaviour was assumed although CNC suspensions are thought to show shear-thinning effects. Nevertheless, the Newtonian assumption seemed to work well as indicated by the results shown in Fig. 7.3 (linear shear profile in a straight channel flow). The velocity field can be determined with the help of particle image velocimetry. These measurements can be compared to simulations. If the experimentally measured and simulated velocities agree, determination of the strain rates and the

angles Λ_0 from the simulations should be feasible. With this, we can measure the two-dimensional birefringence distribution and determine the amount of birefringence as well as the orientation of the refractive index axes as functions of $\dot{\varepsilon}_{\max}$ (see section 2.3 for the definition) and Λ_0, giving (compare section 2.4.1)

$$\begin{aligned} \Delta n &= \Delta n(\dot{\varepsilon}_{\max}, \Lambda_0), \\ \chi &= \chi(\dot{\varepsilon}_{\max}, \Lambda_0). \end{aligned} \tag{8.1}$$

This research will help scientists to characterize degree and orientation of CNC particle alignment for such suspensions in a fluid flow. Moreover, we hope that the findings will be able to verify our conclusion from section 7 and the general assumption that the flow state expressed by angle Λ_0 affects particle alignment.

8.2.2. Flow birefringence in axisymmetric flows

Aben and Puro (1993) describe an integrated photoelasticity method for axisymmetric flow birefringence. They make two assumptions. The first being weak birefringence (H. K. Aben et al., 1989) and the second being that the refractive index axes are aligned with the principal strain rates. They simplify the flow birefringence relations to a scalar field tomography problem where the axial velocity gradient can be determined with the help of the Radon inversion. An alternative integrated photoelasticity approach and experimental results for the strain rate analysis in a diverging and converging axisymmetric tube flow are given by Yuhai et al. (1990).

The experimental design for such flow birefringence studies is not straightforward and issues are discussed by Aben and Puro (1993). The flow channel should be placed in an immersion bath to avoid light refractions, and the channel itself must

not be birefringent. Ideally, the refractive indices of the immersion fluid, flow channel, and birefringent fluid are matched. In the scope of a student project (Köpfli, 2021) we designed such an experimental setup and our initial insights are presented here. Axisymmetric flow channels were made by shrinking a shrinking tube onto a machined core element made from metal (note that it was beneficial to drill a hole along the longitudinal axis and small holes into the side wall to avoid a vacuum when removing the shrinked-on tube). The shrinking tube was made from fluorinated ethylene propylene (FEP) with an estimated refractive index of 1.34. Due to the extrusion process involved in the manufacture of the FEP tube, the flow channel was not completely free of birefringence. A glycerol-water solution was used as an immersion fluid because the refractive index of such solutions can easily be tuned (Glycerine Producers' Association and others, 1963). Adding cellulose nanocrystals made the fluid birefringent. With this, we were able to match the refractive indices of all three parts (immersion fluid, flow channel, birefringent fluid). Our preliminary experiments showed effects of flow birefringence, but ultimately remained inconclusive, and we suggest future work on this topic.

8.2.3. Three-dimensional flow birefringence studies

We briefly discussed three-dimensional flow birefringence in section 2.6. We elaborate here briefly on two possible research opportunities in this context.

Firstly, it might be possible to develop a birefringent fluid based on cellulose nanocrystals and an experiment design that meet the conditions for the utilization of the integrated photoelasticity method (H. Aben & Puro, 1997). Preliminary studies on the birefringent fluid would be necessary to show that it fulfils the requirements. As the integrated photoelasticity method has so far not been applied

to birefringent fluids in this context (at least to our knowledge), it appears that that this research direction is worth looking in to.

Secondly, the birefringence response of the fluid is of interest. A birefringent fluid in a three-dimensional flow will generally show an optical response like a biaxial crystal. Note that this is also true for a two-dimensional flow if the third dimension is considered (see the results from Peterlin and Stuart (1939a, 1939b) described in section 6.1). For example, birefringence measurements could be conducted using two experimental designs, such as a Taylor-Couette type and a plate-plate geometry (shearing rheometers of both designs exist). Combining these results should characterize the three-dimensional optical response. As birefringence is linked to particle alignment, this is considered to be of interest.

8.2.4. Polarization sensitive optical coherence tomography

Polarization sensitive (PS) optical coherence tomography (OCT) is an extension of the established OCT technique. A review is given by de Boer et al. (2017). Researchers have applied PS-OCT in the scope of photoelasticity (Heise et al., 2010; Oh & Kim, 2003; Stifter et al., 2003). The PS-OCT technique should also be able to measure flow birefringence, and we therefore suggest flow birefringence measurements by means of PS-OCT. We also propose cellulose nanocrystal suspensions as birefringent fluids in this context, since the birefringence, as well as the transparency, can easily be modified by in- or decreasing the amount of cellulose nanocrystals.

8.3. Concluding remarks

In this thesis we have looked at birefringence measurement techniques, the physics behind flow birefringence, and the utilization of flow birefringence for

shear rate imaging. We presented the fundamentals, explained our research, and described the insights we have gained.

Measuring birefringence with the help of polarized light is a well-known approach. The rather recent introduction of commercially available polarization image sensors created new measurement opportunities in this field. The first part of this thesis deals with the application of such sensors to exploit the measurement opportunities presented.

Flow birefringence is based on the alignment of anisotropic particles or macromolecules and is an interesting phenomenon. In the second half of this thesis we report our research results on flow birefringence of aqueous cellulose nanocrystal suspensions. Cellulose nanocrystals are currently attracting a lot of scientific attention. In suspensions and when subjected to shear, these rod-like nanocrystals align, and the fluid becomes birefringent. Our work delivers experimental data that can be compared with alignment theories.

Using flow birefringence to study shear rates in a fluid flow is attractive as the measurement technique is non-invasive. If the relationship between flow state (strain rate tensor as well as direction of flow) and birefringence response can be understood and modeled, then flow birefringence will be a powerful tool for studying fluid flows.

Bibliography

Aben, H. (1979). *Integrated photoelasticity*. McGraw Hill International Book Co.

Aben, H., Ainola, L., & Errapart, A. (2010). Photoelastic tomography as hybrid mechanics. *EPJ Web of Conferences*, *6*, 32009. https://doi.org/10.1051/epjconf/20100632009

Aben, H., Errapart, A., Ainola, L., & Anton, J. (2005). Photoelastic tomography for residual stress measurement in glass. *Optical Engineering*, *44*(9), 093601. https://doi.org/10.1117/1.2047368

Aben, H., & Guillemet, C. (1993). *Photoelasticity of Glass*. Springer Berlin Heidelberg. https://doi.org/10.1007/978-3-642-50071-8

Aben, H. K., Idnurm, S. J., Josepson, J., Kell, K.-J. E., & Puro, A. E. (1992). *Optical tomography of the stress tensor field* (G. G. Levin, Ed.; pp. 220–229). https://doi.org/10.1117/12.131894

Aben, H. K., Josepson, J. I., & Kell, K.-J. E. (1989). The case of weak birefringence in integrated photoelasticity. *Optics and Lasers in Engineering*, *11*(3), 145–157. https://doi.org/10.1016/0143-8166(89)90029-8

Aben, H., & Puro, A. (1993). Integrated photoelasticity for axisymmetric flow birefringence studies. *Proceedings of the Estonian Academy of Sciences*, *42*, 7–13.

Aben, H., & Puro, A. (1997). Photoelastic tomography for three-dimensional flow birefringence studies. *Inverse Problems*, *13*(2), 215–221. https://doi.org/10.1088/0266-5611/13/2/002

Ahimaz, F. J. (1970). Birefringent-fluid tests using scattered-light technique. *Experimental Mechanics*, *10*(3), 133–134. https://doi.org/10.1007/BF02325119

Ahnert, K., & Abel, M. (2007). Numerical differentiation of experimental data: Local versus global methods. *Computer Physics Communications*, *177*(10), 764–774. https://doi.org/10.1016/j.cpc.2007.03.009

Ainola, L., & Aben, H. (2005). Principal formulas of integrated photoelasticity in terms of characteristic parameters. *Journal of the Optical Society of America A*, *22*(6), 1181. https://doi.org/10.1364/JOSAA.22.001181

Ajovalasit, A., Barone, S., & Petrucci, G. (1998). A review of automated methods for the collection and analysis of photoelastic data. *The Journal of Strain Analysis for Engineering Design*, *33*(2), 75–91. https://doi.org/10.1243/0309324981512832

Ajovalasit, A., Petrucci, G., & Scafidi, M. (2015). Review of RGB photoelasticity. *Optics and Lasers in Engineering*, *68*, 58–73. https://doi.org/10.1016/j.optlaseng.2014.12.008

Ansys. (2022, January). *Fluent Theory Guide*. https://ansyshelp.ansys.com/account/secured?returnurl=/Views/Secured/corp/v221/en/flu_th/flu_th.html

Ascough, J. (1981). A review of the scattered-light method in photoelasticity. *Optics and Lasers in Engineering*, *2*(3), 215–228. https://doi.org/10.1016/0143-8166(81)90021-X

AZoOptics. (2014, May 1). *Birefringence—Definition and Applications*. AZoOptics.Com. https://www.azooptics.com/Article.aspx?ArticleID=667 accessed 24.01.2022

Azzam, R. M. A. (2016). Stokes-vector and Mueller-matrix polarimetry [Invited]. *JOSA A*, *33*(7), 1396–1408. https://doi.org/10.1364/JOSAA.33.001396

Baas, F. (1971). Streaming birefringence in CO2 and N2. *Physics Letters A*, *36*(2), 107–108. https://doi.org/10.1016/0375-9601(71)90768-7

Bertsch, P., Diener, M., Adamcik, J., Scheuble, N., Geue, T., Mezzenga, R., & Fischer, P. (2018). Adsorption and Interfacial Layer Structure of Unmodified Nanocrystalline Cellulose at Air/Water Interfaces. *Langmuir*, *34*(50), 15195–15202. https://doi.org/10.1021/acs.langmuir.8b03056

Bertsch, P., Sánchez-Ferrer, A., Bagnani, M., Isabettini, S., Kohlbrecher, J., Mezzenga, R., & Fischer, P. (2019). Ion-Induced Formation of Nanocrystalline Cellulose Colloidal Glasses Containing Nematic Domains. *Langmuir*, *35*(11), 4117–4124. https://doi.org/10.1021/acs.langmuir.9b00281

Boer, J. F. de, Milner, T. E., Gemert, M. J. C. van, & Nelson, J. S. (1997). Two-dimensional birefringence imaging in biological tissue by polarization-sensitive optical coherence tomography. *Optics Letters*, *22*(12), 934–936. https://doi.org/10.1364/OL.22.000934

Bordel, D., Putaux, J.-L., & Heux, L. (2006). Orientation of Native Cellulose in an Electric Field. *Langmuir*, *22*(11), 4899–4901. https://doi.org/10.1021/la0600402

Boyer, G. R., Lamouroux, B., & Prade, B. S. (1978). Atmospheric birefringence under wind speed gradient shear*. *Journal of the Optical Society of America*, *68*(4), 471. https://doi.org/10.1364/JOSA.68.000471

Calabrese, V., Haward, S. J., & Shen, A. Q. (2021). Effects of Shearing and Extensional Flows on the Alignment of Colloidal Rods. *Macromolecules*, *54*(9), 4176–4185. https://doi.org/10.1021/acs.macromol.0c02155

Calabrese, V., Varchanis, S., Haward, S. J., Tsamopoulos, J., & Shen, A. Q. (2021). Structure-property relationship of a soft colloidal glass in simple

and mixed flows. *Journal of Colloid and Interface Science*, *601*, 454–466. https://doi.org/10.1016/j.jcis.2021.05.103

Cerf, Roger., & Scheraga, H. A. (1952). Flow Birefringence in Solutions of Macromolecules. *Chemical Reviews*, *51*(2), 185–261. https://doi.org/10.1021/cr60159a001

Chen, Z., Wang, X., & Liang, R. (2015). Calibration method of microgrid polarimeters with image interpolation. *Applied Optics*, *54*(5), 995–1001. https://doi.org/10.1364/AO.54.000995

Chipman, R. A. (1994). Polarimetry. In *Handbook of Optics* (Vol. 2, p. 22.1-22.37). McGraw-Hill. https://ci.nii.ac.jp/naid/10026586244/

Chipman, R. A., Lam, W.-S. T., & Young, G. (2018a). Typical polarization problems in optical systems. In *Polarized Light and Optical Systems* (1st ed., pp. 12–17). CRC Press. https://doi.org/10.1201/9781351129121

Chipman, R. A., Lam, W.-S. T., & Young, G. (2018b). *Polarized Light and Optical Systems*. CRC Press. https://doi.org/10.1201/9781351129121

Chow, A. W., & Fuller, G. G. (1984). Response of Moderately Concentrated Xanthan Gum Solutions to Time-Dependent Flows Using Two-Color Flow Birefringence. *Journal of Rheology*, *28*(1), 23–43. https://doi.org/10.1122/1.549767

Chow, A. W., & Fuller, G. G. (1985). Some experimental results on the development of Couette flow for non-Newtonian fluids. *Journal of Non-Newtonian Fluid Mechanics*, *17*(2), 233–243. https://doi.org/10.1016/0377-0257(85)80017-3

Chowdhury, R. A., Peng, S. X., & Youngblood, J. (2017). Improved order parameter (alignment) determination in cellulose nanocrystal (CNC) films by a simple optical birefringence method. *Cellulose*, *24*(5), 1957–1970. https://doi.org/10.1007/s10570-017-1250-9

Collett, E. (2005). *Field guide to polarization*. SPIE Press.

Corona, P. T., Ruocco, N., Weigandt, K. M., Leal, L. G., & Helgeson, M. E. (2018). Probing flow-induced nanostructure of complex fluids in arbitrary 2D flows using a fluidic four-roll mill (FFoRM). *Scientific Reports*, *8*(1), 15559. https://doi.org/10.1038/s41598-018-33514-8

Cowling, S. J. (2014). Optical microscopy studies of liquid crystals. *Handbook of Liquid Crystals*.

Cressely, R., Hocquart, R., Wydro, T., & Decruppe, J. P. (1985). Numerical evaluation of extinction angle and birefringence in various directions as a function of velocity gradient. *Rheologica Acta*, *24*(4), 419–426. https://doi.org/10.1007/BF01333969

Davey, A. (1962). The growth of Taylor vortices in flow between rotating cylinders. *Journal of Fluid Mechanics*, *14*(3), 336–368. https://doi.org/10.1017/S0022112062001287

de Boer, J. F., Hitzenberger, C. K., & Yasuno, Y. (2017). Polarization sensitive optical coherence tomography – a review [Invited]. *Biomedical Optics Express*, *8*(3), 1838. https://doi.org/10.1364/BOE.8.001838

de Boer, J. F., Milner, T. E., van Gemert, M. J. C., & Nelson, J. S. (1998). Two-Dimensional birefringence imaging in biological tissue using phase and polarization sensitive optical coherence tomography. *Advances in Optical Imaging and Photon Migration*, AMC2. https://doi.org/10.1364/AOIPM.1998.AMC2

De Senarmont, H. (1840). Sur les modifications que la réflexion spéculaire à la surface des corps métalliques imprime à un rayon de lumière polarisée. *Ann. Chim. Phys*, *73*, 337–362.

Decruppe, J. P., Cressely, R., Makhloufi, R., & Cappelaere, E. (1995). Flow birefringence experiments showing a shear-banding structure in a CTAB

solution. *Colloid and Polymer Science*, *273*(4), 346–351. https://doi.org/10.1007/BF00652348

Decruppe, J. P., Hocquart, R., Wydro, T., & Cressely, R. (1989). Flow birefringence study at the transition from laminar to Taylor vortex flow. *Journal de Physique*, *50*(23), 3371–3394. https://doi.org/10.1051/jphys:0198900500230337100

Deplano, V., & Siouffi, M. (1999). Experimental and numerical study of pulsatile flows through stenosis: *Journal of Biomechanics*, *32*(10), 1081–1090. https://doi.org/10.1016/S0021-9290(99)00098-6

Doi, M., & Edwards, S. F. (1978). Dynamics of rod-like macromolecules in concentrated solution. Part 2. *Journal of the Chemical Society, Faraday Transactions 2*, *74*, 918. https://doi.org/10.1039/f29787400918

Dupré, J. C., Valle, V., Jarny, S., & Monnet, P. (2010). Fringe analysis by phase shifting technique for birefringent fluid studies. *Optics and Lasers in Engineering*, *48*(1), 37–42. https://doi.org/10.1016/j.optlaseng.2009.07.015

Durelli, A. J., & Norgard, J. S. (1972). Experimental analysis of slow viscous flow using photoviscosity and bubbles. *Experimental Mechanics*, *12*(4), 169–177. https://doi.org/10.1007/BF02330269

Ebeling, T., Paillet, M., Borsali, R., Diat, O., Dufresne, A., Cavaillé, J.-Y., & Chanzy, H. (1999). Shear-Induced Orientation Phenomena in Suspensions of Cellulose Microcrystals, Revealed by Small Angle X-ray Scattering. *Langmuir*, *15*(19), 6123–6126. https://doi.org/10.1021/la990046+

Elsevier. (2022, February 16). *Permissions*. Elsevier.Com. https://www.elsevier.com/about/policies/copyright/permissions

Ferraton, M., Stolz, C., & Mériaudeau, F. (2009). Optimization of a polarization imaging system for 3D measurements of transparent objects. *Optics Express*, *17*(23), 21077. https://doi.org/10.1364/OE.17.021077

Föppl, L., & Mönch, E. (1950). *Praktische Spannungsoptik*. Springer Berlin Heidelberg. https://doi.org/10.1007/978-3-642-52730-2

Freundlich, H. (1916). Die Doppelbrechung Des Vanadinpentoxydsols. *Zeitschrift Für Elektrochemie Und Angewandte Physikalische Chemie*, *22*(1–2), 27–33. https://doi.org/10.1002/bbpc.19160220108

Frka-Petesic, B., Sugiyama, J., Kimura, S., Chanzy, H., & Maret, G. (2015). Negative Diamagnetic Anisotropy and Birefringence of Cellulose Nanocrystals. *Macromolecules*, *48*(24), 8844–8857. https://doi.org/10.1021/acs.macromol.5b02201

Fuller, G. G. (1990). Optical Rheometry. *Annual Review of Fluid Mechanics*, *22*(1), 387–417. https://doi.org/10.1146/annurev.fl.22.010190.002131

Fuller, G. G. (1995a). *Optical rheometry of complex fluids*. Oxford University Press.

Fuller, G. G. (1995b). Transmission by anisotropic media: The Jones and Mueller calculus. In *Optical rheometry of complex fluids* (pp. 23–44). Oxford University Press.

Funfschilling, D., & Li, H. Z. (2001). Flow of non-Newtonian fluids around bubbles: PIV measurements and birefringence visualisation. *Chemical Engineering Science*, *56*(3), 1137–1141. https://doi.org/10.1016/S0009-2509(00)00332-8

Ganapati, V., Schoenfelder, S., Castellanos, S., Oener, S., Koepge, R., Sampson, A., Marcus, M. A., Lai, B., Morhenn, H., Hahn, G., Bagdahn, J., & Buonassisi, T. (2010). Infrared birefringence imaging of residual stress

and bulk defects in multicrystalline silicon. *Journal of Applied Physics*, *108*(6), 063528. https://doi.org/10.1063/1.3468404

Giménez, Y., Lapray, P.-J., Foulonneau, A., & Bigué, L. (2019). Calibration for polarization filter array cameras: Recent advances. *Fourteenth International Conference on Quality Control by Artificial Vision*, *11172*, 297–302. https://doi.org/10.1117/12.2521752

Gimenez, Y., Lapray, P.-J., Foulonneau, A., & Bigué, L. (2020). Calibration algorithms for polarization filter array camera: Survey and evaluation. *Journal of Electronic Imaging*, *29*(4), 041011. https://doi.org/10.1117/1.JEI.29.4.041011

Glazer, A. M., Lewis, J. G., & Kaminsky, W. (1996). An automatic optical imaging system for birefringent media. *Proceedings of the Royal Society of London. Series A: Mathematical, Physical and Engineering Sciences*, *452*(1955), 2751–2765. https://doi.org/10.1098/rspa.1996.0145

Glycerine Producers' Association and others. (1963). *Physical properties of glycerine and its solutions*. Glycerine Producers' Association.

Habibi, Y., Lucia, L. A., & Rojas, O. J. (2010). Cellulose Nanocrystals: Chemistry, Self-Assembly, and Applications. *Chemical Reviews*, *110*(6), 3479–3500. https://doi.org/10.1021/cr900339w

Hagen, N. A., Shibata, S., & Otani, Y. (2019). Calibration and performance assessment of microgrid polarization cameras. *Optical Engineering*, *58*(8), 082408. https://doi.org/10.1117/1.OE.58.8.082408

Hall, S. A., Hoyle, M.-A., Post, J. S., & Hore, D. K. (2013). Combined Stokes Vector and Mueller Matrix Polarimetry for Materials Characterization. *Analytical Chemistry*, *85*(15), 7613–7619. https://doi.org/10.1021/ac401864g

Han, G., Hu, X., Lian, J., He, X., Zhang, L., Wang, Y., & Dong, F. (2017). Design and Calibration of a Novel Bio-Inspired Pixelated Polarized Light Compass. *Sensors*, *17*(11), 2623. https://doi.org/10.3390/s17112623

Hausmann, M. K., Rühs, P. A., Siqueira, G., Läuger, J., Libanori, R., Zimmermann, T., & Studart, A. R. (2018). Dynamics of Cellulose Nanocrystal Alignment during 3D Printing. *ACS Nano*, *12*(7), 6926–6937. https://doi.org/10.1021/acsnano.8b02366

Hecht, E. (1998a). Geometrical optics. In *Optics* (3rd ed, pp. 148–246). Addison-Wesley.

Hecht, E. (1998b). Polarization. In *Optics* (3rd ed, pp. 319–376). Addison-Wesley.

Heise, B., Wiesauer, K., GÃ¶tzinger, E., Pircher, M., Hitzenberger, C. K., Engelke, R., Ahrens, G., Grützner, G., & Stifter, D. (2010). Spatially Resolved Stress Measurements in Materials With Polarisation-Sensitive Optical Coherence Tomography: Image Acquisition and Processing Aspects. *Strain*, *46*(1), 61–68. https://doi.org/10.1111/j.1475-1305.2008.00589.x

Hess, S. (1969). Flow birefringence of polyatomic gases. *Physics Letters A*, *30*(4), 239–240. https://doi.org/10.1016/0375-9601(69)90878-0

Horsmann, M., & Merzkirch, W. (1981). Scattered light streaming birefringence in colloidal solutions. *Rheologica Acta*, *20*(5), 501–510. https://doi.org/10.1007/BF01503273

Hu, D. L., Goreau, T. J., & Bush, J. W. M. (2009). Flow visualization using tobacco mosaic virus. *Experiments in Fluids*, *46*(3), 477–484. https://doi.org/10.1007/s00348-008-0573-6

Humphry, R. H. (1922). Demonstration of the Double Refraction due to Motion of a Vanadium Pentoxide Sol, and Some Applications. *Proceedings of*

the Physical Society of London, *35*(1), 217–218. https://doi.org/10.1088/1478-7814/35/1/331

Iwata, S., Takahashi, T., Onuma, T., Nagumo, R., & Mori, H. (2019). Local flow around a tiny bubble under a pressure-oscillation field in a viscoelastic worm-like micellar solution. *Journal of Non-Newtonian Fluid Mechanics*, *263*, 24–32. https://doi.org/10.1016/j.jnnfm.2018.11.002

Iyer, K. R. K., Neelakantan, P., & Radhakrishnan, T. (1968). Birefringence of native cellulosic fibers. I. Untreated cotton and ramie. *Journal of Polymer Science Part A-2: Polymer Physics*, *6*(10), 1747–1758. https://doi.org/10.1002/pol.1968.160061005

Jakubek, Z. J., Chen, M., Couillard, M., Leng, T., Liu, L., Zou, S., Baxa, U., Clogston, J. D., Hamad, W. Y., & Johnston, L. J. (2018). Characterization challenges for a cellulose nanocrystal reference material: Dispersion and particle size distributions. *Journal of Nanoparticle Research*, *20*(4), 98. https://doi.org/10.1007/s11051-018-4194-6

Janeschitz-Kriegl, H. (1969). Flow birefringence of elastico-viscous polymer systems. In *Fortschritte der Hochpolymeren-Forschung* (Vol. 6/2, pp. 170–318). Springer-Verlag. https://doi.org/10.1007/BFb0051073

Janeschitz-Kriegl, H. (1983). *Polymer Melt Rheology and Flow Birefringence*. https://doi.org/10.1007/978-3-642-68822-5

Jeffery, G. B. (1922). The Motion of Ellipsoidal Particles Immersed in a Viscous Fluid. *Proceedings of the Royal Society of London. Series A, Containing Papers of a Mathematical and Physical Character*, *102*(715), 161–179.

Jerrard, H. G. (1948). Optical Compensators for Measurement of Elliptical Polarization. *Journal of the Optical Society of America*, *38*(1), 35. https://doi.org/10.1364/JOSA.38.000035

Jones, R. C. (1942). A New Calculus for the Treatment of Optical Systems IV. *Journal of the Optical Society of America*, *32*(8), 486. https://doi.org/10.1364/JOSA.32.000486

Kaap, P. (2010). *Experimentelle Untersuchung von Fluiden mit doppelbrechenden Eigenschaften* [TU Berlin]. https://icm.charite.de/

Kent State University. (2022). *What Are Liquid Crystals? | Kent State University*. https://www.kent.edu/amlci/what-are-liquid-crystals accessed 25.01.2022

Kihara, T. (2004). Photoelastic model measurement with rotated principal axes by scattered-light photoelasticity. *Experimental Mechanics*, *44*(5), 455–460. https://doi.org/10.1007/BF02427956

Klemm, D., Philipp, B., Heinze, T., Heinze, U., & Wagenknect, W. (1998). *Comprehensive cellulose chemistry. Volume 1: Fundamentals and analytical methods*. Wiley-VCH. https://doi.org/10.1002/3527601929

Köpfli, A. (2021). *Entwicklung eines Messaufbaus für scheroptische Untersuchungen* [Bachelor Thesis]. ETH Zürich.

Krishnamurthy, A. R., & Pindera, J. T. (1982). Study of basic patterns of light scattering in aqueous solution of milling yellow. *Experimental Mechanics*, *22*(1), 1–7. https://doi.org/10.1007/BF02325695

Kundu, P. K., Cohen, I. M., & Dowling, D. R. (2012). *Fluid mechanics* (5th ed). Academic Press.

Lagerwall, J. P. F., Schütz, C., Salajkova, M., Noh, J., Hyun Park, J., Scalia, G., & Bergström, L. (2014). Cellulose nanocrystal-based materials: From liquid crystal self-assembly and glass formation to multifunctional thin films. *NPG Asia Materials*, *6*(1), e80–e80. https://doi.org/10.1038/am.2013.69

Lane, C., Baumann, F., & Rösgen, T. (2022). Shear rate imaging using a polarization camera and a birefringent aqueous cellulose nanocrystal suspension. *20th International Symposium on Applications of Laser and Imaging Techniques to Fluid Mechanics, Lisbon, Portugal, forthcoming*.

Lane, C., Rode, D., & Rösgen, T. (2021a). Two-dimensional birefringence measurement technique using a polarization camera. *Applied Optics*, *60*(27), 8435. https://doi.org/10.1364/AO.433066

Lane, C., Rode, D., & Rösgen, T. (2021b). Optical characterization method for birefringent fluids using a polarization camera. *Optics and Lasers in Engineering*, *146*, 106724. https://doi.org/10.1016/j.optlaseng.2021.106724

Lane, C., Rode, D., & Rösgen, T. (2022a). Calibration of a polarization image sensor and investigation of influencing factors. *Applied Optics*, *61*(6), C37. https://doi.org/10.1364/AO.437391

Lane, C., Rode, D., & Rösgen, T. (2022b). Birefringent properties of aqueous cellulose nanocrystal suspensions. *Cellulose*. https://doi.org/10.1007/s10570-022-04646-y

Li, X., Goudail, F., Qi, P., Liu, T., & Hu, H. (2021). Integration time optimization and starting angle autocalibration of full Stokes imagers based on a rotating retarder. *Optics Express*, *29*(6), 9494. https://doi.org/10.1364/OE.418399

Li, X., Le Teurnier, B., Boffety, M., Liu, T., Hu, H., & Goudail, F. (2020). Theory of autocalibration feasibility and precision in full Stokes polarization imagers. *Optics Express*, *28*(10), 15268. https://doi.org/10.1364/OE.390882

Lin, P. L., Han, C. Y., & Chao, Y. F. (2008). Three-intensity measurement technique and its measurement in elliptical retarder. *Optics*

Communications, *281*(13), 3403–3406. https://doi.org/10.1016/j.optcom.2008.02.042

Lin, S.-S., Yemelyanov, K. M., Pugh, Jr., E. N., & Engheta, N. (2006). Polarization-based and specular-reflection-based noncontact latent fingerprint imaging and lifting. *Journal of the Optical Society of America A*, *23*(9), 2137. https://doi.org/10.1364/JOSAA.23.002137

Liu, G., Xiong, J., Cao, Y., Hou, R., Zhi, L., Xia, Z., Liu, W., Liu, X., Glorieux, C., Marsh, J. H., & Hou, L. (2020). Visualization of ultrasonic wave field by stroboscopic polarization selective imaging. *Optics Express*, *28*(18), 27096. https://doi.org/10.1364/OE.400355

LUCID Vision Labs. (2022, February 1). *Phoenix 5.0MP Polarsens Polarization Camera, Sony's IMX250MZR and IMX250MYR CMOS | LUCID Vision Labs*. https://thinklucid.com/product/phoenix-5-0-mp-polarized-model/

Mackley, M. R., & Hassell, D. G. (2011). The multipass rheometer a review. *Journal of Non-Newtonian Fluid Mechanics*, *166*(9), 421–456. https://doi.org/10.1016/j.jnnfm.2011.01.007

Maguire, J. F., McTague, J. P., & Rondelez, F. (1980). Rotational Diffusion of Sterically Interacting Rodlike Macromolecules. *Physical Review Letters*, *45*(23), 1891–1894. https://doi.org/10.1103/PhysRevLett.45.1891

Martyn, M. T., Groves, D. J., & Coates, P. D. (2000). In process measurement of apparent extensional viscosity of low density polyethylene melts using flow visualisation. *Plastics, Rubber and Composites*, *29*(1), 14–22. https://doi.org/10.1179/146580100101540653

Matsuura, K., Hattori, S., Noda, I., & Nagasawa, M. (1978). Measurement of flow-birefringence using a circularly polarized laser beam. *Optics &*

Laser Technology, *10*(5), 237–240. https://doi.org/10.1016/0030-3992(78)90005-1

Maxwell, J. C. (1874). IV. On double refraction in a viscous fluid in motion. *Proceedings of the Royal Society of London*, *22*(148–155), 46–47. https://doi.org/10.1098/rspl.1873.0011

McAfee, W. J., & Pih, H. (1971). A Scattered Light Polariscope for Three-Dimensional Birefringent Flow Studies. *Review of Scientific Instruments*, *42*(2), 221–223. https://doi.org/10.1063/1.1685050

McHugh, A. J., Mackay, M. E., & Khomami, B. (1987). Measurement of Birefringence by the Method of Isoclinics. *Journal of Rheology*, *31*(7), 619–634. https://doi.org/10.1122/1.549939

McKeon, B. J., Comte-Bellot, G., Foss, J. F., Westerweel, J., Scarano, F., Tropea, C., Meyers, J. F., Lee, J. W., Cavone, A. A., Schodl, R., Koochesfahani, M. M., Nocera, D. G., Andreopoulos, Y., Dahm, W. J. A., Mullin, J. A., Wallace, J. M., Vukoslavcevic, P. V., Morris, S. C., Pardyjak, E. R., & Cuerva, A. (2007). Velocity, Vorticity, and Mach Number. In *Springer handbook of experimental fluid mechanics* (pp. 215–472). Springer.

Mei, G., & Oldenbourg, R. (1994). Fast imaging polarimetry with precision universal compensator. *Polarization Analysis and Measurement II*, *2265*, 29–39. https://doi.org/10.1117/12.186681

Merzkirch, W. (2001). Streaming Birefringence. In *Handbook of Flow Visualization*. Routledge.

Meyer, E. L., Fuller, G. G., Clark, R. C., & Kulicke, W. M. (1993). Investigation of xanthan gum solution behavior under shear flow using rheooptical techniques. *Macromolecules*, *26*(3), 504–511. https://doi.org/10.1021/ma00055a016

Morel, O., Stolz, C., Meriaudeau, F., & Gorria, P. (2006). Active lighting applied to three-dimensional reconstruction of specular metallic surfaces by polarization imaging. *Applied Optics*, *45*(17), 4062. https://doi.org/10.1364/AO.45.004062

Myhre, G., Hsu, W.-L., Peinado, A., LaCasse, C., Brock, N., Chipman, R. A., & Pau, S. (2012). Liquid crystal polymer full-stokes division of focal plane polarimeter. *Optics Express*, *20*(25), 27393–27409. https://doi.org/10.1364/OE.20.027393

Mykhaylyk, O. O., Warren, N. J., Parnell, A. J., Pfeifer, G., & Laeuger, J. (2016). Applications of shear-induced polarized light imaging (SIPLI) technique for mechano-optical rheology of polymers and soft matter materials. *Journal of Polymer Science Part B: Polymer Physics*, *54*(21), 2151–2170. https://doi.org/10.1002/polb.24111

Nakagaki, M., & Heller. (1975). Recomputation of certain functions in the Peterlin–Stuart theory of flow birefringence and directions for the evaluation of experimental data in terms of molecular weights and molecular dimensions. *The Journal of Chemical Physics*, *62*(2), 333. https://doi.org/10.1063/1.430490

Nurse, A. D. (1997). Full-field automated photoelasticity by use of a three-wavelength approach to phase stepping. *Applied Optics*, *36*(23), 5781–5786. https://doi.org/10.1364/AO.36.005781

Oba, N., & Inoue, T. (2016). An apparatus for birefringence and extinction angle distributions measurements in cone and plate geometry by polarization imaging method. *Rheologica Acta*, *55*(9), 699–708. https://doi.org/10.1007/s00397-016-0952-5

Ober, T. J., Soulages, J., & McKinley, G. H. (2011). Spatially resolved quantitative rheo-optics of complex fluids in a microfluidic device.

Journal of Rheology, *55*(5), 1127–1159. https://doi.org/10.1122/1.3606593

Oh, J.-T., & Kim, S.-W. (2003). Polarization-sensitive optical coherence tomography for photoelasticity testing of glass/epoxy composites. *Optics Express*, *11*(14), 1669. https://doi.org/10.1364/OE.11.001669

Oldenbourg, R., & Mei, G. (1995). New polarized light microscope with precision universal compensator. *Journal of Microscopy*, *180*(2), 140–147. https://doi.org/10.1111/j.1365-2818.1995.tb03669.x

Onuma, T., & Otani, Y. (2014). A development of two-dimensional birefringence distribution measurement system with a sampling rate of 1.3MHz. *Optics Communications*, *315*, 69–73. https://doi.org/10.1016/j.optcom.2013.10.086

Optica Publishing Group. (2022, March 31). *Author Resources: Copyright Transfer and Licensing Information*. https://opg.optica.org/submit/review/copyright_permissions.cfm?source=authornav&section=oa_posting#posting

Osaki, K., Bessho, N., Kojimoto, T., & Kurata, M. (1979). Flow Birefringence of Polymer Solutions in Time-Dependent Field. *Journal of Rheology*, *23*(4), 457–475. https://doi.org/10.1122/1.549553

Otani, Y. (2021). Snapshot full Stokes imager by polarization cameras and its application to bio-imaging. In T. Yatagai, Y. Koike, & S. Miyata (Eds.), *Ultra-High-Definition Imaging Systems IV* (p. 1). SPIE. https://doi.org/10.1117/12.2587339

Otani, Y., Shimada, T., & YoSHIZAWA, T. (1994). The Local-Sampling Phase Shifting Technique for Precise Two-Dimensional Birefringence Measurement. *Optical Review*, *1*(1), 103–106. https://doi.org/10.1007/s10043-994-0103-6

Otani, Y., Shimada, T., Yoshizawa, T., & Umeda, N. (1994). Two-dimensional birefringence measurement using the phase shifting technique. *Optical Engineering*, *33*(5), 1604–1609. https://doi.org/10.1117/12.168435

Papaioannou, T. G., & Stefanadis, C. (2005). Vascular wall shear stress: Basic principles and methods. *Hellenic Journal of Cardiology: HJC = Hellenike Kardiologike Epitheorese*, *46*(1), 9–15.

Parker, R. M., Guidetti, G., Williams, C. A., Zhao, T., Narkevicius, A., Vignolini, S., & Frka-Petesic, B. (2018). The Self-Assembly of Cellulose Nanocrystals: Hierarchical Design of Visual Appearance. *Advanced Materials*, *30*(19), 1704477. https://doi.org/10.1002/adma.201704477

Patterson, E. A., Ji, W., & Wang, Z. F. (1997). On image analysis for Birefringence measurements in photoelasticity. *Optics and Lasers in Engineering*, *28*(1), 17–36. https://doi.org/10.1016/S0143-8166(96)00060-7

Peebles, F. N., & Liu, K. C. (1965). Photoviscous analysis of two-dimensional laminar flow in an expanding jet: Birefringence patterns are analyzed to determine the velocity distributions in steady, laminar flow. *Experimental Mechanics*, *5*(9), 299–304. https://doi.org/10.1007/BF02326295

Peebles, F. N., Prados, J. W., & Honeycutt, E. H. (1964). Birefringent and rheologic properties of milling yellow suspensions. *Journal of Polymer Science Part C: Polymer Symposia*, *5*(1), 37–53. https://doi.org/10.1002/polc.5070050105

Peng, Y., Gardner, D. J., & Han, Y. (2012). Drying cellulose nanofibrils: In search of a suitable method. *Cellulose*, *19*(1), 91–102. https://doi.org/10.1007/s10570-011-9630-z

Peterlin, A. (1938). Über die Viskosität von verdünnten Lösungen und Suspensionen in Abhängigkeit von der Teilchenform. *Zeitschrift für Physik*, *111*(3–4), 232–263. https://doi.org/10.1007/BF01332211

Peterlin, A. (1976). Optical Effects in Flow. *Annual Review of Fluid Mechanics*, *8*(1), 35–55. https://doi.org/10.1146/annurev.fl.08.010176.000343

Peterlin, A., & Stuart, H. A. (1939a). Zur Theorie der Strömungsdoppelbrechung von Kolloiden und großen Molekülen in Lösung. *Zeitschrift für Physik*, *112*(1–2), 1–19. https://doi.org/10.1007/BF01325633

Peterlin, A., & Stuart, H. A. (1939b). Über die Bestimmung der Größe und Form, sowie der elektrischen, optischen und magnetischen Anisotropie von submikroskopischen Teilchen mit Hilfe der künstlichen Doppelbrechung und der inneren Reibung. *Zeitschrift für Physik*, *112*(3–4), 129–147. https://doi.org/10.1007/BF01340060

Pezzaniti, J. L., & Chipman, R. A. (1995). Mueller matrix imaging polarimetry. *Optical Engineering*, *34*(6), 1558–1568. https://doi.org/10.1117/12.206161

Pih, H. (1980). Birefringent-fluid-flow method in engineering: The development of the two-dimensional birefringent-fluid flow was reviewed. Some results of the application in engineering are given. Recent extension into three-dimensional flows is also discussed. *Experimental Mechanics*, *20*(12), 437–444. https://doi.org/10.1007/BF02320884

Pindera, J. T., & Krishnamurthy, A. R. (1978). Characteristic relations of flow birefringence: Part 1: Relations in transmitted radiation Contemporary problems of flow-birefringence studies in transmitted light are discussed. The influence of spectral frequency is shown to be important in understanding the basic birefringence mechanisms and in optimizing

the flow-birefringence experiments. *Experimental Mechanics*, *18*(1), 1–10. https://doi.org/10.1007/BF02326551

Powell, S. B., & Gruev, V. (2013). Calibration methods for division-of-focal-plane polarimeters. *Optics Express*, *21*(18), 21039–21055. https://doi.org/10.1364/OE.21.021039

Puttonen, E., Suomalainen, J., Hakala, T., & Peltoniemi, J. (2009). Measurement of Reflectance Properties of Asphalt Surfaces and Their Usability as Reference Targets for Aerial Photos. *IEEE Transactions on Geoscience and Remote Sensing*, *47*(7), 2330–2339. https://doi.org/10.1109/TGRS.2008.2010132

Quinzani, L. M., Armstrong, R. C., & Brown, R. A. (1994). Birefringence and laser-Doppler velocimetry (LDV) studies of viscoelastic flow through a planar contraction. *Journal of Non-Newtonian Fluid Mechanics*, *52*(1), 1–36. https://doi.org/10.1016/0377-0257(94)85056-9

Ramesh, K. (2000). *Digital Photoelasticity Advanced Techniques and Applications*. Springer. https://doi.org/10.1007/978-3-642-59723-7

Ramesh, K., Kasimayan, T., & Neethi Simon, B. (2011). Digital photoelasticity – A comprehensive review. *The Journal of Strain Analysis for Engineering Design*, *46*(4), 245–266. https://doi.org/10.1177/0309324711401501

Ramesh, K., & Ramakrishnan, V. (2016). Digital photoelasticity of glass: A comprehensive review. *Optics and Lasers in Engineering*, *87*, 59–74. https://doi.org/10.1016/j.optlaseng.2016.03.017

Ramesh, K., & Sasikumar, S. (2020). Digital photoelasticity: Recent developments and diverse applications. *Optics and Lasers in Engineering*, *135*, 106186. https://doi.org/10.1016/j.optlaseng.2020.106186

Rankin, G. W., Sabbah, H. N., & Stein, P. D. (1989). A streaming birefringence study of the flow at the junction of the aorta and the renal arteries. *Experiments in Fluids*, *7*(2), 73–80. https://doi.org/10.1007/BF00207298

Ratliff, B. M., LaCasse, C. F., & Tyo, J. S. (2009). Interpolation strategies for reducing IFOV artifacts in microgrid polarimeter imagery. *Optics Express*, *17*(11), 9112–9125. https://doi.org/10.1364/OE.17.009112

Saba, A., Lim, J., Ayoub, A. B., Antoine, E. E., & Psaltis, D. (2021). Polarization-sensitive optical diffraction tomography. *Optica*, *8*(3), 402–408. https://doi.org/10.1364/OPTICA.415343

Sarma, A. V. S. S. S. R. (1977). New experimental methods for determining the optical parameters of elliptic retarders. *Journal of Physics D: Applied Physics*, *10*(15), 2019–2030. https://doi.org/10.1088/0022-3727/10/15/006

Sattar, S., Lapray, P.-J., Foulonneau, A., & Bigué, L. (2020). Review of spectral and polarization imaging systems. In C. Fournier, M. P. Georges, & G. Popescu (Eds.), *Unconventional Optical Imaging II* (p. 68). SPIE. https://doi.org/10.1117/12.2555745

Schechner, Y. Y., Narasimhan, S. G., & Nayar, S. K. (2003). Polarization-based vision through haze. *Applied Optics*, *42*(3), 511. https://doi.org/10.1364/AO.42.000511

Scheraga, H. A., Edsall, J. T., & Gadd, J. O. (1951). Double Refraction of Flow: Numerical Evaluation of Extinction Angle and Birefringence as a Function of Velocity Gradient. *The Journal of Chemical Physics*, *19*(9), 1101–1108. https://doi.org/10.1063/1.1748483

Schmitz, E., & Merzkirch, W. (1984). A test fluid for simulating blood flows. *Experiments in Fluids*, *2*(2), 103–104.

Schneider, T. (2013). *Spannungsoptik-Tomographie in Strömungen*. https://depositonce.tu-berlin.de/handle/11303/3781

Schneider, T., Goubergrits, L., Paschereit, C. O., Kertzscher, U., & Affeld, K. (2012). Spannungsoptik-Tomographie zur Messung der Scherung in Strömungen. *Teme*, *79*(6), 304–309. https://doi.org/10.1524/teme.2012.0211

Shafiei-Sabet, S., Hamad, W. Y., & Hatzikiriakos, S. G. (2012). Rheology of Nanocrystalline Cellulose Aqueous Suspensions. *Langmuir*, *28*(49), 17124–17133. https://doi.org/10.1021/la303380v

Shibata, S., Hagen, N., & Otani, Y. (2019). Robust full Stokes imaging polarimeter with dynamic calibration. *Optics Letters*, *44*(4), 891. https://doi.org/10.1364/OL.44.000891

Shribak, M. I., & Oldenbourg, R. (2002). Sensitive measurements of two-dimensional birefringence distributions using near-circularly polarized beam. *Polarization Measurement, Analysis, and Applications V*, *4819*, 56–67. https://doi.org/10.1117/12.463750

Shribak, M. I., Otani, Y., & Yoshizawa, T. (1999). Return-path polarimeter for two-dimensional birefringence distribution measurement. *Polarization: Measurement, Analysis, and Remote Sensing II*, *3754*, 144–149. https://doi.org/10.1117/12.366325

Shribak, M., & Oldenbourg, R. (2003). Techniques for fast and sensitive measurements of two-dimensional birefringence distributions. *Applied Optics*, *42*(16), 3009–3017. https://doi.org/10.1364/AO.42.003009

Shwartz, S., Namer, E., & Schechner, Y. Y. (2006). Blind Haze Separation. *2006 IEEE Computer Society Conference on Computer Vision and Pattern Recognition - Volume 2 (CVPR'06)*, *2*, 1984–1991. https://doi.org/10.1109/CVPR.2006.71

Smyth, S. F., Liang, C., Mackay, M. E., & Fuller, G. G. (1995). The stress jump of a semirigid macromolecule after shear: Comparison of the elastic stress to the birefringence. *Journal of Rheology*, *39*(4), 659–672. https://doi.org/10.1122/1.550649

Solaguren-Beascoa Fernández, M. (2011). Data Acquisition Techniques in Photoelasticity. *Experimental Techniques*, *35*(6), 71–79. https://doi.org/10.1111/j.1747-1567.2010.00669.x

Sony Semiconductor Solutions Corporation. (2022, February 1). *Polarization image sensor with four-directional on-chip polarizer and global shutter function | Sony Semiconductor Solutions Corporation*. Sony Semiconductor Solutions Group. https://www.sony-semicon.co.jp/e/products/IS/industry/product/polarization.html

Springer. (2022, May 13). *How-to: Get permission to reuse Springer content online*. Www.Springer.Com. https://www.springer.com/gp/rights-permissions/obtaining-permissions/882

Stifter, D., Burgholzer, P., Höglinger, O., Götzinger, E., & Hitzenberger, C. K. (2003). Polarisation-sensitive optical coherence tomography for material characterisation and strain-field mapping. *Applied Physics A: Materials Science & Processing*, *76*(6), 947–951. https://doi.org/10.1007/s00339-002-2065-5

Sun, C., & Huang, H.-Y. (2016). Measurements of flow-induced birefringence in microfluidics. *Biomicrofluidics*, *10*(1), 011903. https://doi.org/10.1063/1.4939949

Sun, Y.-D., Sun, Y.-F., Sun, Y., Xu, X. Y., & Collins, M. W. (1999). Visualisation of dynamic flow birefringence of cardiovascular models. *Optics & Laser Technology*, *31*(1), 103–112. https://doi.org/10.1016/S0030-3992(99)00023-7

Sutera, S. P., & Wayland, H. (1961). Quantitative Analysis of Two-Dimensional Flow by Means of Streaming Birefringence. *Journal of Applied Physics*, *32*(4), 721–730. https://doi.org/10.1063/1.1736078

Swinson, W. F., Turner, J. L., & Ranson, W. F. (1980). Designing with scattered-light photoelasticity: Information necessary for three-dimensional surface stress analyses with scattered-light photoelasticity is presented in this paper. *Experimental Mechanics*, *20*(11), 397–402. https://doi.org/10.1007/BF02321015

Tanaka, R., Kashiwagi, Y., Okada, Y., & Inoue, T. (2019). Viscoelastic Relaxation of Cellulose Nanocrystals in Fluids: Contributions of Microscopic Internal Motions to Flexibility. *Biomacromolecules*, *21*(2), 408–417. https://doi.org/10.1021/acs.biomac.9b00943

Tanaka, R., Li, S., Kashiwagi, Y., & Inoue, T. (2018). A Self-Build Apparatus for Oscillatory Flow Birefringence Measurements in a Co-Cylindrical Geometry. *Nihon Reoroji Gakkaishi*, *46*(5), 221–226. https://doi.org/10.1678/rheology.46.221

Tao, Y.-G., den Otter, W. K., Padding, J. T., Dhont, J. K. G., & Briels, W. J. (2005). Brownian dynamics simulations of the self- and collective rotational diffusion coefficients of rigid long thin rods. *The Journal of Chemical Physics*, *122*(24), 244903. https://doi.org/10.1063/1.1940031

Taylor, G. I. (1923). VIII. Stability of a viscous liquid contained between two rotating cylinders. *Philosophical Transactions of the Royal Society of London. Series A, Containing Papers of a Mathematical or Physical Character*, *223*(605–615), 289–343. https://doi.org/10.1098/rsta.1923.0008

Te Nijenhuis, K., McKinley, G. H., Spiegelberg, S., Barnes, H. A., Aksel, N., Heymann, L., & Odell, J. A. (2007). Non-Newtonian Flows. In *Springer handbook of experimental fluid mechanics* (pp. 619–744). Springer.

Teraoka, I., & Hayakawa, R. (1989). Theory of dynamics of entangled rod-like polymers by use of a mean-field Green function formulation. II. Rotational diffusion. *The Journal of Chemical Physics*, *91*(4), 2643–2648. https://doi.org/10.1063/1.456973

Theuwissen, A. J. P. (2011). Advanced imaging: Light sensitivity. In *Solid-state imaging with charge-coupled devices* (pp. 193–218). Springer.

Tominaga, S., & Kimachi, A. (2008). Polarization imaging for material classification. *Optical Engineering*, *47*(12), 123201. https://doi.org/10.1117/1.3041770

Tomlinson, R. A., Pugh, D., & Beck, S. B. M. (2006). Experiment and modelling of birefringent flows using commercial CFD code. *International Journal of Heat and Fluid Flow*, *27*(6), 1054–1060. https://doi.org/10.1016/j.ijheatfluidflow.2006.01.007

Treibitz, T., & Schechner, Y. Y. (2009). Active Polarization Descattering. *IEEE Transactions on Pattern Analysis and Machine Intelligence*, *31*(3), 385–399. https://doi.org/10.1109/TPAMI.2008.85

Tsvetkov, V. N. (1964). Flow birefringence and the structure of macromolecules. *Soviet Physics Uspekhi*, *6*(5), 639–681. https://doi.org/10.1070/PU1964v006n05ABEH003583

Tyo, J. S., Goldstein, D. L., Chenault, D. B., & Shaw, J. A. (2006). Review of passive imaging polarimetry for remote sensing applications. *Applied Optics*, *45*(22), 5453. https://doi.org/10.1364/AO.45.005453

Tyo, J. S., LaCasse, C. F., & Ratliff, B. M. (2009). Total elimination of sampling errors in polarization imagery obtained with integrated microgrid

polarimeters. *Optics Letters*, *34*(20), 3187–3189. https://doi.org/10.1364/OL.34.003187

Vedel, M., Breugnot, S., & Lechocinski, N. (2011). *Full Stokes polarization imaging camera*. 81600X. https://doi.org/10.1117/12.892491

Walker, A. M., Johnston, C. R., & Rival, D. E. (2014). On the Characterization of a Non-Newtonian Blood Analog and Its Response to Pulsatile Flow Downstream of a Simplified Stenosis. *Annals of Biomedical Engineering*, *42*(1), 97–109. https://doi.org/10.1007/s10439-013-0893-4

Walther, J., Li, Q., Villiger, M., Farah, C. S., Koch, E., Karnowski, K., & Sampson, D. D. (2019). Depth-resolved birefringence imaging of collagen fiber organization in the human oral mucosa in vivo. *Biomedical Optics Express*, *10*(4), 1942–1956. https://doi.org/10.1364/BOE.10.001942

Wayland, H. (1960). Streaming Birefringence of Rigid Macromolecules in General Two-Dimensional Laminar Flow. *The Journal of Chemical Physics*, *33*(3), 769–773. https://doi.org/10.1063/1.1731257

Wayland, H. (1964). Streaming birefringence as a rheological research tool. *Journal of Polymer Science Part C: Polymer Symposia*, *5*(1), 11–36. https://doi.org/10.1002/polc.5070050104

Wolf, H. (1961). *Spannungsoptik*. Springer Berlin Heidelberg. https://doi.org/10.1007/978-3-662-00242-1

Wolff, L. B. (1995). Applications of polarization camera technology. *IEEE Expert*, *10*(5), 30–38. https://doi.org/10.1109/64.464928

Yang, Y., Huang, H.-Y., & Guo, C.-S. (2020). Polarization holographic microscope slide for birefringence imaging of anisotropic samples in

microfluidics. *Optics Express*, *28*(10), 14762–14773. https://doi.org/10.1364/OE.389973

Yariv, A., Yeh, P., & Yariv, A. (2007). *Photonics: Optical electronics in modern communications* (6th ed). Oxford University Press.

Yasuno, Y., Makita, S., Sutoh, Y., Itoh, M., & Yatagai, T. (2002). Birefringence imaging of human skin by polarization-sensitive spectral interferometric optical coherence tomography. *Optics Letters*, *27*(20), 1803–1805. https://doi.org/10.1364/OL.27.001803

Yevlampieva, N. P., Pavlov, G. M., & Rjumtsev, E. I. (1999). Flow birefringence of xanthan and other polysaccharide solutions. *International Journal of Biological Macromolecules*, *26*(4), 295–301. https://doi.org/10.1016/S0141-8130(99)00096-3

York, T., & Gruev, V. (2012). Characterization of a visible spectrum division-of-focal-plane polarimeter. *Applied Optics*, *51*(22), 5392–5400. https://doi.org/10.1364/AO.51.005392

Yu, C.-J. (2016). Fully variable elliptical phase retarder composed of two linear phase retarders. *Review of Scientific Instruments*, *87*(3), 035106. https://doi.org/10.1063/1.4943223

Yuhai, C., Youquan, J., & Wei, S. (1990). Utilizing phase retard integration method of flow birefringence to analyse the flow with symmetric plane. *Acta Mechanica Sinica*, *6*(4), 374–381. https://doi.org/10.1007/BF02486897

Zhang, J., Luo, H., Hui, B., & Chang, Z. (2016). Non-uniformity correction for division of focal plane polarimeters with a calibration method. *Applied Optics*, *55*(26), 7236–7240. https://doi.org/10.1364/AO.55.007236

Zhu, Y., Koyama, T., Takada, T., & Murooka, Y. (1999). Two-dimensional measurement technique for birefringence vector distributions:

Measurement principle. *Applied Optics*, *38*(11), 2225–2231. https://doi.org/10.1364/AO.38.002225

Curriculum vitae

Connor Piers Lane

20 January 1992
in Iserlohn, Germany

German and British Citizen

Education

ETH Zürich	Zurich, Switzerland
Doctorate	Nov. 2018 – Nov. 2022
Imperial College London	London, UK
Master Thesis	Oct. 2017 – Mar. 2018
ETH Zürich	Zurich, Switzerland
M.Sc. Mechanical Engineering	Feb. 2016 – Mar. 2018
ETH Zürich	Zurich, Switzerland
B.Sc. Mechanical Engineering	Sept. 2012 – Sept. 2015
Bodensee-Gymnasium Lindau	Lindau, Germany
Allgemeine Hochschulreife (Abitur)	Aug. 2002 – May 2011

Publications

Lane, C., Baumann, F., & Rösgen, T. (2022). Shear rate imaging using a polarization camera and a birefringent aqueous cellulose nanocrystal suspension. 20th international symposium on applications of laser and imaging techniques to fluid mechanics, 11-14 July 2022, Lisbon, Portugal, forthcoming.

Lane, C., Rode, D., & Rösgen, T. (2022). Birefringent Properties of Aqueous Cellulose Nanocrystal Suspensions. Cellulose, 1-15.

Lane, C., Rode, D., & Rösgen, T. (2022). Calibration of a polarization image sensor and investigation of influencing factors. Applied Optics, 61(6), C37-C45.

Lane, C., Rode, D., & Rösgen, T. (2021). Two-dimensional birefringence measurement technique using a polarization camera. Applied Optics, 60(27), 8435-8444.

Lane, C., Rode, D., & Rösgen, T. (2021). Optical characterization method for birefringent fluids using a polarization camera. Optics and Lasers in Engineering, 146, 106724.

Lane, C., Shao, Z., Zheng, K., & Lin, J. (2018). Effect of the thickness reduction of specimens on the limit strains in thermomechanical tensile tests for hot-stamping studies. *Manufacturing Review*, *5*, 11.